DOI: https://doi.org/10.2138/am-2020-6947

Quartz in Toba rhyolites show textures symptomatic of rapid crystallization

Olivia Barbee[1,2]*, Craig Chesner[3], and Chad Deering[1]

[1]Department of Geological and Mining Engineering and Sciences, Michigan Tech, Houghton, Michigan 49931, USA

[2]School of Earth Sciences and Environmental Sustainability, Northern Arizona University, Flagstaff, Arizona 86011, USA

[3]Department of Geology and Geography, Eastern Illinois University, Charleston, Illinois 61920, USA

*E-mail: oabarbee@mtu.edu

ABSTRACT

Textural and chemical heterogeneities in igneous quartz crystals preserve unique records of silicic magma evolution, yet their origins and applications are controversial. To improve our understanding of quartz textures and their formation, we examine those in crystal-laden rhyolites produced by the 74 ka Toba supereruption (>2800 km^3) and its post-caldera extrusions. Quartz crystals in these deposits can reach unusually large sizes (10–20 mm) and are rife with imperfections and disequilibrium features, including embayments, melt inclusions, titanomagnetite and apatite inclusions, spongy morphologies, hollow faces, subgrain boundaries, multiple growth centers, and Ti-enriched arborescent zoning. Using a combination of qualitative and quantitative analyses (petrography, CL, EBSD, X-ray CT, LA-ICP-MS), we determine that those textures commonly thought to signify crystal resorption, crystal deformation, synneusis, or fluctuating *P*–*T* conditions are here a consequence of rapid disequilibrium crystal growth. Most importantly, we discover that an overarching process of disequilibrium crystallization manifests among these crystal features. We propose a model whereby early skeletal to dendritic quartz growth creates a causal sequence of textures derived from lattice mistakes that then proliferate during subsequent stages of slower polyhedral growth. In a reversed sequence, the same structural instabilities and defects form when slow polyhedral growth transitions late to fast skeletal-dendritic growth. Such morphological transitions result in texture interdependencies that become recorded in the textural-chemical stratigraphy of quartz, which may be unique to each crystal. Similar findings in petrologic experimental studies allow us to trace the textural network back to strong degrees of undercooling and supersaturation in the host melt, conditions likely introduced by dynamic magmatic processes acting on short geologic timescales. Because the textural network can manifest in single crystals, the overall morphology and chemistry of erupted quartz can reflect not only its last, but its earliest growth behavior in the melt. Thus, our findings imply that thermodynamic disequilibrium crystallization can account for primary textural and chemical heterogeneities preserved in igneous quartz, and may impact the application of quartz as a petrologic tool.

Keywords: Cathodoluminescence, EBSD, skeletal morphology, embayment, growth twinning, megacryst, supereruption, Youngest Toba Tuff

INTRODUCTION

Giant subsurface bodies (100s–1000s of km^3) of silica-rich magma pose a danger to our environment and existence, driving us to understand ones that erupted in Earth's past. Key questions surround the rates at which these bodies assemble, crystallize and evolve, and for what duration they reside in an eruptible state (Bachmann and Huber 2016 and references therein). While current models indicate that their longevity in the crust depends much on their thermal evolution (e.g., Huber et al. 2009; Annen 2009; Gelman et al. 2013), the thermodynamics and kinetics of multiscale processes operating in these systems is challenging to constrain and quantify. This information, however, is crucial for understanding magma dynamics and associated timescales, and fundamentally lies stored in the erupted minerals and melt.

Compositional growth layers of magmatic minerals represent a chronologic record of the evolving subsurface environment, providing a basis for reconstructing magmatic conditions. The chemical analysis and visualization of growth layering in quartz (SiO_2) through cathodoluminescence (CL) has permitted its use as a tracer of magma temperature, pressure, and composition, as these parameters influence trace element solubility in the crystal structure. Titanium content correlates well with CL growth layers and serves as a thermobarometer (Wark and Watson 2006; Thomas et al. 2010; Huang and Audétat 2012), while Ti gradients across layer boundaries can be used to calculate diffusional relaxation times and crystal residence (Gualda et al. 2012b; Gualda and Sutton 2016). Modeled timescales derived from Ti diffusion and the faceting of melt inclusions in quartz are on the order of decades to millennia, and may suggest quartz is a timekeeper of rhyolite crystallization and residence in the crust (Gualda et al. 2012b; Gualda and Sutton 2016; Pamukcu et al. 2015; Seitz et al. 2015; 2018b). Other geochronometers such as zircon, on the other hand, suggest rhyolite bodies are much longer-lived (>100,000 years; e.g. Reid et al. 1997 and many more), bringing into question what the timescales mean (see Bachmann and Huber 2016 for a review). Because these tools or their calibrations assume that quartz reflects chemical equilibrium with its host melt, each requires careful application. Experiments and numerical modeling have already shown that fast crystal growth rates lead to increased uptake of Ti in quartz and anomalous temperature and pressure estimates (Huang and Audétat 2012; Pamukcu et al. 2016). Thus, despite quartz being a structurally simple mineral, untangling the origins of its chemical zoning at the crystal-scale has proven to be challenging and, as a consequence, interpretations remain inconsistent.

Magmatic quartz also exhibits textures that signify conditions may begin far from equilibrium. Crystal morphologies often deviate from ideal polyhedral shapes and, in some cases, may indicate near-equilibrium conditions were never achieved. Crystals are commonly filled with embayments and inclusions of melt (glass), they display concentric, oscillatory, convolute, or truncated growth zoning with varying CL intensities, and may attach in groups or clusters (e.g., Peppard et al. 2001; Bachmann et al. 2002; Liu et al. 2006; Molloy et al. 2008; Müller et al. 2009; Bachmann 2010; Beane and Wiebe 2012; Matthews et al. 2012a, b; Wilcock et al. 2013; Bégué et al. 2014; Graeter et al. 2015; Pamukcu et al. 2016; Befus and Manga 2019). This textural variability has been attributed to disparate processes, including crystal dissolution caused by magma recharge, mixing, decompression, or exsolved volatiles (embayments, convolute and truncated zoning; Bachmann et al. 2002; Matthews et al. 2012a, b; Befus and Manga 2019), faster growth or dissolution followed by regrowth (melt inclusions; Roedder 1979), the assimilation of xenocrysts (irregular, bright CL crystal cores; e.g. Liu et al. 2006), fluctuating conditions of temperature, pressure, or melt composition (compositional and oscillatory zoning; Wark et al. 2007; Thomas et al. 2010), and synneusis by crystal accumulation and compaction (crystal clusters; Vance 1969; Graeter et al. 2015). There is currently no general agreement on the mechanisms that produce these textures, which are routinely, yet variably, used as guides to conduct geochemical analyses (i.e. trace element concentrations and diffusion; isotopes; melt inclusion chemistry and volatile contents; Wallace et al. 1999; Anderson et al.

2000; Bindeman and Valley 2002; Liu et al. 2006; Campbell et al. 2009; Smith et al. 2010; Chesner and Luhr 2010; Gualda et al. 2012a; Bégué et al. 2014; Pamukcu et al. 2015; Seitz et al. 2015, 2018a, b; Gualda and Sutton 2016; Myers et al. 2016; Budd et al. 2017; Troch et al. 2017). Fortunately, petrologic experiments provide a framework within which to investigate crystal texture and morphology development (Kirkpatrick 1975; Swanson 1977; Lofgren 1980; Swanson and Fenn 1986; MacLellan and Trembath 1991). Experimental work shows that supersaturation controls the rate of crystal growth, which dictates crystal morphology and the partitioning of trace elements into the crystal relative to their diffusion rates in the melt (Hammer 2008). Therefore, crystal textures can be utilized to constrain magmatic processes and rates when combined with the chemical record.

We studied quartz from an extensively crystallized system that not only spawned Earth's largest Quaternary eruption, but captures much of the textural variability observed at silicic calderas worldwide. Rhyolites from Toba caldera provide a vast chronicle of quartz growth preserved as abundant and frequently megacrystic grains. The crystals form a wide range of sizes (0.1–20 mm) and all display imperfections and disequilibrium textures common to igneous quartz. Ubiquitous wormy embayments, abundant melt inclusions, spongy morphologies, glomerophyric appearances, subgrain boundaries, and arborescent compositional zoning are some of their prominent symptoms. Here, we use an integration of serial sectioning, imaging, and micro-analytical methods to better understand origins of these textures. After carefully examining over one-thousand quartz crystals from Toba, we come to a conclusion that contrasts some longstanding ideas on magmatic quartz growth. The following work seeks to recognize the quartz textural record in a new capacity and begins to probe for chemical links, as we find abundant evidence of rapid crystallization within this suite of textures. Our findings emphasize that integrating textural and chemical facets of the crystal stratigraphy could improve our understanding of quartz and its petrologic applications, while they have major implications for rates of dynamic magma processes and the thermal evolution of silicic magma bodies.

QUARTZ-BEARING ROCKS OF TOBA CALDERA

The Toba Caldera Complex in northern Sumatra, Indonesia has been a locus of intermediate to silicic magmatism for ~1.2 m.y. (Chesner and Rose 1991; Chesner 1988, 1998, 2012). It comprises four nested calderas and associated ignimbrites, of which the youngest three are quartz-bearing and similar mineralogically and geochemically (Chesner 1998, 2012). The most recent (~74 ka) and largest caldera-eruption produced the >2800 km^3 rhyodacitic-rhyolitic Youngest Toba Tuff (YTT) and present 100 x 30 km Toba caldera (**Fig. 1**; Chesner and Rose 1991; Chesner 1998, 2012). The YTT ignimbrite extends over 30,000 km^2 and is mostly non-welded except for where it exceeds 100 m in thickness, typically inside the caldera and within paleo-valleys (Chesner 2012). Resurgent uplift and volcanism dramatically modified the YTT caldera floor, which has centrally risen over 1 km and sits up to ~700 m above the crater's lake as the Samosir Island resurgent dome (**Fig. 1**). The only quartz-bearing post-YTT volcanics are intracaldera rhyodacitic-rhyolitic lava domes that occur in multiple locations on Samosir Island, often along faults that parallel Samosir's main eastern fault scarp. Subaerial exposures of the domes are limited (~0.2 km^3) and form several steep-sided, 30–120 m tall, vegetated hills with massive interiors and brecciated carapaces or talus. This study focuses on the YTT and these post-caldera lava domes, as they contain abundant and often large (≤20 mm) quartz crystals, and are essentially identical in compositional range (~68–77 wt% SiO_2), mineralogy (quartz, plagioclase, sanidine, biotite, amphibole; accessory titanomagnetite, ilmenite, allanite, zircon, apatite, orthopyroxene), mineral textures, Sr isotopes, zircon and allanite U-Th ages, and quartz CL zoning characteristics (Chesner 2012; Barbee 2015). Both YTT pumice and dome rock are also particularly crystal-rich (~20–40% and ~30–50%, respectively). Therefore, the YTT and lava domes likely have a common magmatic origin and together provide insight into the evolution of Toba's pre- and post-caldera magma bodies (Barbee 2015).

METHODS

Samples and preparation

Eight YTT pumice blocks and fourteen lava dome samples representative of the compositional range, textural variety, and geographic distribution of these deposits were studied (**Fig. 1**; bulk-rock compositions in **Table 1 of App.**[1]). Most YTT pumice blocks were collected within or just outside the caldera walls. Lava dome samples were collected from both dome interiors (quarries) and exteriors from three separate areas on Samosir Island (**Fig. 1**). Such chemical-spatial parameters of selected samples offer a general view of what has been suggested by Chesner (1998) to represent a compositionally-zoned magma body.

To establish a textural context for quartz (e.g., size, shape, occurrence as single crystals or clusters) and to keep those fractured intact, we prepared the majority of crystals in situ (**Fig. 2; Table 2 of App.**[1]). Hand samples were cut into 3” x 2” x 1” (76 x 51 x 25 mm) blocks and vacuum impregnated with ultra-low viscosity L.R. White Resin inside plastic molds using equipment at Eastern Illinois University (EIU) (detailed in **App.**[2]). Large 3” x 2” thin or thick sections of the blocks were made to accommodate large crystal sizes and increase the number of crystals for study (**Table 2 of App.**[1]). Unidirectional serial sectioning perpendicular to the 1” height of each block was performed to obtain multiple interior views of larger crystals (**Fig. 2; Fig. 1 of App.**[3]) and allow for a more detailed characterization of their growth records.

Petrography, stereomicroscopy, and SE imaging

Quartz textures in each sample were first studied petrographically (**Fig. 2 of App.**[3]). In addition, several hundred loose crystals hand-picked from mineral separates were imaged using a SPOT Insight QE digital camera attached to an Olympus SZ61 stereomicroscope at EIU. Secondary electron (SE) images of loose crystals were obtained using a FEI Philips XL 40 ESEM at Michigan Tech (operating conditions detailed in **App.**[2]). The loose crystals were oriented to observe their growth forms and morphologies and to complement two-dimensional (2D) views of sectioned, in situ crystals.

CL imaging

Cathodoluminescence (CL) images of 887 in situ quartz crystals (YTT, n=294; lava domes, n=593; includes single crystals and clusters; each cluster represents n=1) were collected to observe internal crystal growth patterns (**Table 2 of App.**[1]). Quartz CL zones (growth layers) are defined by variations in luminosity due to differences in trace element and defect abundances within the crystal structure (Wark and Spear 2005; Thomas et al. 2010). Brighter CL zones usually correlate with higher trace element concentrations (Ti, Al) (e.g., Wark et al. 2007; Campbell et al. 2009; Müller et al. 2009). Panchromatic CL (gray-scale) and some color CL images were obtained from up to nine 3” x 2” serial sections per sample using a TESCAN VEGA3 XMU variable-pressure SEM located at University of California, Los Angeles (operating conditions, **App.**[2]). Serial section images provide two to seven interior views of many crystals and inform the third-dimensionality of internal (growth zone) and external crystal morphologies.

EBSD analysis

Quartz cluster is used to describe a crystal with multiple growth centers, or *units*, terms that carry no genetic connotation. CL-imaged quartz clusters (YTT, n=129; lava domes, n=184; each cluster represents n=1) were first examined optically to determine which of those contain parallel units (synchronous extinction) versus non-parallel units (asynchronous extinction). Electron backscatter diffraction (EBSD) analysis was primarily focused on adjacent non-parallel units in thirteen different clusters to determine their relative three-dimensional (3D) crystallographic orientations. Quartz clusters were chosen from samples wherein they are most abundant and based on a set of textural criteria: (i) clusters containing only two units; (ii) clusters having more than two units, (iii) clusters having more than two units and at least one pair of parallel units; (iv) the presence of internal arborescent CL zones in (i) and (ii); (v) an absence of arborescent CL zones in (i) and (ii); and (vi) clusters of different sizes. In addition, a set of nine clusters comprising parallel units with apparent 1–2° extinction offsets were targeted to quantify degrees of crystallographic misorientation. EBSD maps were collected using Oxford Instruments HKL Nordlys II Detector and Channel 5 software on a JEOL JSM-7600F SEM at Nanyang Technological University, Singapore and TESCAN VEGA3 LMU SEM at Bowdoin College (operating conditions, **App.**[2]).

Because all quartz now reside below the β-α inversion (<573°C, 1 atm), their atomic lattices have trigonal symmetry. This means crystals initially formed as β-quartz now have rhombohedral (trigonal) lattice planes despite preservation of an external hexagonal dipyramidal

DOI: https://doi.org/10.2138/am-2020-6947

form. EBSD patterns (EBSPs) acquired from Toba quartz were compared to those of known α-quartz lattice parameters within the Channel 5 HKL phase list to calculate crystallographic orientations. Quartz crystallographic data project three poles each to the upper $\{10\bar{1}1\}$ and lower $\{01\bar{1}1\}$ faces (*r* and *z* rhombohedral lattice planes) that are rotated 60° about one another on an upper hemisphere stereographic projection. Angles between corresponding crystallographic axes and corresponding poles to faces of grouped crystal units were measured manually in HKL Channel 5 module Mambo and Stereonet 8 (Allmendinger et al. 2012; Cardozo and Allmendinger 2013); where there is some spread to orientation data, mean orientations were used (Beane and Wiebe 2012). Measurements between *c*-axes were replicated and indicate ~1–4° measurement errors (Brugger and Hammer 2015). Given the average mean angular deviation (MAD) values of 0.2–0.9, the number of Kikuchi bands detected in EBSPs (7–9), and work of Krieger-Lassen (1995), the relative precision of crystallographic measurements is ~1° (Beane and Wiebe 2012) (data acquisition and reduction detailed further in **App.**[2]).

X-ray tomography

The shattered nature of Toba crystals >1 mm does not allow them to be extracted intact. X-ray tomographic imaging of raw YTT pumice (T-20 and T-57) and dome lava (TT-2) was performed using a NSI ImagiX microCT system at Vanderbilt University to allow direct 3D observation of in situ quartz crystals and to compliment 2D cross-sectional views (e.g., Gualda and Rivers 2006; Pamukcu et al. 2010, 2012) (operating conditions, **App.**[2]). Three-dimensional X-ray tomograms of 25–50 mm diameter cylindrical samples were reconstructed from raw data using ImagiX software. The visualization of air, glass, and different mineral phases within 3D reconstructions is possible due to their differing linear attenuation coefficients, which are functions of density and mean atomic number (Gualda and Rivers 2006; Pamukcu et al. 2012). Thus, in 3D gray-scale maps, air and glass appear dark, whereas biotite, amphibole, and magnetite appear bright, and quartz and feldspars have an intermediate and relatively similar brightness. Using gray-scale thresholding, quartz crystals were observed by removing air and glass from tomograms, and distinguished from feldspars by crystal habit and morphology.

Crystallographic modeling

Quartz habit (i.e. size, growth forms), interfacial angles, and twin laws were simulated using SHAPE v7.4 software (Dowty 1980a, 1987) and *c*/*a* crystallographic axial lengths of both β- and α-quartz polymorphs (Frondel 1962; Deer et al. 1963). Angular relationships between corresponding crystallographic axes of grouped crystal units measured in Mambo (Channel 5) and Stereonet 8 were compared with those of each twin law to identify quartz twinning (Frondel 1962). Crystal unit shapes and CL zoning were then combined with EBSD data to model 3D solutions of quartz clusters using SHAPE. To determine the crystallographic positions of grouped units relative to one another, simple growth zones were applied to SHAPE crystal models and matched closely to CL zone configurations by changing section height (x=0 at crystal center), unit distances, and translation vectors.

LA-ICP-MS

Quartz trace element concentrations were collected from seven in situ crystals displaying arborescent CL zones using a 193 nm Resonetics Resolution 155 excimer laser ablation system coupled to a Thermo Scientific Element XR sector field mass spectrometer at ETH Zürich. Quartz was ablated using a spot size of 29 μm (operating conditions, **App.[2]**). NIST 612 and

This is a preprint, the final version is subject to change, of the American Mineralogist (MSA)
Cite as Authors (Year) Title. American Mineralogist, in press.
DOI: https://doi.org/10.2138/am-2020-6947

NIST 610 were used as primary standards and QTZ-F1 (crystal aliquot from Audétat et al. 2015) was used as a secondary standard. Data reduction was performed using SILLS software (Guillong et al. 2008) with SiO_2 contents at 100% for internal standardization. Elements measured include: Li^{7}, B^{11}, Na^{23}, Mg^{25}, Al^{27}, Si^{29}, P^{31}, K^{39}, Ca^{43}, Ti^{47}, Ti^{49}, Mn^{55}, Fe^{57}, Cu^{63}, Zn^{66}, Ga^{69}, Ge^{72}, Rb^{85}, Nb^{93}, Ag^{107}, Sn^{118}, Ba^{137}, Pb^{208}. Reported Ti concentrations are ^{49}Ti, as interferences are negligible for this isotope.

TEXTURES OF TOBA QUARTZ

Habits

Quartz occurs as both solitary and composite crystals, or clusters, made of several crystal units (**Fig. 2**; **Figs. 1** and **2 of App.[3]**; also see **Figs. 4–8**). Individual clusters contain, on average, two to four units, but may comprise as many as fourteen units, each discernible by repetitive crystal faces and cores (cf. Beane and Wiebe 2012; Welsch et al. 2013). Cluster sizes are generally independent of the number of constituent units. Both single crystals and clusters form microcrysts (<0.1 mm), mesocrysts (0.1–0.5 mm), and macrocrysts (0.5–10 mm), whereas only clusters form megacrysts (>10 mm). Megacrysts reach respective diameters of 20 mm and 15 mm in the YTT and lava domes (**Fig. 2**), and occur throughout both deposits, except in fine-grained high-SiO_2 YTT pumice (sample T-5B; **Table 1 of App.[1]**; **Figs. 1** and **2 of App.[3]**). Mesocrysts and microcrysts, on the other hand, are only significant in the more-evolved rocks (**Fig. 2 of App.[3]**), though microcrysts occur exclusively in the lava domes.

Toba quartz is expected to be crystallographically preserved as high-temperature (>573°C, 1 atm), hexagonal β-quartz. However, in all samples, we find an overwhelming abundance of crystals to have crystallographic forms more characteristic of the low-temperature

(<573°C, 1 atm), trigonal α-quartz polymorph (**Figs. 3–6**). Equant crystals exhibiting hexagonal symmetry appear as hexagonal dipyramids $p\{10\bar{1}1\}$, whereas those exhibiting trigonal symmetry have *apparent* positive $r\{10\bar{1}1\}$ and negative $z\{01\bar{1}1\}$ rhombohedra ± a prism $m\{10\bar{1}0\}$ (**Figs. 3–6**; Frondel 1962). Trigonal-appearing quartz exhibit distinctive features that include (i) diagonal edges bounding either opposing rhombohedral faces, or opposing rhombohedral and prism faces (**Figs. 3** and **4**), as well as (ii) edge extension along apical portions of touching *r* faces as *z* faces become smaller, both products of faster growth of typically *z* faces relative to *r* faces, which yields larger *r* rhombohedra (Sunagawa 2005); and (iii) frequent asymmetry which can result from differential growth rates of individual rhombohedra belonging to the same or crystallographically equivalent form (Frondel 1962; **Figs. 3**, **4a–h, j–m** and **5a**). The prism form, when present, can be either stubby (e.g., **Fig. 4b, m**) or elongate parallel to the *c*-axis (shape ratio *a*:*c* = ~1:1.5–1.7; **Fig. 4c, d, l**). In thin section, asymmetric rhombohedral and prism faces can be identified through interfacial angle measurements when the *c*-axis orientation approximately parallels the plane of section (**Figs. 3, 4e, 5b,** and **6b, c, e, f**).

Morphologies

Toba quartz crystals show two primary morphologies: polyhedral (**Figs. 3, 4a–c, e, i, l, m** and **6a, h–j**) and skeletal (**Figs. 3, 4d, f–h, j, k** and **6b, d, k**). Both morphologies appear in single samples, and are commonly observable within a single crystal or crystal unit, such that some faces are well-developed and flat, and others are hollow (**Figs. 3, 4d, g, j, k 5a,** and **6c, e–g**). Skeletal (hopper) cavities can correspond to some or all pyramidal $\{10\bar{1}1\}$ – or rhombohedral $\{10\bar{1}1\}$, $\{01\bar{1}1\}$ – and prism $\{10\bar{1}0\}$ faces. Each cavity contains tens to as few as one or two sharp, concentric, stair-like terraces (i.e. macrosteps; Faure et al. 2003a, 2007) stepping down into a funnel-shaped, hollow crystal face (compare **Figs. 4d, f–h, j, k, 5a,** and **6b–d**). The terraces, whose widths range from tens to hundreds of micrometers, parallel external crystal face directions and appear petrographically as curvilinear lobes or faceted to slightly rounded ledges separated by matrix glass (e.g., **Fig. 6b, d**). All single crystals and grouped crystal units still maintain recognizable, doubly-terminated hexagonal or pseudo-hexagonal shapes.

Subordinate morphologies include anhedral and granophyric intergrowths with feldspars (1–2 mm), the latter occurring only in the most-evolved rocks (see **Fig. 5j, k of App.**[3]). Anhedral is used to describe extensive rounding along what were either developing or deteriorating skeletal cavities (i.e. cavity walls have smooth surfaces with curvature and minimal to no terracing; **Fig. 4j, k**; cf. MacLellan and Trembath 1991). A reduction in faceting, however, need not be uniform over a single crystal or crystal unit (e.g., **Fig. 4j**). Thus, compound morphologies result between polyhedral, skeletal, and anhedral, and are also characteristic of the granophyric quartz. Quartz intergrowth morphologies transition outward from anhedral to skeletal to radiating with potassium feldspar, and have polyhedral terminations in contact with matrix glass; plagioclase crystals are subhedral in the intergrowths (see **Fig. 5j, k of App.**[3]).

Embayments

Quartz embayments are lobate voids that extend up to several millimeters between their outlets at crystal margins and the crystal interior (e.g., **Figs. 4e, h, j, k** and **6a–g**). They appear in cross section as smooth-walled channels and ovoid to subpolygonal holes filled with vesicular matrix glass (**Fig. 6a–g**). Their contours can become exceptionally wormy and concentrated to generate a spongy texture in the host crystal (e.g., **Fig. 6b**). Embayments occur dominantly within crystal face sectors, as opposed to edge or apical locations, and can occur locally between grouped crystal units. Serial sections and tomograms show that the crystal rim near the dipyramidal mirror plane (0001), or of the $\{10\bar{1}0\}$ prism form, frequently contains higher concentrations of embayments than regions nearer the pyramidal – or rhombohedral – terminations. Importantly, observable intersections of embayment walls and crystal rims are nearly always bounded by crystal facets, albeit a common light curvature of crystal corners and edges (**Figs. 4–6**).

Inclusions

Single crystals and grouped units of quartz contain abundant melt inclusions (MIs), which typically measure ~10–200 μm and have negative-crystal, dipyramidal shapes (e.g., **Fig. 6l**; Chesner and Luhr 2010). Only within the most-evolved YTT pumice (sample T-5B) are MIs of this size commonly ovoid, or non-faceted (Chesner and Luhr 2010). Sealed embayments may also constitute MIs that are larger (~200–500 μm) and irregular (e.g., **Figs. 4i** and possibly **6a–c, e–g**). Melt inclusions are frequently located beneath euhedral faces and the flat bottoms of hollow faces (cavities) (e.g., **Figs. 3, 4i,** and **6b, c**; cf. Welsch et al. 2013); irregular ones occasionally parallel and mimic the shape of the overhanging pyramidal or rhombohedral face (**Fig. 4i**). Negative inclusions can also occur in planar arrays parallel to face directions and crystal unit contacts. Additionally, augen-shaped to highly oblate melt lenses (≤500 μm) lie between grouped crystal units (**Fig. 7**; also see **Fig. 10**). Many MIs contain post-entrapment modifications such as shrinkage bubbles, devitrification, and daughter crystals (detailed in Chesner and Luhr 2010). Most of those >200 μm have oversized vapor bubbles related to cracking and leakage. Crystal fractures radiating from the walls of these larger inclusions imply that the shattered nature of quartz resulted from MI decrepitation upon rapid syneruptive decompression (e.g., **Fig. 6a, f; Fig. 2 of App.**[3]; Best and Christiansen 1997). Notably, sparse titanomagnetite [$Fe^{2+}(Fe^{3+},Ti)_2O_4$] microcrysts and mesocrysts can lie within the open fractures, or are attached to walls of intact MIs and embayments (**Fig. 5b**; Chesner 1998; cf. Befus and Manga 2019). In the latter case, magnetite is located at or near the heads of embayments. **Figures 5b, 6l, m** and **Movie 1 of Appendix**[3] best demonstrate examples of these relationships. Some magnetite crystals are peculiar in that they represent single or interpenetrated (parallel or twinned) crystals with stepped topography on octahedral faces (**Fig. 6m and Fig. 6 of App.**[3]; cf. Fig. 6 of Drev et al. 2013). Quartz also contains highly luminescent micro-needles of what is likely to be apatite [$Ca_5(PO_4)_3(F,Cl,OH)$] (**Fig. 6m**; also see **Figs. 10a and 11a**]. These needles can be at least partially enclosed by a tiny melt capsule, and often host their own tubes of melt (glass) (**Fig. 6m**). Long axes of the needles parallel internal growth zones and external face directions of host quartz crystals. Quartz rarely occurs as an inclusion or constituent phase in clusters composed of other minerals; whereas accessory magnetite and apatite also occur in the matrix and as inclusions in other major and accessory phases.

Clusters of parallel crystal units

Quartz clusters represent approximately 45–60% of quartz crystals in YTT samples and 5–60% of crystals in lava dome samples (**Figs. 7** and **8**). Two-thirds of the clusters are made only of organized, parallel units (e.g., **Figs. 5a, 6b, e, k** and **8a**; **Table 3 of App.**[1]). Identical *c*-axis and *a*-axes orientations of units are indicated by their simultaneous optical extinction, same interference color, and parallel corresponding faces (e.g., **Figs. 6b, e, f, k**). Parallel units within several clusters, however, display slight 1–2° extinction offsets (e.g., **Fig. 6g**), which correspond to EBSD-measured misorientation angles of 0–5° between the *c*-axes [0001] and 0–7° between corresponding *a*-axes (mostly within error) (**Table 3 of App.**[1]; **Fig. 8a, b, d, e**). Misorientations appear as grain or subgrain boundaries (**Fig. 6f, g**), but may also be delineated by narrow melt lenses (**Fig. 7**; also see **Fig. 10**). Additionally, rare compact clusters of tens of parallel units show successive extinctions every ~2–3° of rotation, planar to irregular dislocation planes, and highly repetitive sets of parallel faces (**Fig. 6k**), similar to that described for dendritic olivine macrocrysts in basalts (e.g., Welsch et al. 2013, their Fig. 10e, f). Parallel orientations are also inferred for ruptured, or detached, units with their corresponding *c*-axes and *a*-axes separated by a misorientation angle of 0–12° and 0–13°, respectively (**Table 3 of App.**[1]).

All parallel units within a cluster usually appear to have similar habits, morphologies, and sizes; otherwise, units exhibit a decrease in size away from the center of a cluster (e.g., **Figs. 5a** and **6f**; cf. Welsch et al. 2013). Parallel units can even appear as interpenetrated replicas having the same habit and shape ratio (e.g., **Figs. 6b, e, f, 7** and **8a, d**; also see **Fig. 10a, g** and **Fig. 5f of App.**[3]; cf. Welsch et al. 2013). **Figure 5a** shows multi-angle tomographic views of an in situ macrocryst made of two (ruptured) units of different sizes, but with parallel corresponding faces and the same shape ratio. Some faces are clearly hollow, whereas others may exhibit depressions or terraces. Notably, crystal faces do not occur where the smaller unit sits astride the larger unit, indicating the units are intergrowths. In section planes near cluster margins, units may be portrayed as closely-spaced individuals separated by matrix glass, whereas sections through the centers of clusters expose unit contacts or interpenetration (e.g., **Fig. 3a of App.**[3]; also see **Fig. 10h**). Section plane orientations also dictate whether the external morphology of a cluster resembles a single hexagonal crystal, aggregate, or rare chain (e.g., compare **Fig. 8a, e**). Parallel units may be separated by a fracture or melt lens at their suture (**Fig. 7, 8d**); otherwise, they form continuous interstitial growth zoning, appearing as a single entity rather than an aggregate of aligned individuals (compare **Fig. 8a, e**; also see **Fig. 10**).

Twinnings

Contact twins. The remaining one-third of quartz clusters include at least one pair of units in a non-parallel orientation. Adjacent non-parallel units consistently show larger ~5–30° offsets in extinction position (complements of 60–85°), varied interference colors, and misaligned growth faces (**Figs. 6f, h–j**; **Fig. 3 of App.**[3]). Unit pair orientations determined using EBSD frequently agree with two common quartz twin laws: Verespatak and Esterel (**Fig. 8b–e**; **Table 3 of App.**[1]). Each twin law describes a contact twin, expressed by mirror reflection in the $(11\bar{2}2)$ compositional plane in Verespatak twins and the $(10\bar{1}1)$ plane in Esterel twins, or by 180° rotation about low-index twin axes (**Fig. 3**; Grimmer 2006). Resultant inclination of the *c*-axes at angles of 84°33' (Verespatak) and 76°26' (Esterel), and the orientations of *a*-axes and faces distinguish the twin types (**Fig. 3**; Drugman 1927; Kozu 1952; Beane and Wiebe 2012). Like parallel units, intact twinned units may deviate from ideal *c*-axis orientations by up to 5° (mostly within error). Therefore, intact units with their *c*-axes separated by an angle of 85–89° and one of their $\{10\bar{1}0\}$ poles parallel (0–9°) (i.e. consider it an *a*-axis $[10\bar{1}0]$ or $m(10\bar{1}0)$ prism face) are interpreted as Verespatak twins (**Fig. 8b, e**). Whereas, intact units with their *c*-axes oriented 71–77° apart, the poles to one set of dipyramidal – or rhombohedral – faces oriented approximately parallel (3–13°), and the other set oriented ~30° apart (25–36°) are interpreted as Esterel twins (**Fig. 8c, d**; **Tables 3 and 4 of App.**[1]; cf. Beane and Wiebe 2012; Graeter et al. 2015). Most ruptured units in proximate twin orientations did not rotate far from original twin position (e.g., **Fig. 8c**).

Conversely, many non-parallel units do not satisfy Verespatak or Esterel twin laws (**Table 3 of App.**[1]), and have been previously denoted as "random" orientations in some granitoids (Beane and Wiebe 2012; Graeter et al. 2015). However, units twinned repetitively on the same law or combinations of laws can create additional *c*-axis coordinations (**Table 4 of App.**[1]). Thus, angles between *c*-axes in **Table 3 of Appendix**[1] close to 67° (supplement of 113°), 60°, 51°, 48°, 38°, 33°, 27°, and 9° may comply with multiply-twinned units in clusters manifesting the Verespatak or Esterel laws (Drugman 1927; Watanabe 1974; this study; **Table 4 of App.**[1]). For example, *Units 1* and *2* of the YTT macrocryst in **Figure 8c** are non-twinned ($+c_1 \measuredangle +c_2 = 113°$), yet still related by symmetry because they are linked by and both Esterel-twinned with *Unit 3*. The much smaller lava dome macrocryst in **Figure 8d** shows the same repeated Esterel twinning and crystallographic relation between non-twinned units. Alternatively, some extraneous *c*-axis coordinations may comply with rare twin laws listed in **Table 4 of Appendix**[1]; although it seems implausible such a variety of rare twins would occur frequently in the subset of clusters analyzed (see Drugman 1927; Frondel 1962). These 'other' orientations are important nonetheless, as their recurrences may imply that potentially all units within a given cluster are in some way related by symmetry. Indeed, the number of possible *c*-axis coordinations becomes exponential with unit additions and twin law combinations.

Simple twinning, multi-component twinning, and 'other' possible assemblages manifest in clusters ranging widely in size, from microcrysts to megacrysts. Contact twins can occur as a group of two virtually equal units (e.g., **Fig. 6j**), or, more commonly, as symmetric or asymmetric attachments on groups of parallel units (e.g., **Fig. 8b, d, e**). 'Other' orientations often recur in clusters having many units (**Table 3 of App.**[1]). Units touching twins can replicate twin orientations and sometimes appear in positions of re-entrant edges (**Fig. 8b, d, e**; **Fig. 3e of**

App.[3]; cf. Drugman 1927; Welsch et al. 2013). Like parallel units, voids or melt lenses can occur along twin contacts (cf. Kozu 1952; Welsch et al. 2013). In some section planes, Verespatak twins exhibit characteristic V-shapes and flattening parallel to their co-planar $m\{10\bar{1}0\}$ prism faces (**Figs. 3** and **6h, j**; Sunagawa et al. 2004). Comparing 2D sections of clusters between tomograms and EBSD maps verifies that twin orientations also generate more prismatic cross-sections similar to those seen in **Figures 6f, i, j** and **8b, d** [also see **Figs. 10e, g, 11c**; cf. Fig. 9 of Müller et al. (2000) and Figs. 5a, 6a of Beane and Wiebe (2012)].

Penetration twins. Stereographic projections of EBSD data show six poles (instead of three) rotated ~60° about one another for each set of rhombohedral planes [i.e. $\{10\bar{1}1\}$ and $\{01\bar{1}1\}$] (**Fig. 8**). This particular projection reflects a penetration twin corresponding to the Dauphiné Law (**Fig. 3**). Dauphiné twins are related by a 180° rotation about the *c*-axis on $\{10\bar{1}0\}$ and are of like handedness, thus they have coincident *c*-axes and coincident $r\{10\bar{1}1\}$ and $z\{01\bar{1}1\}$ lattice planes (Frondel 1945, 1962). Consequently, the twin and host are optically undetectable. Dauphiné twins are only stable in the α-quartz structure due to symmetry, and therefore have no primary origin associated with temperatures above 573°C (1 atm). As seen in Frondel's (1945) basal sections of etched natural α-quartz, Dauphiné twin domains are irregular and often patchy (**Fig. 3**). Similar intergrowth irregularities are depicted in EBSD maps, which define patchy regions of two distinct crystallographic orientations within single crystals or crystal units (**Fig. 8**). Twin domains can be preferentially located along closed and open fractures associated with decrepitated MIs, consistent with observations made by Frondel (1945). Dauphiné twins can also follow boundaries between non-parallel units, but extend continuously across units of identical orientation (**Fig. 8**), the latter implying that parallel units represent a single crystal lattice.

Zoning

Adaptations. Cathodoluminescence images reveal that quartz growth layers adapt to crystal imperfections. That is, skeletal cavities, embayments, MIs, and crystal unit contacts do not dissect, but rather deflect growth zones. Linear zones of varied thicknesses taper inward along walls of embayments and curve around MIs (**Fig. 7** and **Fig. 4 of App.**[3]; also see **Figs. 8, 10, 11**). In contrast, oscillating lens-shaped zones (≤10–100 μm), which generally swell along face directions and pinch at edge locations, pinch out prior to approaching margins of cavities, embayments, and MIs (**Fig. 7**; exceptional examples in **Fig. 4a, b, j, p of App.**[3]). Lens zone adaptations also signify locations at which crystal segments have sutured together and sealed embayments (at least partially, e.g., **Fig. 4p of App.**[3]). In addition, as zones approach the contacts of incompletely sutured crystal units (i.e. melt lenses), they either pinch out (**Fig. 7**; also see **Fig. 10g, i**), become indistinct and disappear, or taper inward at the seams (e.g., **Fig. 8d**). Zone adaptation can be broad in character, with deflection beginning hundreds of micrometers away from a crystal imperfection (e.g., **Fig. 4l, m, s of App.**[3]), or it can begin within just tens of micrometers of one's periphery (e.g., **Fig. 4a, b of App.**[3]). Zone boundaries and adaptations are unseen only proximal to embayments elongated perpendicular to the section plane, presumably because zones taper out of the section in this case. The few cross-cutting relationships observed differ in that they correspond to a crystal-wide dissolution surface (rounded zone boundary; e.g., **Fig. 10d; Fig. 4m, s of App.**[3]).

Branching patterns. Cathodoluminescent zones bearing a tree-like resemblance appear in ~25–70% of quartz crystals in YTT samples and ~20–60% of crystals in lava dome samples (**Figs. 9–11**; **Fig. 5 of App.**[3]). These arborescent zones are dominantly located at the cores of single crystals and crystal units, but can additionally or alternatively reside in their mantles. Arborescent zones are slight to moderately *brighter* CL features corresponding with modest enrichments in Ti (by ~5–10 ppm; as high as ~20 ppm) and sometimes Al (by ~5–20 ppm) concentrations (**Figs. 10** and **11**; trace element data in **Table 5 of App.**[1]). Although their branching patterns vary in scale and intricacy among crystals, arborescent zones emanate consistently from the crystal interior, bifurcating from internal vertices of a concentric euhedral zone of identical or even brighter CL (**Figs. 9–11**). Each arborescent 'tip' may extend as a ~0.05−1 mm primary limb anchoring a second set of branches, reminiscent of the feathery P-rich zonings described extensively in olivine (Milman-Barris et al. 2008; Welsch et al. 2013, 2014). Tertiary branches are rare (**Figs. 9f** and **10b**). The primary limbs usually appear straight, but occasionally curve or arch as they follow paths of older apical and edge positions within a crystal (**Figs. 9f** and **10b**). The secondary branches are more varied, ranging from feathery regions to discrete, regularly-spaced, ≤100 μm long and 10–40 μm wide lineations, and have terminations that are blunt, or tapering, curved, and diffuse. Each primary limb displays its secondary branches in two arrays, each in a single orientation that may or may not align with the outer growth faces of the crystal. Branches paralleling subjacent external face directions form interior angles with the primary limb, creating a chevron semblance (e.g., **Figs. 9a–c, e, g–k**); whereas, those forming roughly perpendicular or exterior angles with the primary limb do not parallel subjacent face directions (but opposite, or adjacent, ones), and more closely simulate the pinnate venation of a leaf (e.g., **Figs. 9d, f, 10b,** and **11b**). In both cases, the loci of branch terminations often trace crystal faces of $\{10\bar{1}1\}$ or $\{10\bar{1}0\}$ (e.g., **Fig. 9a**). The diverseness of 2D branching patterns appears to be largely an effect of crystallographic and section plane orientations based collectively on (1) EBSD information, (2) pattern disparities between individual limbs within the same crystal (e.g., **Figs. 9k** and **10a**), and instances where secondary branches derive from no apparent primary limb (i.e. chevron oscillations lying on a common axis; e.g., **Figs. 9c, 10f**). Notably, sections through the crystal core at nearly perpendicular or parallel orientations to the *c*-axis often display the most spectacular patterns – ‘snowflakes’ with several ‘arms’ that presumably relate to positions of *c* and *a* crystallographic axes or growth faces (e.g., **Figs. 9f, k** and **10a, b**; cf. Swanson and Fenn 1986).

Arborescent zones are accompanied by a number of features. The most fundamental one is a distinct, *very dark* CL region occupying the interstices of the branching pattern (**Figs. 7, 10** and **11**). Chemically, this region is poorer in Ti relative to the arborescent zones (**Fig. 11**; **Table 5 of App.**[1]). It can merely coat limbs and branches (**Figs. 10b, j** and **11a, b**), but typically broadens within face sectors, and terminates in facets 10–20 μm beyond limb extremities (e.g., **Fig. 10a**). Where it occurs interstitially, the dark region is non-zoned; whereas, interior to the euhedral zone rooting limbs and branches, it commonly separates brighter, concentric oscillations (**Figs. 9–11**). The euhedral ‘root’ zone is often the outermost of these oscillations, which are periodic, yet may be widely-spaced (20–50 μm wide, 20–40 μm apart) or fine-scale (5–10 μm wide, 5–10 μm apart). Notably, the CL of the oscillations is similar to that of the ‘root’ and arborescent zones. Additional oscillations sometimes lie outside a branching pattern (e.g., **Fig. 10d, h**; **Fig. 5g of App.**[3]); some crystals even show complex alternations of oscillations and arborescent zones (**Figs. 8e, 9g, i** and **10e, h**; **Fig. 5a, d of App.**[3]). Otherwise, the oscillations may appear unaccompanied (**Figs. 8a, b, d** and **10k**). Together, brighter arborescent zones, oscillations, and their dark envelope extend across a ~0.5–2 mm^2 area at crystal or unit cores, where they most commonly occur. In crystal or unit mantles, arborescent zones occasionally manifest as a single, thin, concentric, ‘wavy’ zone composed of numerous, faceted, rimward projections (≤50 μm), which attach along internal faces or rounded surfaces (**Figs. 7** and **10j**; cf. Fig. 3.18 of Sunagawa 2005); it is here that precedent and succedent oscillations are absent, and the dark region is limited to a veneer (**Figs. 10e, f, j** and **11b**). Alternatively, arborescent zones can be associated with a subordinate zonation that exhibits the *brightest* CL observed for Toba quartz. The branching patterns themselves are configured in the same ways as described previously, but are relatively much brighter and gently merge with a region chiefly of high CL intensity (**Fig. 10l; Fig. 5l of App.**[3]). In most cases, the bright region is thick (1–3 mm), often spongy, and can mantle a rounded dissolution surface. Because the bright region is filled with MIs and embayments, it exhibits tortuous internal zoning that is adaptive to these features (e.g., **Fig. 10l** and **Figs. 4n, s, 5l of App.**[3]).

Pockets of melt (glass) are positioned next to every pattern of arborescent zones. Melt inclusions tend to situate between limbs, branches, and tiny projections of 'wavy' zones (**Figs. 7, 8, 9–11**), while embayments can extend between primary limbs, sometimes causing crystals or units to externally mimic a morphology defined roughly by the shape of the internal branching pattern (**Figs. 10c** and **11b**). Although MIs and embayments only occur in regions surrounding arborescent zones, they may abut limbs and branches. Halos that often surround melt pockets also may abut the arborescent zones (**Fig. 10** and **11**). These CL halos can be subtly zoned, sometimes showing a circular zone inside a triangular one. In a given crystal, most halos typically match in CL intensity, but cannot be easily matched with that of nearby zones. Melt inclusions associated with halos are not always exposed, while the visibility of halos diminishes as the MIs become smaller. Rarely do halos correspond with a crystal-wide truncating zone (i.e. dissolution surface; **Fig. 10d**). Melt inclusions with walls that truncate zones tend to be central to the core and branching pattern where an occasional magnetite inclusion will take the same position, suggesting these are possible points of quartz nucleation instead of resorption sites (e.g., **Figs. 8a, b, d** and **10c, d, h**; cf. Müller et al. 2009).

Identities of crystal units. Arborescent zones show an affinity with quartz clusters, appearing in ~40–85% of YTT clusters and up to ~80% of lava dome clusters. In most samples, approximately half or more of the observable branching patterns occur in grouped crystal units, as opposed to single crystals with one growth center (**Figs. 8, 10** and **11**). Regardless of how complex or simple the cluster assemblage, any unit pair may exhibit arborescent zones, but parallel units display them most frequently. Even if a unit pair does not display arborescent zones, it may still coexist with or be bound to units that do. Considering that single sections do not expose equivalent levels of all units in a cluster (**Figs. 8a, e, 10h** and **11c; Fig. 3a, b of App.**[3]), the reported numbers of units, clusters, and total crystals containing arborescent zones are minimums (e.g., Dowty 1980b).

Serial sections reveal that grouped units of the same size share similar to virtually identical core-to-rim zoning (e.g., **Fig. 8a**). Whereas, grouped units that differ appreciably in size, namely large megacryst units versus relatively smaller units (~1–2 mm) occasionally embedded in their mantles, do not share the same core-to-rim zoning (e.g., **Fig. 8e**; **Fig. 3a, b of App.**[3]). In these megacrystic clusters, for example, only the larger units have closely-spaced, nearly identical cores, which are mantled by a common exterior (**Fig. 8e**; **Fig. 3a, b of App.**[3]). Generally, similarly-zoned units exhibit the same sequence of CL variations, but often in different zone thicknesses that are presumably controlled by 2D sectioning; similar units are observable in ~50–100% and ~55–100% of YTT and lava dome clusters, respectively. Two or more nearly identical units are visible in ~15–90% and ~0–60% of the respective clusters. Furthermore, all units in a cluster can appear similar regardless of orientation, but it is common to see only some units that are identical (e.g., three of seven units). Conceivably, units sharing a common orientation are most likely to appear identical in 2D sections (e.g., **Fig. 8a, d**). For example, the most near-identical units observed in a single section of a cluster is five, and they lie in parallel orientation with arborescent zones at their cores (**Fig. 8a**; also see **Fig. 12**). Rarer sections of parallel units expose unit interpenetrations through to the core zones, wherein arborescent limbs connect from one unit to another (**Figs. 10c, g**; **Fig. 5h of App.**[3]).

DISCUSSION

Textural and chemical signs of rapid quartz growth

Deciphering the quartz record at Toba requires understanding the mechanisms that form crystal textures. Here, we relate our observations to theoretical and experimental work on crystal growth to interpret quartz texture origins (summarized in **Table 1**). The outcome is a model demonstrating a genetic interrelation of disparate textures that can be explained by an overarching process of rapid crystal growth.

Buried skeletal and dendritic relics. *Signs: Zoning forms a branching pattern brighter in CL and richer in Ti; Melt inclusions and embayments are positioned between arborescent zones.*

Arborescent CL zones (**Figs. 9–11**) resemble contours of skeletal and dendritic quartz grown in crystallization experiments (e.g., Swanson and Fenn 1986). Their architecture also shows a crystallographic control strikingly similar to P-rich zones that delineate skeletal-dendritic frameworks of olivine (Welsch et al. 2013, 2014; Milman-Barris et al. 2008). The growth processes by which those crystal morphologies develop are diffusion-controlled, where the crystal growth rate exceeds the diffusion rate of impurity elements away from the crystal interface under high degrees of undercooling (i.e. the difference between the liquidus and magma temperature, or ΔT) and supersaturation (Kirkpatrick 1975; Sunagawa 1981). Thus, crystal corners and edges (regions of greater surface area) rapidly grow into sharp protuberances by penetrating through a compositional boundary layer contaminated with rejected incompatible elements and into melt richer in those compatible with the crystal (Hammer 2008), a process known as constitutional supercooling (Berg 1938; Kirkpatrick 1975; see **Fig. 14**). This preferential growth leads to the branching morphology of dendrites, as well as the macroscopic terraces lining hopper cavities, each a new frame that envelops the growing crystal (Faure et al. 2007; Welsch et al. 2013). Considering that natural and experimentally-produced hopper crystals and dendrites develop melt-filled cavities between their protrusions (e.g., Drever and Johnston 1957; Lofgren 1974; MacLellan and Trembath 1991; Faure et al. 2003a, 2007; Kohut and Nielsen 2004; Brugger and Hammer 2015; Welsch et al. 2013, 2014, 2016), the strict positioning of MIs or embayments between limbs and branches substantiates our idea that arborescent zones represent buried, three-dimensional structures (**Figs. 10–13**; see *Trapped melt*).

Using their shapes in cross-section with crystal orientation data, we formulate a 3D model of arborescent zones that defines them as older hopper cavities and dendrites, whose diverse profiles can be resolved by varying crystallographic or section plane orientation (**Figs. 12** and **13**). Sections through relic hopper crystals intersect their once hollow faces and the terraces that lined or overhung these cavities. Most sections near the center of a hopper relic portray its planar terraces as secondary branches paralleling external forms $\{10\bar{1}1\}$, $\{01\bar{1}1\}$, or $\{10\bar{1}0\}$ (**Fig. 12**). Intersected corners and edges of the older hopper represent the primary limb zones from which terraces extend into the cavities. Thus, unexposed interior corners and edges explain why terraces sometimes appear as 'floating chevrons' in the zoning pattern (e.g., **Fig. 11a** and

12). In sections far from the relic's center that roughly parallel a face direction or clip only cavity walls, the terraces appear as concentric pseudo-oscillations (**Figs. 8a, 10h, k, 11c** and **12**). Conversely, sections through dendrites intersect true rod-like primary and secondary branches, which attach at right angles or form exterior angles, much like those of a dendritic snowflake (**Figs. 9d, f, 10b, 11b** and **13**). Sections roughly perpendicular to the *c*-axis of both dendritic and hopper relics (also sections parallel or oblique to *c* of the latter) will create a snowflake semblance, but we surmise crystals like **Fig. 10b** preserve proper examples of dendritic 'arms' (Swanson and Fenn 1986). Finer dendritic overgrowths are also represented by the tiny faceted projections of thin 'wavy' zones coating older crystal surfaces (**Fig. 10j**). Because skeletal hoppers and dendrites theoretically lie on a continuous morphological spectrum, or represent transient stages along a morphological evolutionary path (Donaldson 1976; Lofgren 1974; Faure et al. 2003a, b, 2007; Swanson and Fenn 1986; MacLellan and Trembath 1991), they may mimic one another in some sections (compare **Figs. 12** and **13**). For example, oblique sections steeply inclined to stacks of hopper terraces or secondary dendritic branches may yield feathery zoning. Even where these morphologies cannot be discriminated, their fundamental implication is that they both signify rapid crystal growth.

Quartz arborescent CL zones and associated oscillations are always notably brighter and richer in Ti ± Al than juxtaposing zones. They even represent some of the brightest CL zones in some crystals (**Figs. 8, 10, 11**). Experimental work has shown that Ti solubility in quartz is a function of temperature (Wark and Watson 2006) and pressure (Thomas et al. 2010), thus relatively brighter CL (higher Ti) zones may indicate crystallization at relatively higher temperatures or lower pressures. The experiments of Huang and Audétat (2012) show that Ti as well as Li, Al, and Na uptake in quartz may also be influenced by melt composition and crystal

DOI: https://doi.org/10.2138/am-2020-6947

growth rate (also see models of Pamukcu et al. 2016). It is implausible that the higher CL intensity and Ti concentration of rapidly-grown quartz is a product of higher temperature formation than adjacent low CL intensity (Ti-poorer) polyhedral zones. Large cyclic pressure changes on the order of those described by Thomas et al. (2010) also cannot explain fine-scale rhythmic oscillations or multiple generations of arborescent zones spaced tens to hundreds of micrometers apart (**Figs. 8e, 9g, i** and **10e, h**; **Fig. 5a, d of App.**[3]). For these reasons, we propose the higher CL intensity of arborescent zones is best explained by (1) the incorporation of a boundary layer, whereby the rapidly advancing crystal surface incorporated slow-diffusing rejected elements accumulated in the liquid at the crystal-melt contact (extrinsic defects; **Fig. 14**; Kirkpatrick 1975; Swanson and Fenn 1986; Milman-Barris et al. 2008; Huang and Audétat 2012; Welsch et al. 2013), and very likely (2) intrinsic point defects imposed by rapid crystallization (**Fig. 14**; Götze et al. 2001 and references therein). In other words, lattice defects and the elements enriched in the engulfed boundary layer (having higher partition coefficients in quartz, most importantly Ti^{4+} and Al^{3+}) act as CL activators and fossilize parts of quartz that grew at high rates during strong undercooling and supersaturation (**Fig. 14**; cf. Huang and Audétat 2012; Welsch et al. 2013; Pamukcu et al. 2016). The defined shapes of arborescent frameworks indicate that excess trace element or defect incorporation occurred during non-equilibrium skeletal to dendritic growth; therefore, we suggest these relic luminescent structures are direct natural evidence for the effect of high crystal growth rate on impurity uptake and defect formation in magmatic quartz.

Accessory mineral inclusions. *Signs: Titanomagnetite crystals lie inside embayments and MIs adjacent to arborescent zones; Apatite micro-needles occur at arborescent zone boundaries.*

The concentration of rejected components in a boundary layer around a rapidly growing major phase may locally saturate accessory phases (Bacon 1989; Sunagawa 2005). During constitutional supercooling, the contacts of two phases may also be controlled by surface energy minimization through heterogeneous nucleation and heteroepitaxy (Hammer et al. 2010). Quartz-hosted titanomagnetite inclusions typically occur within the heads of embayments and are in contact with their walls (**Figs. 5c, 6l, m** and **10c**), implying not only that magnetite impeded quartz growth, but that it was likely anchored to quartz surfaces. This may also be true for the apatite micro-needles, which are embedded parallel to older growth surfaces. Both minerals can be found adjacent to the same boundary layer-derived arborescent CL zones (e.g., **Figs. 6l, m** and **10c**), and apatite needles are more frequent at these locations. Additionally, the stepped topography, subcrystals and twins of magnetite, as well as the acicular habit and glass inclusions of apatite are possible indicators of faster growth and supersaturation (**Fig. 6m**; **Fig. 6a, b of App.**[3]; Bacon 1989). Although the quartz-accessory mineral relations require further investigation, it is possible that titanomagnetite and apatite nucleated on or adjacent to rapidly growing quartz as slow-diffusing Ti and P (essential structural constituents) accumulated in a boundary layer at the advancing crystal-melt interface (Bacon 1989). Iron and Ca contents fall below detection limit and P was difficult to measure accurately in quartz (**Table 5 of App.**[1]). However, we expect that during crystallization of a boundary layer, the coupled substitutions required to incorporate Fe^{3+}, Ca^{2+}, and P^{5+} in the lattice would be less favored relative to those involving the more abundant Al^{3+} and the single substitution of Ti^{4+} for Si^{4+}. Thus, while some Ti within the boundary layer became incorporated into the growing crystal (hence, the Ti enrichment of arborescent zones; **Fig. 14**), a build-up of Fe, Ti, Ca, and P may have forced local supersaturation of titanomagnetite and apatite, which were subsequently enveloped by quartz.

Trapped melt. *Signs: Polyhedral layers fill interstices of arborescent frameworks, and host MIs; MI shape may mimic the shape of an overhanging crystal face or open skeletal cavity.*

Arborescent frameworks are encased by polyhedral layers (**Figs. 10–13**), indicating that burial of skeletal and dendritic crystals involved a morphology transition from hollow forms to replete faces. Positioning of MIs exclusively in the interstices of arborescent frameworks implies that quartz trapped melt as it infilled and hung faces above its cavities (**Fig. 15;** cf. MacLellan and Trembath 1991; Welsch et al. 2013, 2014). This explains why some melt inclusions mimic shapes of overhanging polyhedral faces (**Fig. 4i**; cf. Welsch et al. 2013). External faceting of the infill and crystal margins indicates slower, interface-controlled growth at lower degrees of undercooling (Kirkpatrick 1975; Hammer 2008), and in turn, suggests that rapid crystal growth followed by slower growth promotes melt entrapment in quartz (**Fig. 15**).

Melt inclusions may be sealed by two distinct polyhedral overgrowths: (1) darker CL, Ti-poorer infill that directly encases arborescent frameworks, or (2) generic, moderate CL oscillatory zoning, which mantles the posterior of infill (**Figs. 7** and **10–13**). Halos around MIs represent separate layers inside these polyhedral overgrowths, implying that secondary processes influenced inclusion formation. Three processes are interpreted based solely on CL, spatial relationships between the aforementioned features, as well as 2D and 3D considerations. Each is illustrated in **Figure 16a** and discussed hereafter.

(1) *Seal then fill*. The example discussed here focuses on what we commonly observe near arborescent zones. Like melt inclusions, halos occur between arborescent zones (**Fig. 16a**). They may abut, but do not crosscut them. Halos occur dominantly within dark CL infill and have matching CL intensities, suggesting they are the same in origin (e.g., **Figs. 10a, d**). Most halos appear homogenous, but ones with subtle zoning can show an inward (2D) shape transition from

triangular to circular, suggesting they were initially the shape of the skeletal cavity they lie at the center of (e.g., **Figs. 10d** and **11a;** compare with **Figs. 4i** and **9**). We therefore interpret these halos to represent post-entrapment crystallization of quartz on the walls of melt pockets after they were sealed (**Fig. 16a**). This is consistent with the observed correlation between inclusion size and halo size, which suggests the mass of quartz crystallizing on the walls is proportional to that of the original melt pocket. The facets of inclusion walls in contact with halos also signify the redistribution of material (e.g., **Fig. 10a, 11a,** and **16a**; Chesner and Luhr 2010).

(2) *Dissolve and refill*. Alternatively, halo margins can connect to a concentric dissolution surface across the crystal (e.g., **Fig. 10d**). These halos exhibit the same CL as the overgrowth outside the dissolution surface, indicating that dissolution and quartz reprecipitation sealed the inclusion. A caveat is that these melt inclusions may reside in locations of pre-existing inclusions or unit contacts. In **Figure 16a**, we illustrate the cluster of **Fig. 10d**, which contains two types of halos in contact with one another. The more interior halos match in CL and occur within relic hopper cavities (i.e. earlier post-entrapment crystallization). A second generation halo crosscuts one of the pre-existing halos, likely because dissolution acted preferentially at pre-existing, high-energy unit contacts nearby (see *Growth embayments*). This is evidenced by incision of the dissolution surface only where the two units meet; other parts of the cluster became rounded (cf. Manzini et al. 2017). Primary MIs can also occur between units lacking dissolution surfaces (e.g., **Fig. 10i**; see *Lineage of lattice defects*); however, those here were newly formed during the regrowth of quartz following dissolution.

(3) *Fill unsealed*. Some halos clearly connect to and match the generic CL zoning of the crystal mantle, indicating these melt pockets remained open and filled simultaneously with mantle growth (e.g., **Figs. 10c, l** and **16a**). This suggests the pockets were formerly embayments,

which may or may not have become sealed with continued growth. Portions of melt pockets (i.e. embayments) unsurmounted by polyhedral overgrowths could be associated with high densities of lattice dislocations that formed during rapid growth or slower infilling (Sunagawa 2005). An incomplete transition from skeletal to polyhedral growth can explain the smooth anhedral depressions ± embayments at the centers of crystal faces (**Fig. 4d, h, j, k**), as well as crystals that contain both hollow and replete faces (**Fig. 15**; also **Figs. 4d, j , k** and **6b, c, e, f**). In 2D, we observe that the overall shape of a crystal or cluster will partially retain that of its skeletal to dendritic foundation until the size ratio between the matured polyhedron and its internal skeleton reaches ~1.3:1; thereupon, the crystal begins to show recovery (**Fig. 10c**). Thus, slow infilling leads to a polyhedral quartz morphology, but inevitably leaves crystals blemished with internal voids due to the initial disequilibrium growth generated by high degrees of undercooling.

Growth embayments. *Signs: Growth zoning adapts to embayment margins; Embayments are positioned between arborescent zones or skeletal protuberances on crystal margins.*

Quartz embayments are commonly ascribed to resorption (e.g., Roedder 1979; Harris and Anderson 1984; Manley 1996; Bachmann et al. 2002; Molloy et al. 2008; Girard and Stix 2009; Wilcock et al. 2013; Allan et al. 2013; Seitz et al. 2018b; Befus and Manga 2019). However, from an energy standpoint, it would be difficult to detach atoms preferentially from the centers of planar crystal faces, locations where embayments often open. Therefore, locally accelerated dissolution on quartz surfaces is required for this interpretation. Bubble-driven dissolution has been proposed as a drilling mechanism to produce quartz reentrants (Donaldson and Henderson 1988; Befus and Manga 2019), but there is a lack of natural or experimental evidence that suggests bubble-drilling penetrates deep into quartz interiors. Furthermore, we find the evidence presented for bubble-drilling by Befus and Manga (2019) to be inconsistent with crystal stratigraphies in their CL images, wherein we see MIs/embayments between infilled hopper cavities (arborescent frameworks), MI halos of different origins, and zone adaptation to embayments containing magnetite and separating cluster units, consistent with stratigraphies of Toba quartz (**Figs. 7–12** and **16**). Alternatively, heating and dissolution might facilitate embayment formation in natural quartz (discussed in *Trapped melt* and hereafter), but experimental evidence suggests it should not. Superheating of experimental silicate melts causes quartz to develop rounded, embayment-free surfaces (Kuo and Kirkpatrick 1985; Donaldson 1985; Tsuchiyama 1986; MacLellan and Trembath 1991). On the other hand, dynamic crystallization experiments show that unstable, or rapid, crystal growth in supersaturated melts results in embayment formation (e.g., Donaldson 1976; Lofgren 1980; MacLellan and Trembath 1991). Some experimentalists have hypothesized that screw dislocations may also encourage their development even during polyhedral growth (Faure and Schiano 2005).

Embayments in Toba quartz are not late-stage reentrants, but were instead developed from the interior outward. The most compelling evidence is the adaptation or inward tapering of CL zones to embayment margins, which indicates their tubular shapes were acquired during continued crystal growth (**Figs. 7**; **Fig. 4 of App.[3]**; Laemmlein 1930; Blackerby 1968; Müller et al. 2000, 2002, 2009). If embayments originate by dissolution, they should cross-cut CL zones. We only find minimal cross-cutting relationships exclusively where older dissolution surfaces intersected and carved out walls of pre-existing MIs and unit suture boundaries (e.g., **Figs. 10d** and **16a**; **Fig. 4s of App.[3]**). High densities of lattice dislocations typically occur around MIs and at junctions of units or skeletal protuberances, making these areas energetically unfavorable and possible promotion centers for dissolution in an undersaturated melt (Sunagawa 2005). The concentric nature of dissolution surfaces substantiates that dissolution causes quartz to become externally rounded (e.g., **Figs. 7** and **10m**; **Figs. 3b, 4a, n, p** and **5a of App.**[3]), but we suggest it may locally act to minimize the high-energy of growth defects which outcrop at the crystal-melt interface (Sunagawa 2005). This can explain why slightly rounded units in some clusters are marginally unbound with locally cross-cut CL zones at their contacts—their sutures likely acted as dissolution pathways (**Fig. 10h**; **Fig. 3a of App.**[3]; cf. Fig. 8 of Milman-Barris et al. 2008). Thus, we contend embayment formation was never a direct causal effect of dissolution, but that dissolution sometimes occurred preferentially at features created by crystal growth.

Growth embayments are ubiquitous despite that not all crystals contain skeletal to dendritic foundations, multiple units, or growth impeding magnetite inclusions (**Fig. 4a–c, j–r of App.**[3]). Few crystals present the possibility of dissolution and regrowth, because embayments rarely originate from older dissolution surfaces (e.g., **Fig. 4m, s of App.**[3]). Some embayments delineate distinct skeletal protuberances and hopper cavities at crystal margins, formed during a late stage of rapid growth (**Fig. 6b, d**; **Fig. 4a–i of App.**[3]). These protuberances are larger than relic ones preserved in crystal cores (arborescent zones), and display adaptive, generic oscillatory zoning and poorly-zoned margins. Growth embayments that do not occur between distinct skeletal features, but rather border anhedral to polyhedral segments of quartz (**Fig. 4j–s of App.**[3]), require further explanation. Three possibilities are:

(1) If they are skeletal in origin, section plane orientation may prohibit their recognition as skeletal features. Sections cut roughly perpendicular to face directions may yield more definition to protuberances or hopper cavities than oblique sections (e.g., **Fig. 6d; Fig. 4a, b of App.**[3]).

(2) Still, some quartz segments in **Figure 4j–s of App.**[3] are unlike the faceted skeletal protuberances in **Figure 4a–i of App.**[3] (also see **Fig. 16b**). These segments tend to occur more frequently on larger macrocrysts and megacrysts; whereas, smaller macrocrysts and mesocrysts tend to exhibit pronounced skeletal features (**Fig. 6b–d** and **16b; Fig. 4a–i of App.**[3]). Theoretically, the radius of a crystal influences attachment kinetics and crystal interface stability phenomena, depending on the degree of undercooling, diffusion, and crystal growth rate (Kirkpatrick 1975 and references therein). Numerical modeling shows that larger crystals (≥1 mm radius) may not record the effect of increased undercooling as much as smaller crystals (Hort 1998). A simple explanation is that larger radii crystals with larger surface areas should require more time or sustained undercooling (due to far more molecules needed) to develop skeletal protuberances proportional to their overall crystal size, as compared to smaller crystals (**Fig. 16b**; Kirkpatrick 1975; Kuroda et al. 1977). Thus, skeletal overgrowths on large polyhedral crystals may sometimes deviate from what we typically identify as a skeletal texture (e.g., sharp disequilibrium textures in quenched experimental melts or lavas). This idea, in turn, implies that different coexisting crystal sizes may record rapid growth differently (**Fig. 16b**; compare **Fig. 4a–i** with **4j–s of App.**[3]). We also consider crystal growth and protuberance morphology as a function of time (Swanson and Fenn 1986). For example, Welsch et al. (2014) interpreted the curvature of matured olivine dendrites to signify a transitional morphology between dendritic and polyhedral growth. The anhedral to partly faceted lobes on some quartz margins may also indicate an incomplete transition from skeletal to polyhedral morphology (**Fig. 4 of App.**[3]**;** also **Fig. 4d, h, j, k**). Thus, infilling (slower growth and faceting; a change in growth mechanism) may initially aid in defining large protuberances we can recognize as skeletal, but if prolonged, it will eventually obscure them as a crystal restores polyhedral forms (consider **Fig. 16b**).

(3) Due to their high crystallinities, Toba magmas were likely volatile saturated by the time quartz exteriors grew, especially if rapid crystallization had occurred (second boiling). As an alternative, if pre-eruptive bubbles existed in the melt and were able to attach to quartz surfaces, quartz might form embayments by growing around bubbles (Müller et al. 2000). However, MI decrepitation makes it difficult to determine if quartz ever trapped pre-eruptive bubbles, while vesicles in glass-filled embayments likely reflect syn-eruptive melt vesiculation. Bubbles that are preserved in some intact MIs have volumes proportional to those of their host inclusions, and are therefore considered post-entrapment shrinkage bubbles (Chesner and Luhr 2010). Because there are ample crystals with skeletal margins in our samples, we hypothesize that quartz embayments dominantly formed as a direct result of unstable crystal growth related to an early or late, pre-eruptive period of disequilibrium conditions (**Fig. 16b**; **Fig. 4 of App.**[3]).

Dendritic buds and growth twins. *Signs: Parallel crystal units have (and can share) arborescent core zones, near-identical growth patterns, and similar morphology...; Twinned units have similar sizes, growth patterns, ± arborescent core zones...*

Arrangements of grouped quartz units in dominantly parallel to sub-parallel and twin orientations indicate a crystallographic control on the assembly of clusters (**Table 3 of App.**[1]; **Figs. 8, 10, 11**). Synneusis is said to often produce such preferred alignments through a union of suspended crystals and adherence of their prominent faces (Gaubert 1896; Vogt 1921; Vance 1969; Schwindinger and Anderson 1989; Schwindinger 1999; Schaskolsky and Schubnikow 1933; Nespolo and Ferraris 2004). Synneusis caused by gravitational crystal settling, accumulation, or compaction has been invoked to explain organized quartz clusters in plutonic rocks (Beane and Wiebe 2012; Graeter et al. 2015). This would require pyramidal faces of separate polyhedral dipyramids to bond together through a precise alignment of their lattices in parallel or Esterel twin orientations (positions of minimal interfacial energy; Vance 1969), the latter of which is permitted by a paralleling of the contact twin plane ($10\bar{1}1$) and pyramidal face direction $\{10\bar{1}1\}$ (Friedel 1933; Nespolo and Ferraris 2004; Grimmer 2006; Beane and Wiebe 2012). Synneusis then requires the assumption that Esterel twins do not form from twinned nuclei, while it cannot explain Verespatak (Japan) twins that exclusively form by growth twinning (**Fig. 3**; Frondel 1962). Importantly, these particular twin laws are two of the most common and are often associated in nature (Drugman 1927; Frondel 1962; Watanabe 1974; Sunagawa et al. 2004; Grimmer 2006). In section, any size-shape disparities between grouped units, or dissimilarities and spatial offsets of their core zones, are not prima facie evidence of synneusis (cf. Beane and Wiebe 2012), as they are commonly effects of off-center sectioning (e.g., **Figs. 8a, e,** and **10h**; **Fig. 3a, b of App.**[3]; Dowty 1980b; this study). In both single and serial sections, similarities in size and zoning patterns among units in an overwhelming number of quartz clusters is striking and cannot be coincidental (**Figs. 5a, 8, 10,** and **11c**). We reason this by the wide range of crystal sizes (<1–20 mm) coexisting, and the inability to correlate individual CL zones between single crystals, or between crystal units in different clusters. Therefore, the probability that multiple (e.g., four or five; **Fig. 8a**; **Fig. 3a of App.**[3]) separate similar-sized quartz crystals with virtually identical CL zoning patterns would meet and attach systematically by synneusis is implausibly low (cf. Welsch et al. 2013). While crystal settling and accumulation would increase the probability of crystal contacts (Bachmann and Bergantz 2004), the high melt viscosity is likely to limit the ability of two faces to achieve the proper closeness, positioning, and orientation needed for atomic bonding (Dowty 1980b). Furthermore, the energy barrier that would avert numerous spontaneous rotations of multiple touching quartz into perfect parallel or twin alignments is prohibitively high in a viscous rhyolite melt (Brugger and Hammer 2015). Altogether, we suggest the quartz clusters are not a result of crystal aggregation by synneusis.

We ascribe their crystallographic organizations primarily to dendritic growth and growth twinning. Clusters frequently preserve relic skeletal to dendritic morphologies (arborescent zones) at the centers of crystal units (**Figs. 8–13**), suggesting at least some and potentially all units in many clusters grew rapidly upon or soon after nucleation. Analogous to a manner in which olivine grows dendritically, parallel quartz units may represent subcrystals, or buds, developed from a single lattice through replicated overgrowths of crystallographically aligned hopper units (Donaldson 1976; Faure et al. 2003a, b; Welsch et al. 2013, 2014, 2016). Evidence among parallel units that collectively supports dendritic budding includes their (1) simultaneous extinction under crossed-polars (**Fig. 6b, e–g, k**), (2) nearly identical core-to-rim growth patterns (e.g., **Figs. 8a, 10c,** and **11c**) (3) similar habits and external skeletal to polyhedral morphologies, (4) similar sizes, or a decrease in unit size away from the cluster center (e.g., **Figs. 5a** and **10g**; cf. Welsch et al. 2013), (5) elongation of the prism form consistent with growth being fastest along [0001] (e.g., **Figs. 6b, e,** and **8a, e**; Swanson and Fenn 1986; MacLellan and Trembath 1991), (6) penetrative nature and resemblance to a single hexagonal crystal shape (e.g., **Figs. 5a, 6b, 8a,** and **10c, f, g, i**), and (7) continuation of Dauphiné twin boundaries across unit boundaries, which indicates a mutual crystal lattice (**Fig. 8a, b, e**). Also of significance are fortuitously oriented, oblique sections that show parallel units having mutual interior limbs and branches, which we contend is unequivocal evidence for dendritic growth (**Fig. 10c, g**; **Fig. 5h of App.**[3]). Welsch et al. (2013, 2014) also show that P-rich feathery zoning exists near cores of parallel olivine units, which also exhibit such connections. We point out, just as they do, that most 2D sections do not reveal the interconnectedness of parallel units formed by dendritic budding. Thus, we assume their arborescent zones likely connect in the third-dimension and are a part of the same crystal lattice and dendritic framework, which is plausibly defined by hopper overgrowths inside or along the upper parts of first generation hopper cavities (Faure et al. 2003a, b; Welsch et al. 2013, 2014; compare **Fig. 10c, g** with **Fig. 15**). In contrast, units attached in Verespatak or Esterel twin orientations are not buds, because the lattices of the units are mirrored respectively in $\{11\bar{2}2\}$ and $\{10\bar{1}1\}$ (Grimmer 2006) (**Fig. 3**). However, because both parallel and twinned units can occur within the same cluster and can have similar sizes and intra-core arborescent zones, we surmise that their crystallization was concurrent (cf. Welsch et al. 2013). Strikingly similar to dendritic olivine twins, quartz twins often have their own buds, which are attached replicas paralleling the twin orientation (e.g., **Fig. 8b, d**; Welsch et al. 2013). These characteristics lead us to suggest that Verespatak and Esterel twins, occurring as both single pairs and as units attached to groups of parallel units, must represent nucleisupersaturation twins if twin individuals are essentially of equal size (Buerger 1945; Sunagawa 2005). Therefore, we interpret twinning to signify nucleation errors developed early in the lattice structure due to higher rates of crystal nucleation and growth (Buerger 1945; Sunagawa et al. 2004; Welsch et al. 2013; Brugger and Hammer 2015). We emphasize that twinning is a common phenomenon in minerals, and it alone does not necessarily imply rapid growth (e.g., Brugger and Hammer 2015). High driving force conditions increase the probability of defect and twin formation (Buerger 1945; Sunagawa 2005). Thus, when twins are prevalent and concurrent with other indicators of rapid growth, they may be linked to high degrees of undercooling and supersaturation (Brugger and Hammer 2015).

Seeded and epitaxial intergrowths. *Signs: Small crystal units occur at corner or edge positions within the margins of large clusters; Small and large units lie in twin or parallel orientations.*

Other intergrowth-forming processes are only evident in macrocrystic and megacrystic clusters that incorporated small units during late stages of growth. These marginal units lie in parallel or twin orientations with the megacryst trunk and are attached near crystal corners or edges of the larger units (**Figs. 6f, 8e**; **Fig. 3a, b of App.**[3]). Serial sections of the megacryst in **Figure 8e**, for example, show that a matured skeletal Verespatak twin, three small parallel units, and a thin skeletal overgrowth concentric to the megacryst mantle are nearly stratigraphically equivalent. From this, we infer that formations of twins and parallel units with highly unequal sizes and distinctly different growth patterns can be better explained, respectively, by (1) seeded twin growth through a mismatch of atomic positions on pre-existing crystals, and (2) preferential nucleation and homoepitaxial growth on pre-existing crystal corners and edges, both driven by a new stage of high-supersaturation (Sunagawa 2005). These processes may be applicable to smaller clusters, but could be subordinate, as the majority exhibit characteristics explainable by dendritic budding or growth twinning. In fact, growth twinning is energetically more achievable at the nucleation stage (Buerger 1945; Sunagawa 2005; Brugger and Hammer 2015), and the twinned quartz mesocrysts in **Figure 6j** and **Figure 3c–e of Appendix**[3] attest that twinning occurs in very early stages of quartz growth (also see **App.**[4]). Additionally, recurring twin planes in single clusters are also plausible at high supersaturation (Sunagawa 2005; Brugger and Hammer 2015), although multi-component twinning could also result from heterogeneous-like nucleation of twins. The latter should be evidenced by a distinct and non-systematic grain size difference among units that can be verified through serial sectioning (Drugman 1927).

Regardless of these various complex processes that may contribute to cluster construction, our observations and data lead us to suggest that it may be powered exclusively by higher rates of crystal nucleation and growth under high driving force conditions.

Lineage of lattice defects. *Signs: Parallel or twinned units show measurable misorientation; Occurrences of subgrain boundaries, melt lenses at unit contacts, and Dauphiné twins.*

The mechanisms forming quartz clusters produce or predispose them to a number of other crystal defects worth noting. Optical and EBSD measurements of unit orientations show that units may be offset a few degrees from ideal parallel or twin relation (e.g., **Fig. 6g, k**; **Table 3 of App.**[1]). Quartz clusters in plutonic lithologies also show consistent unit offsets in EBSD data (Beane and Wiebe 2012; Graeter et al. 2015), as do highly systematic groupings of dendritic olivine (Welsch et al. 2013). Such slight misorientations have been formerly cited as evidence of synneusis (Vance 1969 and references therein), distortions related to the β-α quartz transition (Beane and Wiebe 2012; Graeter et al. 2015), or intracrystalline deformation (Carter et al. 1986; Helz 1987; Beane and Wiebe 2012). Alternatively, we propose unit offsets are most likely the result of lattice defects created during early rapid crystallization (Sunagawa 2005; Welsch et al. 2013). Defective boundaries or lattice mismatches are indicated by subgrain boundaries or dislocation planes (e.g., **Fig. 6g, k**), as well as narrow melt lenses (i.e. areas unfavorable for atomic attachment) that appear to have formed as faces of slightly misoriented units tried to meld together throughout growth (i.e. planar defects) (e.g., **Figs. 8d,** and **10f, i**; Sunagawa 2005; Welsch et al. 2013). Dauphiné twins are also defects superimposed on parallel units and contact twins (**Fig. 8**), a phenomenon that is quite common for the latter (Sunagawa et al. 1979; Lenart et al. 2012; Xu et al. 2014; Momma et al. 2015). Dauphiné twin formation by primary growth is limited to α-quartz, but can occur secondarily under mechanical stresses or transformation from β- to α-structure (Frondel 1945). Because of their ubiquity, a secondary origin is probable and could be related to MI bursting or strain induced by rapid cooling through the β-α inversion (Frondel 1945). Conceivably, various pre-existing high-energy growth defects (i.e. contact twin boundaries, planar defects, screw dislocations, impurity and point defects, MIs, etc.) increased the susceptibility of crystals to additional lattice imperfection.

Conditions of rapid quartz growth

Our investigation identifies disequilibrium, skeletal to dendritic crystal growth traceable through intricate relationships between prominent quartz textures. The crystallization of skeletal and dendritic quartz requires specific thermodynamic conditions (Swanson and Fenn 1986); therefore, quartz morphologies can be used to reconstruct crystal origins and the history of the host magma. Crystallization experiments using natural and synthetic silicate melts show that quartz morphology can be directly related to the degree of undercooling ($\Delta T = T_{\mathrm{liquidus}} - T_{\mathrm{melt}}$) at various pressures and water contents (e.g., Lofgren 1971; Swanson 1977; Fenn 1986; Swanson and Fenn 1986; MacLellan and Trembath 1991; London 1992, 2009; Baker and Freda 2001). Generally, quartz forms a polyhedral morphology at small ΔT, but develops skeletal to dendritic morphologies as ΔT becomes increasingly larger than ~50°C, or when cooling rates exceed ~2°C/hour (Swanson and Fenn 1986).

Experiments collectively show that skeletal or hopper dipyramids are characteristic of quartz crystallizing at moderate undercoolings (ΔT > ~40–50°C), whereas dendrites form at large undercoolings (ΔT > ~50–100°C) (Swanson and Fenn 1986; MacLellan and Trembath 1991). Experiments focused on textural development at pressures appropriate for rhyolitic systems are limited. Therefore, we focus on results of the 1 kbar experiments of MacLellan and Trembath (1991) wherein H_2O was maintained at or below 4 wt% for granitic melts, as well as similar 2 kbar experiments of Swanson and Fenn (1986), as these represent minimum conditions we infer for Toba magmas (Chesner 1998; Chesner and Luhr 2010) and are consistent with other rhyolitic systems (Gualda and Ghiorso 2013 and references therein). Both experimental studies produced a similar morphological range of quartz by inducing similar degrees of undercooling, but MacLellan and Trembath (1991) thoroughly documented that morphologies are equally dependent upon ΔT, crystallization duration (*time*), and melt composition. More specifically, their isothermal experiments show complexity: multiple quartz morphologies (i.e. polyhedral, anhedral, and skeletal dipyramids; granophyric, micropoikilitic, and spherulitic intergrowths with feldspar), which increased in number and often coexistence with increased durations of large ΔT (their Figs. 3 and 6). This led MacLellan and Trembath (1991) to infer that a melt cooling continuously at a constant moderate to high rate may crystallize two or more morphologies sequentially without a major change in temperature, pressure, or volatile content. They also show that cooling rate and melt composition (Ab- versus Or-rich) may govern the sequence in which some quartz morphologies develop (their Fig. 5). MacLellan and Trembath (1991) suggest that multiple quartz morphologies can form through two processes: (1) one morphology evolving into another during continued growth of early crystals (**Fig. 15**; also Swanson 1977); and (2) sequential crystallization of different morphologies occurring synchronously with the aforementioned process. Their descriptions of textural modification (i.e. the transformative sequences of polyhedral dipyramids → anhedral quartz → skeletal quartz; and skeletal quartz → polyhedral dipyramids with MIs and embayments) are remarkably in line with the textures and inferred growth processes we describe for Toba quartz (**Figs. 9–13** and **15**).

We infer based upon experimental studies that a minimum undercooling of ~50–100°C was required for skeletal and dendritic quartz morphologies to develop in melts of Toba compositions (**Fig. 17**; MacLellan and Trembath 1991; Swanson and Fenn 1986). Only in the most-evolved, fine-grained YTT pumice and dome samples (T-5B and TT-2) are there granophyric quartz-feldspar intergrowths (**Figs. 2** and **5j, k of App.**[3]), a sign that these melts experienced a much stronger degree of undercooling (ΔT > 100°C) or crystallized at large ΔT for a relatively longer duration (**Fig. 17**; Fig. 6 of MacLellan and Trembath 1991). Additionally, melt composition likely played a role in the development of this particular texture (MacLellan and Trembath 1991). Given that quartz is not the first phase to crystallize in this near-eutectic system, other mineral phases, such as feldspars, are expected to also record such strong undercooling. In addition to granophyric intergrowths, single crystals and monomineralic clusters of plagioclase, sanidine, and some mafic phases show abundant textural-chemical evidence of disequilibrium (some textures observable in **Fig. 2 of App.**[3]). Ongoing work aims to collectively interpret characteristics of quartz and these minerals to more accurately reconstruct crystallization conditions and the degree of undercooling. Because quartz is simpler structurally and less susceptible to structural and chemical modification (MacLellan and Trembath 1991), its textural record forms the most reliable foundation for understanding the cooling histories of Toba melts.

Determining the specific process(es) that drove magma undercooling is beyond the breadth of this study, as it too requires consideration of other phases and may warrant experimental investigation. However, strong degrees of undercooling can be readily generated by a decrease in magma temperature upon contact with a cooler environment or cold country rock (i.e. conventional ΔT). Undercooling can also increase through a rise in the liquidus temperature during volatile exsolution (i.e. effective undercooling, ΔT_{eff}), a process that usually accompanies magma decompression or ascent (e.g., Hammer and Rutherford 2002; Hammer 2008). Alternatively, phase supersaturation can be achieved through a change in melt chemistry during magma mixing or assimilation (e.g., Castro 2001). Because skeletal and dendritic quartz can develop in H_2O-saturated or H_2O-undersaturated melts and at various pressures (Swanson and Fenn 1986; MacLellan and Trembath 1991), the consideration for either set of conditions, concurrent with or exclusive of one another, is tenable (we leave ΔT unspecified here for this reason). The textural transformations recorded in quartz should provide vital clues to the origin of its rapid growth and are discussed hereafter.

Origins of textural transformations beneath Toba

Sections of the quartz stratigraphy that record changes in crystal morphology are critical for deciphering and constraining processes that led to rapid quartz growth. Here, we discuss implications of the scale, location, and sequence of morphological transformations in relation to CL intensity across the transitions (also see **App.**[4]). We test the applicability of experimental results in finer detail where possible, and in turn, interpret causation for each type of transformation.

Early rapid growth (polyhedral → skeletal or dendritic). The regular occurrence of hopper and dendrite relics at the cores of single crystals and grouped units indicates that skeletal to dendritic growth was characteristic of early stages of quartz crystallization (**Figs. 7–13** and **15**). This can be explained by an initial lag in quartz nucleation upon sudden disequilibrium, followed by a nucleation event and subsequent pulse of rapid growth (e.g., Swanson 1977; Swanson and Fenn 1986; Dowty 1980b; MacLellan and Trembath 1991; Hort 1998; Milman-

Barris et al. 2008; **Fig. 18a**). Hopper relics themselves mantle a ≤300 μm faceted zone, implying that crystals initially grew with polyhedral morphologies (**Figs. 9–13** and **15**). This morphology sequence also appears in MacLellan and Trembath's (1991) experiments, wherein skeletal morphologies evolved from continued growth of earlier dipyramids during prolonged undercooling and under a range of cooling rates. Therefore, such an early transformation in Toba quartz was likely short-lived and occurred in situ (**Fig. 18a**).

Portions of each precursory polyhedral 'seed' may indeed preserve a conformable relation to the pulse of rapid growth. These portions include euhedral zones rooting arborescent zones, and the periodic oscillations that precede them (**Figs. 9–13** and **18a**). Because the oscillations exhibit periodicity, display a higher CL intensity matching that of arborescent zones, and can cycle back and forth with arborescent zones (**Fig. 9g, i**), we interpret them to also represent entrapped boundary layers with defects (**Fig. 14**). Huang and Audétat (2012) and Pamukcu et al. (2016) show that absolute concentrations of Ti, Li, Al, and Na in quartz increase with increasing crystal growth rate. Thus, we interpret the Ti-richer and -poorer oscillations to reflect cyclic ramp-ups and lulls in growth rate (**Fig. 18a**). Whereas, the Ti-richer 'root' zone may mark a final pulse in growth rate that increases enough to sprout terraced or branching tips (**Figs. 12, 13** and **18a**; Swanson and Fenn 1986). This interpretation would imply that the incorporation of a melt boundary layer (and increase in defect density) does not require development of skeletal and dendritic morphologies, and is in accord with crystal-growth theory that predicts changes in growth mechanism induce changes in morphology (Kirkpatrick 1975 and references therein). If correct, this early transformation involved two conformable styles of growth: (1) sequential layer addition (tree-ring style) followed by (2) preferential growth of crystal corners and edges (**Fig. 18a**). Single or recurring transitions from the former (1;

polyhedral oscillating zones) to the latter (2; arborescent zones) would imply progressive or oscillating changes in growth mechanism, respectively (**Fig. 9 g, i**; e.g., Welsch et al. 2013; Faure et al. 2007). Again, such changes would reflect shifts in growth rate as an effect of undercooling at the crystal interface (Swanson 1977; Swanson and Fenn 1986). Thus, increasing ΔT may explain a single transition from polyhedral to skeletal or dendritic overgrowths, whereas fluctuations in ΔT or latent heat build-up and removal along the crystal surface may explain transient oscillations of 'ramp-ups', 'lulls', and skeletal to dendritic overgrowths (e.g., **Figs. 9g, i, 10e, h, 14** and **18a**; Kirkpatrick 1975; Welsch et al. 2009, 2013; Colin et al. 2012).

Further, we speculate whether inter-crystal variation in zoning patterns within hopper and dendrite core relics also results from variability in melt evolution at a local scale (i.e. the crystal-melt interface). Other than within clusters, we do not observe any two cores having followed the exact same cooling or morphological path (**Figs. 10** and **11**). Analogously, just as no two snowflakes that have fallen from the same cloud look alike (Libbrecht 2005), we expect that early skeletal to dendritic quartz too record locally unique, although broadly similar, trajectories in melts at disequilibrium conditions.

Cessation and two-stage recovery (skeletal or dendritic → polyhedral x 2). The cessation of fast diffusion-controlled growth is marked by the infilling of skeletal to dendritic crystals with dark CL, Ti-poorer quartz (see *Trapped melt*; **Figs. 10–15** and **18a**). This first stage of recovery may correspond to the infilling of skeletal crystals in MacLellan and Trembath's (1991) experiments of longer durations at moderate to large ΔT, or at moderate cooling rates (**Fig. 17**). With continued crystallization, their skeletal crystals tended to evolve to anhedral morphologies (reduced faceting); whereas, the dark infill here is typically faceted above cavities (e.g., **Fig. 10a**). Terminal faceting of the earliest infill is consistent with slower polyhedral growth, while its poorly- to non-zoned nature implies it grew under invariant conditions, possibly in situ soon after skeletal to dendritic growth ended (**Fig. 18a**).

Additionally, the total impurity content and lower Ti concentrations of the dark CL infill may provide clues to a magmatic environment that seeded fast crystallizing quartz, which is otherwise masked by the incorporated melt boundary layer and intrinsic defects. Because early skeletal to dendritic crystals (core relics) grew to a common size (~0.5–1 mm diameter) before their primal 'dark recovery stage', their growth was probably slowed by a pervasive and systematic process. Melt boundary layers may poison crystal faces to the point of slowing their growth (e.g., Swanson and Fenn 1986; Colin et al. 2012; Welsch et al. 2013); but this may be implausible as a dominant process for quartz given that the melt itself is primarily SiO_2. Alternatively, it is probable that the burst of crystallization upon high undercooling led to a regional build-up of latent heat in the magma (**Fig. 18a**), which could eventually halt rapid crystal growth and allow slower growth to take over in situ (Kirkpatrick 1975; Hort 1998). Evolution of the melt composition during the mass of crystallization would progressively lower $T_{liquidus}$ of quartz and hence ΔT over time as it approaches equilibrium, a process that could also contribute to the decay of crystal growth rate (Kirkpatrick 1975; Swanson and Fenn 1986; Baker and Freda 2001; Hammer and Rutherford 2002; Nabelek et al. 2010). Infilling, however, indicates undercooling remained great enough to permit crystallization. Therefore, the dark infill could signify the melt's approach to thermal equilibrium and eutectic conditions (**Fig. 18a**; Swanson and Fenn 1986). Such a series of processes would account for the absence of unmodified hopper and dendritic crystals in the erupted magmas.

Stratigraphically above the dark CL infill lies the generic CL zoning of Toba quartz, characterized by subtle oscillatory patterns in moderate gray shades (**Figs. 10–13, 16a,** and **18a**).

Contacts between dark infill and this second-stage polyhedral overgrowth can be either flat (conformable) or rounded (possibly non-conformable), implying that the faceting of dark infill did not always complete (cf. MacLellan and Trembath 1991; Welsch et al. 2014) or that the infill occasionally dissolved prior to growth of generic polyhedral exteriors (e.g., compare **Figs. 4j, k, 10a,** and **11c**). Presuming that the first stage of polyhedral overgrowth (infill) occurred in situ, the second stage generic overgrowth likely marks the point at which matured skeletal and dendritic crystals physically left the environment they formed in, or when that environment attained conditions typical of the system (**Fig. 18a**).

Intermittent rapid growth (polyhedral → dendritic). Fine dendritic overgrowths ('wavy' zones) or tips reflect a severe change in morphology due to an abrupt increase in growth rate (e.g., **Figs. 10j and 11b**; Swanson and Fenn 1986; MacLellan and Trembath 1991). Because these Ti-richer relics interrupt the generic zoning pattern of crystal exteriors, show a reduction in scale, and are coated with dark CL infill, we interpret them to represent the response of pre-existing polyhedral crystals to a pulse of strong undercooling (**Fig. 18b**). Thus, it is possible that transitions from large planar crystal surfaces to finer dendritic morphologies temporally correspond to nucleation and growth of early skeletal to dendritic crystals (**Fig. 18a, b**). The single crystals and clusters that show both early and intermittent morphology transformations may record multiple undercooling events (e.g., **Fig. 10f**; **Fig. 5d of App.**[3]), consistent with our idea that multiple generations of hopper or dendrite relics formed in order to explain why they occur in a wide range of coexisting crystal sizes (0.5–20 mm) (e.g., compare **Fig. 10a** and **m**).

Late rapid growth (polyhedral → skeletal). Growth protuberances delineating sinuous crystal margins signal disequilibrium during the latter stages of magma crystallization (**Fig. 16b** and **18c; Fig. 4 of App.**[3]). Their formation is fundamentally different from any other morphology transformation in that it is often relatively much larger in scale and unassociated with arborescent CL zones. Instead, there is no interruption in generic oscillatory zoning across the transition into protuberances, apart from zone adjustment to embayment walls (**Fig. 16b** and **18c; Fig. 4 of App.**[3]). These characteristics are interpreted collectively as signs of a more gradual transition from polyhedral to skeletal morphology, possibly related to a moderately lower degree of undercooling or cooling rate, and thus relatively slower growth rate (**Fig. 18c**; MacLellan and Trembath 1991). With their growth seized by eruption, these exterior skeletal protuberances likely represent disparate morphoses reflecting different stages of polyhedral recovery (see *Growth embayments*).

A relevant question here is: whether this type of skeletal growth contributes to large crystal growth? Large crystal sizes are, in part, a consequence of grouped crystal units growing together, many of which initially grew rapidly. Although megacrystic clusters are likely older than mesocrystic ones, for example, megacrysts may not be necessarily “old”. Swanson (1977) shows experimentally that large (several mm) crystals in supercooled granitic melts do not need long periods of time to form. Experiments also show that seeded and twinned nuclei grow at faster rates than unseeded and non-twinned ones (Cahn 1954; Swanson 1977). Additionally, Nabelek et al. (2010) demonstrates that if water is retained in an undercooled system because it cannot be efficiently vented, growth of large crystals may occur at cool temperatures, and even below the equilibrium solidus (Jahns and Burnham 1969; Baker and Freda 2001). Because exteriors of macrocrysts and megacrysts often contain a wealth of growth embayments and matured? skeletal appendages, perhaps a specific set of conditions (T, P, H_2O, ΔT) may have facilitated growth of large quartz beneath Toba.

How fast did quartz grow?

Studies seeking to extract time information from quartz crystals are increasing (e.g. Gualda et al. 2012b; Seitz et al. 2015; 2018b; Pamukcu et al. 2015, 2016). A critical variable of interest is crystal growth rate, which has been investigated experimentally (e.g., Swanson 1977; Swanson and Fenn 1986; Baker and Freda 2001; Huang and Audétat 2012), through models (e.g., Baker and Freda 2001; Pamukcu et al. 2016), melt inclusion faceting (Pamukcu et al. 2015), and Ti diffusion chronometry (e.g., Gualda and Sutton 2015; Seitz et al. 2015). Because experimental studies agree that crystal morphology is a function of growth rate and the diffusion of crystal-forming components in the melt (e.g., Kirkpatrick 1975; Swanson 1977; Lofgren 1974, 1980; Swanson and Fenn 1986), the skeletal to dendritic morphologies observed here offer a qualitative reference from which to assess quartz growth rates obtained through different methods. Consequently, these textures may help constrain the timescales of quartz growth.

Here, we review previously determined growth rates, paying particular attention to those measured experimentally for skeletal to dendritic quartz (e.g. Swanson and Fenn 1986), and those used to model the effect of quartz growth rate on boundary layer development in rhyolitic melt (Pamukcu et al. 2016). Quartz growth rates are on the order of 10^{-10} m/s (parallel to *c*) in experiments that produce skeletal and dendritic morphologies (Swanson and Fenn 1986; Baker and Freda 2001). These are minimum values considering nucleation lag times; although water in the system may effectively lower these rates (Swanson 1977; Swanson and Fenn 1986; Baker and Freda 2001). Experiments consistently document that with increasing undercooling, crystal growth rate increases to a maximum, and then decreases with time (i.e. diffusion-controlled growth exhibits time-dependent behavior). Thus, growth rate may vary by orders of magnitude (10^{-12} to 10^{-9} m/s at minimum) during a period of high undercooling, and may be exemplified by the crystal morphology transitions observed here and in experiments (*see previous section*; Swanson and Fenn 1986; MacLellan and Trembath 1991). Interestingly, numerical models of Pamukcu et al. (2016) show that time-dependent boundary layer enrichment occurs at growth rates faster than 10^{-10} m/s, consistent with the minimum growth rates required to form skeletal to dendritic quartz in experiments. Assuming that skeletal to dendritic quartz growth in Toba magmas led to crystallization of melt boundary layers, it seems appropriate to use a minimum growth rate of 10^{-10} m/s to calculate possible timescales of 'rapid' quartz growth.

We focus our calculations on skeletal to dendritic relics delineated by zones enriched in Ti (a factor of ~1.3–1.5) because we expect these features represent the most rapidly grown portions of quartz (**Figs. 9–13**). As previously described, these relics usually represent overgrowths on a ≤300 μm polyhedral 'seed' at the cores of single crystals or crystal units, signifying that a severe morphology change followed nucleation. Therefore, a linear growth rate from core-to-overgrowth margin cannot be assumed. We simply divide the core into two parts: the inner polyhedral 'seed', and the skeletal-dendritic overgrowth, and measure the length of the overgrowth parallel to the *c*-axis (e.g., **Figs. 10a, b** and **11a**). Growing at a rate of 10^{-10} m/s, the ~0.05–1 mm skeletal-dendritic portions alone would have formed within 1 week to 4 months. If faster growth rates apply, their growth times are of course much shorter: on the order of hours to weeks. Other portions of quartz crystals likely grew at rates orders of magnitude slower as indicated by polyhedral morphologies (e.g., 10^{-14} to 10^{-11} m/s; Gualda et al. 2012b; Pamukcu et al. 2015; Seitz et al. 2015), thus the overall timescale of quartz growth at Toba is expected to be much longer.

IMPLICATIONS

Recognizing quartz textures as disparate manifestations of rapid crystallization challenges our current understanding of the crystal record, and has implications for analytical approaches and the models of large silicic magma bodies.

- Many textures observed in this study (such as embayments, “jagged CL zones” richer in Ti, and clusters) are common to quartz in silicic rocks, and have been formerly taken as direct signs of crystal dissolution caused by added heat or volatiles amid magma recharge (Bachmann et al. 2002) or decompression (Seitz et al. 2018b), the assimilation of xenocrysts (Liu et al. 2006), and synneusis forced by turbulence, crystal accumulation, compaction, or melt expulsion from a mush (Vance 1969; Beane and Wiebe 2012; Wilcock et al. 2013; Graeter et al. 2015). Our study demonstrates that such processes are either not applicable to or solely responsible for these ubiquitous textures in Toba rhyolites. Instead, we suggest that a single process of rapid disequilibrium crystallization resonates through an array of prominent quartz textures related by skeletal to dendritic growth. Consequently, we recommend a reevaluation of the timing or extent to which quartz texturally records thermal rejuvenations, decompression, assimilation, crystal gathering, and mush dynamics.

- A correspondence between relic skeletal-dendritic morphologies and increased trace element concentrations (Ti, ± Al…) in natural quartz suggests that high crystal growth rates lead to incorporation of a melt boundary layer in the lattice structure (also see Huang and Audétat 2012; Pamukcu et al. 2016). Preservation of a skeletal-dendritic morphology (i.e. its illumination and delineation in CL) presumably owes to the presence of impurities (primarily Ti based on current measurements); however, because rapid crystallization may introduce additional point defects (Götze et al. 2001 and references therein), the total CL intensity may be influenced by both extrinsic (impurity) and intrinsic defects. Collectively, these processes have major implications for the applications of Ti-in-quartz thermobarometry (Wark and Watson 2006; Thomas et al. 2010; Huang and Audétat 2012) and Ti diffusion modeling (Matthews et al. 2012b; Seitz et al. 2015, 2018b; Gualda and Sutton 2016). These petrologic tools assume parameters such as magma temperature, $aTiO_2$, or growth rate to be constant, that CL variations are primarily due to Ti zoning, or that crystal compositions reflect chemical equilibrium with the melt, all of which could be problematic when studying portions of crystals grown at high rates. In addition, our study finds that skeletal to dendritic crystal growth promotes melt entrapment in quartz, and that continued infilling leads to crystallization on the walls of some inclusions after they have been sealed. Because anomalous MI compositions in quartz are commonly documented (e.g., Liu et al. 2006; Chesner and Luhr 2010; Bégué et al. 2014), establishing their textural context is crucial in determining if quartz entrapped representative aliquots of its host melt versus melt boundary layers, or if post-entrapment crystallization has modified inclusion chemistry.

- Diverse textures traceable to shifts between fast and slow crystallization occur in single crystals. Thus, their compound morphologies and chemical zoning reflect growth at both high and low degrees of undercooling and supersaturation. This implies that rapid disequilibrium crystallization can account for some primary, inter- and intra-crystal textural and chemical heterogeneities in igneous quartz. Thus, our model of rapid quartz growth may impact the approach to analyzing and interpreting the quartz crystal stratigraphy.

- Abundant skeletal to dendritic and rarer granophyric quartz textures in the YTT and its effusive remnants are in accord with those produced experimentally at high degrees of undercooling and supersaturation (Swanson and Fenn, 1986; MacLellan and Trembath 1991). Because such morphologies require specific thermodynamic conditions, they provide a new foundation from which to investigate the thermochemical evolution and dynamics of Toba's pre- and post-caldera magma systems. Providing that skeletal quartz textures are non-unique to Toba rhyolites, they may serve as potentially unique tracers of dynamic processes and their rates over some spatial or temporal scale in silicic magma bodies.

- Skeletal to dendritic quartz textures in the Toba magma system record episodes of crystallization on short geologic timescales, possibly on the order of weeks to months. While such textures may echo the short timescales obtained from element diffusion modeling and melt inclusion shapes (e.g., Druitt et al. 2012; Gualda et al. 2012a; Allan et al. 2013; Pamukcu et al. 2015; Gualda and Sutton 2016), a record of both rapid and slow growth may suggest fast crystallization contributes latent heat needed to incubate large magma bodies for longer time periods (e.g., Huber et al. 2009). Moreover, the prevalence of these textures implies that dynamic processes can drive (at least portions of) voluminous systems to supersaturation while residing in the crust, which will have profound effects on their thermomechanical evolution and longevity.

ACKNOWLEDGMENTS

We are grateful to the EIU Geology Dept. for use of sample preparation equipment and supplies. Carrie Brugger-Schorr is thanked for her enthusiasm and encouragement during many insightful discussions on crystal growth. We thank the UCLA EPSS SEM lab and Rita

Economos for assistance with CL imaging. Caroline Bouvet de Maisonneuve is thanked for hosting OB at the Earth Observatory of Singapore (EOS). Help from Gareth Fabbro, Jason Herrin, and Dawn Ruth while using instrumentation at EOS is appreciated. Assistance was provided graciously by Rachel Beane during EBSD analyses; Guil Gualda and Lydia Harmon during X-ray CT analyses; and Marcel Guillong and Oscar Laurent during LA-ICP-MS analyses. This work benefited from conversations with Alfred Anderson, Kendra Lynn, Michael Ort, Amber Gullikson, Mary Reid, Jorge Vazquez, Jim Wittke, Fidel Costa, Guil Gualda, Olivier Bachmann, Josef Dufek, and Benoit Welsch. Suggestions from Benoit Welsch, Guil Gualda, and Eva Hartung on an earlier version of this manuscript are appreciated. Susanne Seitz and an anonymous reviewer are thanked for constructive reviews, and we are grateful to Christy Till for editorial handling. This work was supported by a National Science Foundation East Asia and Pacific Summer Institutes Award OISE-1514964 and Geological Society of America Graduate Student Research Grant to OB; EIU Council on Faculty Research Grant to CC; and National Science Foundation Grant EAR-1249821 to CD. Support for OB was also provided by Nanyang Technological University and the EOS.

REFERENCES CITED

Allan, A.S.R., Morgan, D.J., Wilson, C.J.N., and Millet, M.-A. (2013) From mush to eruption in centuries: assembly of the super-sized Oruanui magma body. Contributions to Mineralogy and Petrology, 166(1), 143–164.

Allmendinger, R.W., Cardozo, N.C., and Fisher, D. (2012) Structural Geology Algorithms: Vectors & Tensors, 289 p. Cambridge University Press, United Kingdom.

Anderson, A.T., Davis, A.M., and Lu, F. (2000) Evolution of Bishop Tuff rhyolitic magma based on melt and magnetite inclusions and zoned phenocrysts. Journal of Petrology, 41(3), 449–473.

Audétat, A., Garbe-Schönberg, D., Kronz, A., Pettke, T., Rusk, B., Donovan, J.J., and Lowers, H.A. (2015) Characterisation of a natural quartz crystal as a reference material for microanalytical determination of Ti, Al, Li, Fe, Mn, Ga and Ge. Geostandards and Geoanalytical Research, 39(2), 171–184.

Bachmann, O. (2010) The petrologic evolution and pre-eruptive conditions of the rhyolitic Kos Plateau Tuff (Aegean arc). Open Geosciences, 2(3), 270–305.

Bachmann, O., and Bergantz, G.W. (2004) On the origin of crystal-poor rhyolites: extracted from batholithic crystal mushes. Journal of Petrology, 45(8), 1565–1582.

Bachmann, O., Dungan, M.A., and Lipman, P.W. (2002) The Fish Canyon magma body, San Juan volcanic field, Colorado: rejuvenation and eruption of an upper-crustal batholith. Journal of Petrology, 43(8), 1469–1503.

Bacon, C.R. (1989) Crystallization of accessory phases in magmas by local saturation adjacent to phenocrysts. Geochimica et Cosmochimica Acta, 53(5), 1055–1066.

Baker, D.R., and Freda, C. (2001) Eutectic crystallization in the undercooled Orthoclase-Quartz-H_2O system. European Journal of Mineralogy, 13(3), 453–466.

Barbee, O.A. (2015) Origin of Toba's Post-Caldera Rhyolite Lava Domes and their Relation to the Youngest Toba Tuff Magma, 271 p. M.S. thesis, Northern Arizona University.

Beane, R., and Wiebe, R.A. (2012) Origin of quartz clusters in Vinalhaven granite and porphyry, coastal Maine. Contributions to Mineralogy and Petrology, 163(6), 1069–1082.

Befus, K.S., and Manga, M. (2019) Supereruption quartz crystals and the hollow reentrants. Geology, 47(8), 710–714.

Bégué, F., Deering, C., Gravley, D., Kennedy, B., Chambefort, I., Gualda, G., and Bachmann, O. (2014) Extraction, storage and eruption of multiple isolated magma batches in the paired Mamaku and Ohakuri eruption, Taupo Volcanic Zone, New Zealand. Journal of Petrology, 55(8), 1653–1684.

Berg, W. (1938) Crystal growth from solutions. Proceedings of the Royal Society of London: Mathematical, Physical and Engineering Sciences, A164, p. 79–95. The Royal Society.

Best, M.G., and Christiansen, E.H. (1997) Origin of broken phenocrysts in ash-flow tuffs. Geological Society of America Bulletin, 109(1), 63–73.

Bindeman, I.N., and Valley, J.W. (2002) Oxygen isotope study of the Long Valley magma system, California: isotope thermometry and convection in large silicic magma bodies. Contributions to Mineralogy and Petrology, 144(2), 185–205.

Blackerby, B. (1968) Convolute zoning of plagioclase phenocrysts in Miocene volcanics from the Western Santa Monica Mountains, California. American Mineralogist, 53, 954–962.

Bragg, W., and Gibbs, R. (1925) The structure of α and β quartz. Proceedings of the Royal Society of London. Series A, Containing Papers of a Mathematical and Physical Character, A109, p. 405–427. The Royal Society.

Brugger, C.R., and Hammer, J.E. (2015) Prevalence of growth twins among anhedral plagioclase microlites. American Mineralogist, 100(2–3), 385–395.

Budd, D.A., Troll, V.R., Deegan, F.M., Jolis, E.M., Smith, V.C., Whitehouse, M.J., Harris, C., Freda, C., Hilton, D.R., and Halldórsson, S.A. (2017) Magma reservoir dynamics at Toba caldera, Indonesia, recorded by oxygen isotope zoning in quartz. Scientific Reports, 7, 40624.

Buerger, M. (1945) The genesis of twin crystals. American Mineralogist, 30(7–8), 469–482.

Cahn, R. (1954) Twinned crystals. Advances in Physics, 3(12), 363–445.

Campbell, M.E., Hanson, J.B., Minarik, W.G., and Stix, J. (2009) Thermal History of the Bandelier Magmatic System: Evidence for Magmatic Injection and Recharge at 1.61 Ma as Revealed by Cathodoluminescence and Titanium Geothermometry. The Journal of Geology, 117(5), 469–485.

Cardozo, N., and Allmendinger, R.W. (2013) Spherical projections with OSXStereonet. Computers & Geosciences, 51, 193–205.

Carter, N.L., Officer, C.B., Chesner, C.A., and Rose, W.I. (1986) Dynamic deformation of volcanic ejecta from the Toba caldera: possible relevance to Cretaceous/Tertiary boundary phenomena. Geology, 14(5), 380–383.

Castro, A. (2001) Plagioclase morphologies in assimilation experiments. Implications for disequilibrium melting in the generation of granodiorite rocks. Mineralogy and Petrology, 71(1–2), 31–49.

Chesner, C.A. (1988) The Toba tuffs and caldera complex, Sumatra, Indonesia: Insights into magma bodies and eruptions, 428 p. Ph.D. thesis. Michigan Technological University.

Chesner, C.A. (1998) Petrogenesis of the Toba Tuffs, Sumatra, Indonesia. Journal of Petrology, 39(3), 397–438.

Chesner, C.A. (2012) The Toba Caldera Complex. Quaternary International, 258, 5–18.

Chesner, C.A., and Luhr, J.F. (2010) A melt inclusion study of the Toba Tuffs, Sumatra, Indonesia. Journal of Volcanology and Geothermal Research, 197(1–4), 259–278.

Chesner, C.A., and Rose, W.I. (1991) Stratigraphy of the Toba tuffs and the evolution of the Toba caldera complex, Sumatra, Indonesia. Bulletin of Volcanology, 53(5), 343–356.

Colin, A., Faure, F., and Burnard, P. (2012) Timescales of convection in magma chambers below the Mid-Atlantic ridge from melt inclusions investigations. Contributions to Mineralogy and Petrology, 164(4), 677–691.

Deer, W.A., Howie, R.A., and Zussman, J. (1963) Rock-forming Minerals: Vol. 4: Framework Silicates. 435 p. John Wiley & Sons, New York.

Donaldson, C., and Henderson, C. (1988) A new interpretation of round embayments in quartz crystals. Mineralogical Magazine, 52, 27–33.

Donaldson, C.H. (1976) An experimental investigation of olivine morphology. Contributions to Mineralogy and Petrology, 57(2), 187–213.

–. (1985) The rates of dissolution of olivine, plagioclase, and quartz in a basalt melt. Mineralogical Magazine, 49(354), 683–693.

Dowty, E. (1980a) Computing and drawing crystal shapes. American Mineralogist, 65(5–6), 465–471.

–. (1980b) Synneusis reconsidered. Contributions to Mineralogy and Petrology, 74(1), 75–84.

Dowty, E. (1987) SHAPE. Kingsport, TN: Shape Software. http://www.shapesoftware.com.

Drever, H., and Johnston, R. (1957) Crystal Growth of Forsteritic Olivine in Magmas and Melts. Transactions of the Royal Society of Edinburgh, 63(02), 289–315.

Drev, S., Rečnik, A., and Daneu, N. (2013) Twinning and epitaxial growth of taaffeite-type modulated structures in BeO-doped $MgAl_2O_4$. CrystEngComm, 15(14), 2640–2647.

Drugman, J. (1927) On β-quartz twins from some Cornish localities. Mineralogical Magazine, 21(119), 366–382.

Druitt, T.H., Costa, F., Deloule, E., Dungan, M., and Scaillet, B. (2012) Decadal to monthly timescales of magma transfer and reservoir growth at a caldera volcano. Nature, 482(7383), 77–80.

Faure, F., and Schiano, P. (2005) Experimental investigation of equilibration conditions during forsterite growth and melt inclusion formation. Earth and Planetary Science Letters, 236(3), 882–898.

Faure, F., Schiano, P., Trolliard, G., Nicollet, C., and Soulestin, B. (2007) Textural evolution of polyhedral olivine experiencing rapid cooling rates. Contributions to Mineralogy and Petrology, 153(4), 405–416.

Faure, F., Trolliard, G., Nicollet, C., and Montel, J.-M. (2003a) A developmental model of olivine morphology as a function of the cooling rate and the degree of undercooling. Contributions to Mineralogy and Petrology, 145(2), 251–263.

Faure, F., Trolliard, G., and Soulestin, B. (2003b) TEM investigation of forsterite dendrites. American Mineralogist, 88(8–9), 1241–1250.

Fenn, P.M. (1986) On the origin of graphic granite. American Mineralogist, 71(3–4), 325–330.

Flick, H. (1987) Geotektonische Verknüpfung von Plutonismus und Vulkanismus im südwestdeutschen Variscicum. Geologische Rundschau, 76, 699–707.

Friedel, G. (1933) Sur un noveau type de macles. Bulletin de la Société française de minéralogie et de cristallographie, 56, 262–274.

Frondel, C. (1945) Secondary Dauphiné twinning in quartz. American Mineralogist, 30, 447–461.

–. (1962) The System of Mineralogy of James Dwight Dana and Edward Salisbury Dana, Yale University, 1837–1892. Vol. 3. Silica Minerals. John Wiley & Sons, New York.

Gaubert, P. (1896) Sur la production artificielle de la macle des spinelles dans les cristaux d'azotate de plomb. Bulletin de la Société française de minéralogie et de cristallographie, 19, 431–434.

Gelman, S.E., Gutierrez, F.J., and Bachmann, O. (2013) On the longevity of large upper crustal silicic magma reservoirs. Geology, 41, 759–762.

Ghiorso, M.S., Carmichael, I.S.E., and Moret, L.K. (1979) Inverted high-temperature quartz. Contributions to Mineralogy and Petrology, 68(3), 307–323.

Girard, G., and Stix, J. (2009) Magma recharge and crystal mush rejuvenation associated with early post-collapse Upper Basin Member rhyolites, Yellowstone caldera, Wyoming. Journal of Petrology, 50, 2095–2125.

–. (2010) Rapid extraction of discrete magma batches from a large differentiating magma chamber: the Central Plateau Member rhyolites, Yellowstone Caldera, Wyoming. Contributions to Mineralogy and Petrology, 160(3), 441–465.

Götze, J., Plötze, M., and Habermann, D. (2001) Origin, spectral characteristics and practical applications of the cathodoluminescence (CL) of quartz–a review. Mineralogy and Petrology, 71(3–4), 225–250.

Graeter, K.A., Beane, R.J., Deering, C.D., Gravley, D., and Bachmann, O. (2015) Formation of rhyolite at the Okataina Volcanic Complex, New Zealand: New insights from analysis of quartz clusters in plutonic lithics. American Mineralogist, 100(8–9), 1778–1789.

Grimmer, H. (2006) Quartz aggregates revisited. Acta Crystallographica Section A, 62(2), 103–108.

Gualda, G.A., and Ghiorso, M.S. (2013) Low-pressure origin of high-silica rhyolites and granites. The Journal of Geology, 121(5), 537–545.

Gualda, G.A., Ghiorso, M.S., Lemons, R.V., and Carley, T.L. (2012a) Rhyolite-MELTS: a modified calibration of MELTS optimized for silica-rich, fluid-bearing magmatic systems. Journal of Petrology, 53(5), 875–890.

Gualda, G.A., Pamukcu, A.S., Ghiorso, M.S., Anderson, A.T., Jr., Sutton, S.R., and Rivers, M.L. (2012b) Timescales of quartz crystallization and the longevity of the Bishop giant magma body. PLoS One, 7(5), e37492.

Gualda, G.A., and Sutton, S.R. (2016) The Year Leading to a Supereruption. PLoS One, 11(7), e0159200.

Guillong, M., Meier, D.L., Allan, M.M., Heinrich, C.A., and Yardley, B.W. (2008) SILLS: A MATLAB-based program for the reduction of laser ablation ICP-MS data of homogeneous materials and inclusions. In P. Sylvester, Ed. Laser Ablation ICP-MS in the Earth Sciences: Current Practices and Outstanding Issues, p. 328–333, Vancouver.

Hammer, J.E. (2008) Experimental studies of the kinetics and energetics of magma crystallization. Reviews in Mineralogy and Geochemistry, 69(1), 9–59.

Hammer, J.E., and Rutherford, M.J. (2002) An experimental study of the kinetics of decompression-induced crystallization in silicic melt. Journal of Geophysical Research: Solid Earth, 107(B1), 1–23.

Hammer, J.E., Sharp, T.G., and Wessel, P. (2010) Heterogeneous nucleation and epitaxial crystal growth of magmatic minerals. Geology, 38(4), 367–370.

Harris, D.M., and Anderson Jr, A.T. (1984) Volatiles H_2O, CO_2, and Cl in a subduction related basalt. Contributions to Mineralogy and Petrology, 87(2), 120–128.

Hartman, P. (1956) On the morphology of growth twins. Zeitschrift für Kristallographie-Crystalline Materials, 107(1–6), 225–237.

Helz, R.T. (1987) Diverse olivine types in lava of the 1959 eruption of Kilauea volcano and their bearing on eruption dynamics. US Geological Survey Professional Paper, 1350, 691–722.

Hort, M. (1998) Abrupt change in magma liquidus temperature because of volatile loss or magma mixing: effects on nucleation, crystal growth and thermal history of the magma. Journal of Petrology, 39(5), 1063–1076.

Huang, R., and Audétat, A. (2012) The titanium-in-quartz (TitaniQ) thermobarometer: A critical examination and re-calibration. Geochimica et Cosmochimica Acta, 84, 75–89.

Jahns, R.H., and Burnham, C.W. (1969) Experimental studies of pegmatite genesis; l. A model for the derivation and crystallization of granitic pegmatites. Economic Geology, 64(8), 843–864.

Keith, M., and Tuttle, O. (1952) Significance of variation in the high-low inversion of quartz. American Journal of Science, Bowen vol., 203–280.

Kennedy, B., Wilcock, J., and Stix, J. (2012) Caldera resurgence during magma replenishment and rejuvenation at Valles and Lake City calderas. Bulletin of Volcanology, 74(8), 1833–1847.

Kirkpatrick, R.J. (1975) Crystal-growth from melt-review. American Mineralogist, 60(9–10), 798–814.

Kohut, E., and Nielsen, R.L. (2004) Melt inclusion formation mechanisms and compositional effects in high-An feldspar and high-Fo olivine in anhydrous mafic silicate liquids. Contributions to Mineralogy and Petrology, 147(6), 684–704.

Kozu, S. (1952) Japanese twins of quartz. American Journal of Science, Bowen vol., 281–292.

Krieger-Lassen, N. (1995) The relative precision of crystal orientations measured from electron backscattering patterns. Journal of Microscopy, 181, 72–81.

Kuo, L.-C., and Kirkpatrick, R.J. (1985) Kinetics of crystal dissolution in the system diopside-forsterite-silica. American Journal of Science, 285(1), 51–90.

Kuroda, T., Irisawa, T., and Ookawa, A. (1977) Growth of a polyhedral crystal from solution and its morphological stability. Journal of Crystal Growth, 42, 41–46.

Laemmlein, G. (1930) Korrosion und Regeneration der Porphyr-Quarze. Zeitschrift für Kristallographie-Crystalline Materials, 75(1), 109–127.

Le Châtelier, H. (1889) Sur la dilatation du quartz. Comptes Rendus, 108, 1046.

Lenart, A., Samardžija, Z., Godec, M., Mirtič, B., and Šturm, S. (2012) Twin-boundary formation in Japan-law twinned quartz crystals. European Journal of Mineralogy, 24(3), 509–517.

Libbrecht, K.G. (2005) The physics of snow crystals. Reports on Progress in Physics, 68(4), 855–895.

Liu, Y., Anderson, A.T., Wilson, C.J.N., Davis, A.M., and Steele, I.M. (2006) Mixing and differentiation in the Oruanui rhyolitic magma, Taupo, New Zealand: evidence from volatiles and trace elements in melt inclusions. Contributions to Mineralogy and Petrology, 151(1), 71–87.

Lofgren, G. (1971) Experimentally produced devitrification textures in natural rhyolitic glass. Geological Society of America Bulletin, 82(1), 111–124.

–. (1974) An experimental study of plagioclase crystal morphology; isothermal crystallization. American Journal of Science, 274(3), 243–273.

–. (1980) Experimental studies on the dynamic crystallization of silicate melts. In R. Hargraves, Ed., Physics of Magmatic Processes, p. 487–551. Princeton University Press, New Jersey.

London, D. (1992) The application of experimental petrology to the genesis and crystallization of granitic pegmatites. The Canadian Mineralogist, 30(3), 499–540.

London, D. (2009) The origin of primary textures in granitic pegmatites. The Canadian Mineralogist, 47(4), 697–724.

Lu, F., Anderson, A.T., and Davis, A.M. (1995) Diffusional gradients at the crystal/melt interface and their effect on the compositions of melt inclusions. The Journal of Geology, 103, 591–597.

MacLellan, H.E., and Trembath, L.T. (1991) The role of quartz crystallization in the development and preservation of igneous texture in granitic rocks; experimental evidence at 1 kbar. American Mineralogist, 76(7–8), 1291–1305.

Manley, C.R. (1996) Morphology and maturation of melt inclusions in quartz phenocrysts from the Badlands rhyolite lava flow, southwestern Idaho. American Mineralogist, 81(1–2), 158–168.

Manzini, M., Bouvier, A.-S., Baumgartner, L.P., Müntener, O., Rose-Koga, E.F., Schiano, P., Escrig, S., Meibom, A., and Shimizu, N. (2017) Weekly to monthly time scale of melt inclusion entrapment prior to eruption recorded by phosphorous distribution in olivine from mid-ocean ridges. Geology, 45(12), 1059-1062.

Matthews, N., Pyle, D., Smith, V., Wilson, C., Huber, C., and Van Hinsberg, V. (2012a) Quartz zoning and the pre-eruptive evolution of the ~340ka Whakamaru magma systems, New Zealand. Contributions to Mineralogy and Petrology, 163(1), 87–107.

Matthews, N.E., Huber, C., Pyle, D.M., and Smith, V.C. (2012b) Timescales of Magma Recharge and Reactivation of Large Silicic Systems from Ti Diffusion in Quartz. Journal of Petrology, 53(7), 1385–1416.

Milman-Barris, M.S., Beckett, J.R., Baker, M.B., Hofmann, A.E., Morgan, Z., Crowley, M.R., Vielzeuf, D., and Stolper, E. (2008) Zoning of phosphorus in igneous olivine. Contributions to Mineralogy and Petrology, 155(6), 739–765.

Molloy, C., Shane, P., and Nairn, I. (2008) Pre-eruption thermal rejuvenation and stirring of a partly crystalline rhyolite pluton revealed by the Earthquake Flat Pyroclastics deposits, New Zealand. Journal of the Geological Society, 165(1), 435–447.

Momma, K., Nagase, T., Kuribayashi, T., and Kudoh, Y. (2015) Growth history and textures of quartz twinned in accordance with the Japan law. European Journal of Mineralogy, 27(1), 71–80.

Müller, A., Kronz, A., and Breiter, K. (2002) Trace elements and growth pattern in quartz: a fingerprint of the evolution of the subvolcanic Podlesí Granite System (Krušné Hory, Czech Republic). Bulletin of Czech Geological Survey, 77, 135–145.

Müller, A., Seltmann, R., and Behr, H.-J. (2000) Application of cathodoluminescence to magmatic quartz in a tin granite–case study from the Schellerhau Granite Complex, Eastern Erzgebirge, Germany. Mineralium Deposita, 35(2–3), 169–189.

Müller, A., van den Kerkhof, A.M., Behr, H.-J., Kronz, A., and Koch-Müller, M. (2009) The evolution of late-Hercynian granites and rhyolites documented by quartz – a review. Earth and Environmental Science Transactions of the Royal Society of Edinburgh, 100(1–2), 185–204.

Myers, M.L., Wallace, P.J., Wilson, C.J., Morter, B.K., and Swallow, E.J. (2016) Prolonged ascent and episodic venting of discrete magma batches at the onset of the Huckleberry Ridge supereruption, Yellowstone. Earth and Planetary Science Letters, 451, 285–297.

Nabelek, P.I., Whittington, A.G., and Sirbescu, M.-L.C. (2010) The role of H_2O in rapid emplacement and crystallization of granite pegmatites: resolving the paradox of large crystals in highly undercooled melts. Contributions to Mineralogy and Petrology, 160(3), 313–325.

Nespolo, M., and Ferraris, G. (2004) The oriented attachment mechanism in the formation of twins–a survey. European Journal of Mineralogy, 16(3), 401–406.

Pamukcu, A.S., Ghiorso, M.S., and Gualda, G.A. (2016) High-Ti, bright-CL rims in volcanic quartz: a result of very rapid growth. Contributions to Mineralogy and Petrology, 171(12), 105.

Pamukcu, A.S., and Gualda, G.A. (2010) Quantitative 3D petrography using X-ray tomography 2: Combining information at various resolutions. Geosphere, 6(6), 775–781.

Pamukcu, A.S., Gualda, G.A., Bégué, F., and Gravley, D.M. (2015) Melt inclusion shapes: Timekeepers of short-lived giant magma bodies. Geology, 43(11), 947–950.

Pamukcu, A.S., Gualda, G.A.R., and Anderson, A.T. (2012) Crystallization Stages of the Bishop Tuff Magma Body Recorded in Crystal Textures in Pumice Clasts. Journal of Petrology, 53(3), 589–609.

Peppard, B.T., Steele, I.M., Davis, A.M., Wallace, P.J., and Anderson, A.T. (2001) Zoned quartz phenocrysts from the rhyolitic Bishop Tuff. American Mineralogist, 86(9), 1034–1052.

Prior, D.J., Boyle, A.P., Brenker, F., Cheadle, M.C., Day, A., Lopez, G., Peruzzo, L., Potts, G.J., Reddy, S., and Spiess, R. (1999) The application of electron backscatter diffraction and orientation contrast imaging in the SEM to textural problems in rocks. American Mineralogist, 84(11–12), 1741–1759.

Reid, M.R., Coath, C.D., Harrison, T.M., and McKeegan, K.D. (1997) Prolonged residence times for the youngest rhyolites associated with Long Valley Caldera; ^{230}Th-^{238}U ion microprobe dating of young zircons. Earth and Planetary Science Letters, 150, 27–39.

Rivers, M.L., Sutton, S.R., and Eng, P.J. (1999) Geoscience applications of X-ray computed microtomography. SPIE's International Symposium on Optical Science, Engineering, and Instrumentation, p. 78–86. International Society for Optics and Photonics.

Roedder, E. (1979) Origin and significance of magmatic inclusions. Bulletin de Minéralogie, 102, 487–510.

Schaskolsky, M., and Schubnikow, A. (1933) Über die künstliche Herstellung gesetzmässiger Kristallverwachsungen des Kalialauns. Zeitschrift für Kristallographie-Crystalline Materials, 85(1–6), 1–16.

Schwindinger, K.R. (1999) Particle dynamics and aggregation of crystals in a magma chamber with application to Kilauea Iki olivines. Journal of Volcanology and Geothermal Research, 88(4), 209–238.

Schwindinger, K.R., and Anderson Jr, A.T. (1989) Synneusis of Kilauea Iki olivines. Contributions to Mineralogy and Petrology, 103(2), 187–198.

Seitz, S., Putlitz, B., Baumgartner, L.P., Escrig, S., Meibom, A., and Bouvier, A.-S. (2015) Short magmatic residence times of quartz phenocrysts in Patagonian rhyolites associated with Gondwana breakup. Geology, 44(1), 67–70.

Seitz S., Putlitz, B., Baumgartner, L.P., and Bouvier, A.-S. (2018a) The role of crustal melting in the formation of rhyolites: Constraints from SIMS oxygen isotope data (Chon Aike Province, Patagonia, Argentina). American Mineralogist, 103, 2011–1027.

Seitz, S., Putlitz, B., Baumgartner, L., Meibom, A., Escrig, S., and Bouvier, A-.S. (2018b) A NanoSIMS Investigation on Timescales Recorded in Volcanic Quartz From the Silicic Chon Aike Province (Patagonia). Frontiers in Earth Science, 6:95, doi: 10.3389/feart.2018.00095

Smith, V., Shane, P., and Nairn, I. (2010) Insights into silicic melt generation using plagioclase, quartz and melt inclusions from the caldera-forming Rotoiti eruption, Taupo volcanic zone, New Zealand. Contributions to Mineralogy and Petrology, 160(6), 951–971.

Steno, N. (1669) De Solido Intra Sodium Naturaliter Contento Dissertations Prodomus, Florence. English translation by J. G. Winter. The Prodomus of Nicolaus Steno’s Dissertation Concerning a Solid Body Enclosed by Process of Nature within a Solid. 1968, Hafner, New York.

Sunagawa, I. (1981) Characteristics of crystal-growth in nature as seen from the morphology of mineral crystals. Bulletin de Minéralogie, 104(2–3), 81–87.

Sunagawa, I. (2005) Crystals: growth, morphology, & perfection. Cambridge University Press, United Kingdom.

Sunagawa, I., Imai, H., Takada, M., and Hoshino, Y. (2004) Morphogenesis of quartz crystals twinned after Japan Law. European Journal of Mineralogy, 16(1), 91–97.

Sunagawa, I., Takahashi, J., Aonuma, K., and Takahashi, M. (1979) Growth of quartz crystals twinned after Japan law. Physics and Chemistry of Minerals, 5(1), 53–63.

Swanson, S. (1977) Relation of nucleation and crystal-growth rate to the development of granitic textures. American Mineralogist, 62(9–10), 966–978.

Swanson, S.E., and Fenn, P.M. (1986) Quartz crystallization in igneous rocks. American Mineralogist, 71(3–4), 331–342.

Thomas, J.B., Bruce Watson, E., Spear, F.S., Shemella, P.T., Nayak, S.K., and Lanzirotti, A. (2010) TitaniQ under pressure: the effect of pressure and temperature on the solubility of Ti in quartz. Contributions to Mineralogy and Petrology, 160(5), 743–759.

Troch, J., Ellis, B.S., Mark, D.F., Bindeman, I.N., Kent, A.J., Guillong, M., and Bachmann, O. (2017) Rhyolite generation prior to a Yellowstone supereruption: insights from the Island Park–Mount Jackson Rhyolite series. Journal of Petrology, 58(1), 29–52.

Tsuchiyama, A. (1986) Experimental study of olivine-melt reaction and its petrological implications. Journal of Volcanology and Geothermal Research, 29(1–4), 245–264.

Vance, J.A. (1969) On synneusis. Contributions to Mineralogy and Petrology, 24(1), 7–29.

Vogt, J.H.L. (1921) The physical chemistry of the crystallization and magmatic differentiation of igneous rocks. The Journal of Geology, 29(4), 318–350.

Wallace, P.J., Anderson, A.T., and Davis, A.M. (1999) Gradients in H_2O, CO_2, and exsolved gas in a large-volume silicic magma system: Interpreting the record preserved in melt inclusions from the Bishop Tuff. Journal of Geophysical Research: Solid Earth, 104(B9), 20097–20122.

Wark, D.A., Hildreth, W., Spear, F.S., Cherniak, D.J., and Watson, E.B. (2007) Pre-eruption recharge of the Bishop magma system. Geology, 35(3), 235–238.

Wark, D.A., and Spear, F.S. (2005) Ti in quartz: Cathodoluminescence and thermometry. Geochimica et Cosmochimica Acta, 69, 592.

Wark, D.A., and Watson, E.B. (2006) TitaniQ: a titanium-in-quartz geothermometer. Contributions to Mineralogy and Petrology, 152(6), 743–754.

Watanabe, J. (1974) Quartz fabrics in Alteration Zones Surrounding the Hitachi Copper Deposits, Abukuma Plateau, Japan. Journal of the Faculty of Science, Hokkaido University. Series 4, Geology and mineralogy, 16(2–3), 145–192.

Welsch, B., Faure, F., Bachelery, P., and Famin, V. (2009) Microcrysts Record Transient Convection at Piton de la Fournaise Volcano (La Reunion Hotspot). Journal of Petrology, 50(12), 2287–2305.

Welsch, B., Faure, F., Famin, V., Baronnet, A., and Bachelery, P. (2013) Dendritic Crystallization: A Single Process for all the Textures of Olivine in Basalts? Journal of Petrology, 54(3), 539–574.

Welsch, B., Hammer, J., Baronnet, A., Jacob, S., Hellebrand, E., and Sinton, J. (2016) Clinopyroxene in postshield Haleakala ankaramite: 2. Texture, compositional zoning and supersaturation in the magma. Contributions to Mineralogy and Petrology, 171(1), 1–19.

Welsch, B., Hammer, J., and Hellebrand, E. (2014) Phosphorus zoning reveals dendritic architecture of olivine. Geology, 42(10), 867–870.

Wilcock, J., Goff, F., Minarik, W.G., and Stix, J. (2013) Magmatic Recharge during the Formation and Resurgence of the Valles Caldera, New Mexico, USA: Evidence from Quartz Compositional Zoning and Geothermometry. Journal of Petrology, 54(4), 635–664.

Xu, H., Zhang, J., Yu, T., Rivers, M., Wang, Y., and Zhao, S. (2014) Crystallographic evidence for simultaneous growth in graphic granite. Gondwana Research, 27(4), 1550–1559.

Zhao, S.-R., Xu, H.-J., Wang, Q.-Y., and Yang, K.-G. (2013) Electron backscatter diffraction study of twins and intergrowths among quartz crystals in granite. Journal of Applied Crystallography, 46(5), 1414–1424.

FIGURE CAPTIONS

Figure 1. Sample locations shown on a DEM of Toba caldera (Sumatra, Indonesia). Rhyolite dome exposures outside the study area (inset) were discovered in 2015 by Chesner et al. (submitted).

Figure 2. Examples of thick serial sections of YTT pumice (sample T-13). The full sequence represents eight successive cuts parallel to the pumice stretch direction (slices 6–8 are in **Fig. 1 of App.**[3]). Individual serial sections in this study are ~0.15–0.5 mm thick and separated by a ~0.9 mm kerf width. A pink background shows transparent crystals of quartz (Qz; shaded red in Slice 3; some fractures are stained), plagioclase (Pl), and sanidine (Sa). Like quartz, the feldspars can reach megacrystic sizes and form clusters. Plagioclase commonly exhibits abundant glass inclusions and is shattered. Sanidine is often elongate to tabular, but low in abundance and relatively small in this sample.

Figure 3. Mineralogical data for quartz. Polymorphs of β- and α-quartz represent the hexagonal crystal system, but possess different lattice symmetries. Beta-quartz is stable above 573°C at 1 atm and contains hexagonal 6-fold lattice symmetry (*622 class; $P6_422$ or $P6_222$ space group*), whereas α-quartz is stable below 573°C at 1 atm and contains rhombohedral (trigonal) 3-fold symmetry (*32 class; $P3_221$ or $P3_121$ space group*) (Le Châtelier 1889; Bragg and Gibbs 1925; Keith and Tuttle 1952; Deer et al. 1963). Crystal forms and interfacial angles were calculated using SHAPE v7.4 software (Dowty 1980a, 1987) for β-quartz and α-quartz in their respective

point symmetries (*622* and *321*) and unit-cell parameters (a=5.01, c=5.47 Å and a=4.913, c=5.405 Å; Deer et al. 1963; Ghiorso et al. 1979), which correlate to axial ratios of a:c=1:1.093 and a:c=1:1.1 (Frondel 1962); however, primary β-quartz structurally possesses those of α-quartz at room temperature. Orientations of *a* and *c* crystallographic axes are equal in both polymorphs, but $\{10\bar{1}1\}$ and $\{01\bar{1}1\}$ lattice planes change to positive *r* and negative *z* rhombohedra in α-quartz. Interfacial angles of polymorphs are red=β, blue=α, and purple=mutual. Interfacial angles are constant regardless of crystal asymmetry (i.e. law of constancy of interfacial angles, Steno 1669), but cross-sections oblique to *a* and *c* axes can simulate apparent angles, especially between pyramidal or rhombohedral faces. The area of each crystal form or face (dictated by growth rate in nature) was controlled by changing their central distances. Angular relationships and morphology variations for twin laws are drawn after Sunagawa (2004) and Frondel (1945, 1962). Verespatak Law (β-quartz) is traditionally Japan Law for primary α-quartz; and the Esterel Law (β-quartz) is equivalent to Reichenstein-Grieserntal Law for primary α-quartz. Although twin law names are implicative of polymorph, we refer to just one pair for consistency. Previous literature intermixes the names as a note of caution (i.e. Beane and Wiebe 2012; Graeter et al. 2015). Twin *r* and *z* rhombohedra are depicted due to observed asymmetry, but are interchangeable with *p* faces of the dipyramidal form. Black pins indicate the angular relationships between poles to faces that distinguish the contact twins.

Figure 4. Representative habits and morphologies of Toba quartz. Images were taken with a stereomicroscope (a, b, f–i), SEM (c, d, j–m), and petrographic microscope (e). Scale bars are 100 μm. Crystal replicas were drawn using SHAPE v7.4 software (Dowty 1980a, 1987) to emphasize face shape and size. Crystals (a–c, e, i, l, m) are polyhedral, whereas those in (d, f–h,

j, k) are skeletal or contain remnant hopper cavities. Some crystals are fractured. **(a)** Crystal with extended diagonal and apical edges (out of focus) between opposing rhombohedral faces (sample T-12). **(b)** Crystal exhibiting extended diagonal edges between opposing rhombohedral and prism faces due to asymmetric rhombohedral faces (T-20). **(c–d)** SE images of crystals containing large prism faces and unequal rhombohedral faces (TT-10). Remnants of two hollow prism faces in crystal (d) are indicated by an oval depression (front) and subtle terraces (front and left). Dense glass is shaded orange. **(e)** Cross-section of an in situ asymmetric crystal encased in vesicular matrix glass (plane-polarized light). Interfacial angles verify the prism form (T-5B). **(f)** Skeletal (hopper) crystal showing many sharp terraces (growth steps) inside a hollow rhombohedral face (T-12). Diagonal edge orientations are preserved in the terrace pattern (i.e. *r* and *z* face inequality persisted throughout growth). **(g)** Two similar skeletal-polyhedral crystals showing hollow prism faces and polyhedral rhombohedral faces (T-12). **(h)** Hopper crystal showing hollow prism faces with traces of curved terraces. The funnel-shaped cavity overlies part of its embayment (T-13). **(i)** Enclosed remnant hopper cavities (MIs) that mimic shapes of overlying crystal faces (T-5B). **(j)** Two views of a hollow prism face that contains both terraces and smooth surfaces. The crystal exhibits a compound morphology (i.e. skeletal-anhedral-polyhedral) (T-5B). **(k)** Cross-section of a broken crystal similar to (g) and (h). The embayment opening spans the width of the prism face depression (i.e. remnant hollow face) (T-20). **(l–m)** Highly asymmetric crystals. Crystal in (l) shows the imprint of a lost subcrystal (shaded teal). Imprint edges parallel crystal edges (T-5B).

Figure 5. Quartz textures in X-ray tomograms. Air and matrix glass have been removed. Separate crystals or minerals may surround quartz of interest, but they are not in contact. Purple

DOI: https://doi.org/10.2138/am-2020-6947

arrows indicate re-entrant edges; black arrows indicate magnetite inclusions (white). **(a)** Snapshots of two parallel, interpenetrated, dipyramidal units in clockwise rotation. Views 4b and 5 show a hollow face (hopper cavity) in cross-section and 3D, respectively. Sectioned quartz clusters that may appear similar to this one in 3D can be found in **Fig. 10a, c,** and **g**, for example. **(b)** Successive slices that intersect MIs and embayments hosting magnetite (Mag) inclusions. The shattered megacryst (ø ~10 mm) is delineated by orange dashed lines. Crystal faces outside chosen section planes are masked in red (prism, *m*) and orange (rhombohedral, *r* or *z*). Insets represent enlargements of magnetite crystals attached to embayment walls (orange solid lines).

Figure 6. Quartz textures in thin and thick sections. Images (b–f, h–k) have map coordinates in 3” x 2” sections of **Fig. 2 of App.**[3]. **(a)** Burst, faceted megacryst containing embayments lying in different orientations (sample T-57). **(b)** Skeletal macrocryst with embayments or cavities. Faceted MIs occur beneath crystal faces. Protuberances are faceted and extend from edge or corner locations (T-5B). **(c)** Mesocryst exhibiting hollow faces of the prism form (T-5B). Small MIs occur beneath rhombohedral faces. **(d)** Macrocryst (left) and mesocryst (lower right) with embayments or MIs at centers of crystals faces (TT-2). The macrocryst displays (in 2D) a triangular-shaped cavity with overhanging skeletal appendages (opposing terraces). **(e)** Optically continuous mesocryst (near extinction) showing redundant faces, asymmetry, and skeletal-polyhedral morphology (TT-2). **(f)** Burst megacryst with repeated faces, embayments, and misoriented regions separated by fractures (T-12). **(g)** Macrocryst with a misoriented region delineated by a subgrain boundary (TT-4). Embayments/triangular-shaped voids also bound misoriented regions. **(h)** V-shaped macrocryst showing two regions with different interference colors and extinctions (T-12). **(i)** Macrocryst with three regions (separated by fractures) of

different interference colors and extinctions (T-13). **(j)** Optically discontinuous microcryst and mesocryst pairs, each a mirror image or inversion about a planar contact (arrows) (T-5B). **(k)** Serial sequence showing blocky-progressive extinction and repeated faces of different crystal forms (T-12). Irregular dislocation planes are concentrated nearer the repetitive external faces. **(l)** Plane-polarized light (PPL) + reflected light image showing concentrated MIs and a magnetite inclusion at the center of a cluster (see corresponding CL image in **Fig. 5f of App.**[3]). The inclusion lies at the head of a deep embayment. **(m)** PPL image showing magnetite and apatite inclusions in CL-imaged quartz of **Fig. 10c**. Two magnetite octahedrons are attached in parallel.

Figure 7. Sketch summarizing crystal zoning and textures revealed by CL imaging. Sizes of textural features *4* through *12* are described in the text. The relative scaling of some drawn features is arbitrary.

Figure 8. Crystallography of quartz clusters determined through EBSD. Clusters in CL images are displayed next to Euler orientation maps and corresponding pole figures. Data points (pixels) are represented by Euler colors that indicate different crystallographic orientations and are plotted in upper hemisphere stereographic projections. Dashed white lines delineate prominent crystal fractures bordered by Dauphiné twins (*D*). Crystal shape and CL zone configurations were combined with EBSD data to model simplistic 3D solutions of clusters in SHAPE v7.4 software (see *Methods*; Dowty 1980a, 1987). Modeled crystal margins may not replicate true margins due to complex asymmetric habits. Arborescent zones (described in *Zonings*, **Fig. 10–13**) are delineated in CL images. **(a)** Five nearly identical parallel units disguised as a single crystal. Each core has brighter oscillating CL zones surrounded by much darker CL zones. *Units*

1 and *2* are most resembled in *Slice 1* because equivalent levels of *Units 3–5* lie outside the section plane. A 3D reconstruction requires remarkably organized interpenetrations of elongate prismatic units to replicate CL zoning in both *Slices 1* and *2* [sample T-12 (C11, 10)]. **(b)** Units in Verespatak or parallel relation. Unit cores show brighter oscillating CL zones encased in darker CL zones. A 3D reconstruction requires trigonal symmetry and asymmetric habit. The re-entrant edge (*RE*) is also characteristic of growth twins (Hartman 1956; Sunagawa et al. 2004) [sample T-20 (2.9)]. **(c)** Repeated Esterel twinning on *Unit 3* creates a 113° angle between *Units 1* and *2*. The two sandwiching units are thus, by symmetry, related. Because equivalent unit levels are not exposed, unit size and zoning patterns appear somewhat dissimilar. Note the configuration of faint brighter CL zones at the core of *Unit 1* (see *Zonings*, **Fig. 10**) [sample T-13 (H6)]. **(d)** Repeated Esterel twinning on parallel *Units 2* and *3* creates a 113° angle between *Units 1* and *4*. Like (c), a 3D model requires the prism form to replicate unit shapes and CL zoning. EBSD map and Dauphiné twins not shown (see **App.**[2]) [sample SF-3 (3.1)]. **(e)** Megacrystic cluster comprising eight units. Larger units do not differ significantly in zoning pattern, whereas *Units 3–6* are smaller, located in the megacryst exterior, and can differ in zoning pattern. All units are in parallel except *Unit 5*, a Verespatak twin. Asymmetric Verespatak (Japan) twin development (i.e. a small twin astride a larger one) is common in nature (Drugman 1927). Note *Unit 5*'s three-fold distribution of Dauphiné twins and its layers of arborescent CL zones (see *Zonings*, **Fig. 10**) [sample T-12 (B)].

Figure 9. Sketches of arborescent CL zones in Toba quartz.

Figure 10. Arborescent zones exposed in CL images of in situ quartz. Arborescent zones can be subtle and may be better observed by magnifying the digital version of the figure. Insets represent enhanced enlargements. **(a)** Ruptured pair of parallel polyhedral units (sample T-20). The section plane lies in the center of *Unit 1*'s core and not in *Unit 2*'s, hence their similar CL characteristics, but pattern disparity. The classic construction of arborescent zones is displayed by *Unit 1* (i.e. branched limbs propagating from vertices of a polyhedral zone of similar CL, all underlain by periodic oscillations). Note locations of exposed MIs/halos and that some branches appear blurred. Orange arrows indicate apatite (Ap) inclusions. **(b)** Polyhedral crystal displaying feathery arms between MIs/embayments (TT-10). **(c)** Two parallel units that appear as a single crystal and share a mutual limb zone (pattern highlighted white; TT-6). Separate magnetite inclusions lie deeper within heads of two embayments (shown in **Fig. 6m**). **(d)** Polyhedral crystal with CL branches appearing as curvilinear lobes. A teardrop-shape MI is central to the core (SF-1). **(e)** A section plane exposing two generations of arborescent zones in one twin, but not in the other (SF-3). **(f)** Two generations of arborescent zones appear subtle at low-magnification (TT-10). This section plane does not expose equivalent levels of each unit. Branches in *Unit 2* appear disconnected (i.e. unattached to a primary limb). **(g)** Interpenetration of parallel *Units 1* and *2* and their size decrease in the propagation direction of their mutual limb are important (SF-3). *Units 3* and *4* are offset by 1–2°.

Figure 10 continued. (h) Ruptured, complex cluster (T-13). Arborescent zones in different units do not all appear in one section plane. Note the zoning pattern similarities and mutual orientations of face directions among zones in some unit cores (especially parallel *Units 2* and *3*). **(i)** Cluster disguised as a single crystal, which displays seam MIs, suture boundaries, and CL zone adaptations to these features (TT-2). This section plane does not expose equivalent levels of each unit, but shows their mutual exterior. **(j)** High magnification of small-scale overgrowths that appear as 'wavy' zones within crystal mantles (TT-2). **(k)** Three units disguised as a single crystal (T-20). Note that the dark CL area surrounding oscillations in *Unit 3* matches the dark CL area around branches in *Unit 2*. **(l)** Arborescent zones nested in a bright CL region with MIs/embayments, which were partially infilled by darker CL quartz (SF-1). Inclusions are also associated with the wavy, jagged margin of the bright zone. **(m)** Ruptured megacrystic cluster (T-57). Tiny MIs (black dots) in the core of *Unit 4* are consistent with the presence of arborescent zones, which display diffuse boundaries with their dark CL encasement.

Figure 11. Titanium and aluminum concentrations determined by LA-ICP-MS in arborescent and surrounding CL zones. A full set of trace element data for these and additional crystals can be found in **Table 5 of App.**[1]. Magenta symbols for laser-ablation pits are to scale (~29 µm). Pits with green-blue symbols represent crystal mantle (generic CL zoning) or rim analyses spatially unrelated to arborescent zones and their encasing zones. Analytical error is 1σ. Legend is the same as in **Fig. 10**. **(a)** Arborescent zones containing higher amounts of Ti (top values) and Al (bottom values) relative to the dark CL polyhedral interior zone (sample T-5B). Orange arrows indicate apatite (Ap) inclusions. **(b)** Branching tips propagate from vertices of a bright CL polyhedral to wavy 'root' zone, which has some of the highest Ti, Al concentrations identified for these features (T-20). The greater apparent thickness of the 'root' zone in *Unit 2* is likely an effect of a high-angle section plane relative to its planar surface. *Units 1* and *2* are non-parallel (possibly twins). **(c)** Group of six formerly intact units (T-13). *Units 1*, *2*, *3*, *5*, and *7* are parallel; *Units 6* and *8* are parallel, *Unit 4* is not parallel to any other unit. In this section, most units

possess similar core characteristics (i.e. thin brighter CL oscillating zones ± arborescent tips encased by dark CL quartz), but *Units 1* and *2* are most resembled, showing equivalent face zones and arborescent tips in mutual orientations (remainder of *Unit 2* is not exposed). *Slice 2* is in **Fig. 5 of App.**[3] and does not show these textures. Plotted laser-ablation transects show variations in Ti and Al in *Units 1*, *3*, and *4*. Transect data are plotted from left to right across a unit and are discontinuous (green-blue pit symbols have been enlarged in top image). At unit cores, the magenta color spectrum is defined by Ti variations, which have been roughly categorized (shaded boxes) into az = brighter CL arborescent zones and associated oscillations; de = dark CL encasement; az:de > 1; and az:de < 1. Titanium values intermediate between the highest and lowest values likely represent different proportions of az:de unavoidably sampled using laser-ablation.

Figure 12. Interpretation of arborescent CL zones using a 3D model of hopper crystals of quartz. Sectioning older prismatic and dipyramidal hopper crystals containing terraced cavity walls generates zoning patterns like those observed in **Figs. 8–11** (except for **8e, 9d, f, 10b, 11b** – see **Fig. 13**; cf. Welsch et al. 2013, 2014). All model faces of forms p or $r\{10\bar{1}1\}$, $z\{01\bar{1}1\}$, and $m\{10\bar{1}0\}$ are initially polyhedral (blue and dark gray), become hollow (red), and subsequently redevelop (dark and light grays). Zoning in lower index section planes of the model are shown, although obtained sections can be variations of these. Model arborescent zones are simplified, as observed disparities in apparent branch thickness and length (tapered arrows vs. thin and feathery) may be related to both growth phenomena and section orientation (compare **Fig. 9** sketches). Branch thickening as a possible effect of terrace intersections at high-angles is depicted in sections A2—plane $(1\bar{2}10)$ and C—plane $(1\bar{2}12)$. Successive branch lengthening is

most-likely growth-related and is only depicted in sections A1—plane $(1\bar{2}10)$ and D—plane $(1\bar{2}10)$ for example. Diffuseness of branch boundaries is not illustrated in the model, but may be an effect of section orientation or trace element diffusion. Sections A1 and D—plane $(1\bar{2}10)$ show feathery zoning similar to **Fig. 10a, i** and **Fig. 10c, m**, respectively, by intersecting terraced hopper cavities, corners and edges that propagate from a polyhedral foundation (also **Fig. 5g of App.**[3]). Section A2—plane $(1\bar{2}10)$ shows zoning similar to **Fig. 11a** by intersecting only terraces and edges and not cavities along the prism direction. Section B—plane (0001) displays symmetrically distributed feathery zoning similar to **Fig. 10f, l**. Oblique section C—plane $(1\bar{2}12)$ exhibits many corners/edges and the continuations of terraces between them (connections of branches) similar to **Fig. 10d, h** and **Fig. 5b, c of App.**[3]. Sections E1 and E2—plane $(1\bar{1}01)$ parallel the same face direction, but E1 generates pseudo-oscillatory zoning similar to **Fig. 10k** by clipping only terraces of the hollow $(1\bar{1}01)$ face; whereas, E2 displays feathery zoning by intersecting cavities, corners, and edges. Section F—plane (0001) generates hexagonal pseudo-oscillatory zoning like that in *Unit 3* of **Fig. 11c** by intersecting only terraces, edges and not cavities. Crystal forms and cross-sections were drawn using SHAPE v7.4 software (Dowty 1980a, 1987).

Figure 13. Interpretation of arborescent CL zones using a 3D model of dendrites. Sectioning older dendritic overgrowths generates zoning patterns observed in **Figs. 8e, 9d, f, 10b, 11b**, and **Fig. 5e of App.**[3]. All model faces of forms *p* or $r\{10\bar{1}1\}$ and $z\{01\bar{1}1\}$ are initially polyhedral (blue and dark gray), become hollow (red), and subsequently redevelop (dark and light grays). Dendrite tips may propagate first from crystal corners or in directions of crystallographic axes (see Swanson and Fenn 1986). Arborescent zones are described in the same way as in **Fig. 12**,

but here, limbs and branches intersecting at right angles or forming exterior angles (i.e. branches are inclined away from the crystal center and do not parallel subjacent face directions) are true primary and secondary dendrite branches. Section A—plane (0001) exhibits 'snowflake' arms by intersecting dendrite tips that propagate from vertices of a polyhedral foundation.

Figure 14. Sketch of boundary layer uptake and defect increase to explain higher Ti concentrations and CL intensities of arborescent zones (adapted from Welsch et al. 2013). Scale is arbitrary. **(a)** The quartz crystal surface is growing slowly at near-equilibrium conditions, and is not consuming a boundary layer contaminated with elements that are incompatible in quartz. **(b)** An increase in quartz growth rate during rapid skeletal to dendritic crystallization leads to a build-up of slow-diffusing incompatible elements at the crystal-melt contact. Continued accumulation of rejected elements at the rapidly advancing crystal surface leads to their consumption; elements incorporated into the lattice are dominantly ones most compatible with quartz (Ti, ± Al) (see **Table 5 of App.**[1]; Huang and Audétat 2012). The rapid crystallization also likely induces intrinsic point defects in the lattice structure (Götze et al. 2001). Both extrinsic (Ti) and intrinsic defects may contribute to the overall higher CL intensity of the rapidly crystallized layer. **(c)** Liquid differentiation and latent heat build-up along the crystal surface leads to a decrease in crystal growth rate. Slow growing infill buries the skeletal to dendritic layers, which are preserved by enrichments in impurity elements and lattice defects.

Figure 15. Evolution of crystal morphology common to early stages of quartz growth (compare with Welsch et al. 2013). Quartz crystallizes rapidly following nucleation, and quickly transitions from a polyhedral to skeletal (hopper) morphology under a high degree of

DOI: https://doi.org/10.2138/am-2020-6947

undercooling (a similar transition is also common to branching snowflakes that evolve from hexagonal plates; Libbrecht 2005). The propagation of crystal corners and edges may transition to dendritic crystallization that manifests as replicated overgrowths, or buds, on the initial crystal (see *Dendritic buds and growth twins*). The crystal growth rate subsequently decays and quartz begins to infill its hollow crystal faces. Slower infilling leads to melt inclusion entrapment and embayment formation as quartz develops faces above its hopper cavities. Preferential growth (infilling) may occur along pyramidal $p\{10\bar{1}1\}$ or rhombohedral $r\{10\bar{1}1\}$ and $z\{01\bar{1}1\}$ faces, while the prism $m\{10\bar{1}0\}$ faces lag behind (e.g., **Fig. 4d, g, h, j, k**). This is consistent with the relative normal growth rates of these forms, $R_m<R_r<R_z<<R_{0001}$ (Sunagawa 2005 and references therein), from which we predict hollow *r* and *z* faces will infill quicker than hollow *m* faces due to the anisotropy in growth rates and tendency for R_m to be relatively low. Development of the prism implies a higher ratio of $R_{r,z}$:R_m, and likely formed in response to the initial rapid growth stage, consistent with relic skeletal to dendritic core morphologies (**Figs. 12** and **13**).

Figure 16. (a) Interpretations of CL halos around melt pockets (inclusions, embayments). See text for details. Crystals illustrated are from **Fig. 10a, c,** and **d**. **(b)** Protuberance size and shape vs. quartz crystal size. Sketched crystal margins and prominent zone adaptations correspond to those in CL-images of **Fig. 4 of Appendix**[3]. Protuberances are indicated by green arrows. We hypothesize that larger crystals may have (1) had morphologies similar to smaller crystals earlier in time, and subsequently infilled, or (2) they developed skeletal protuberances and infilled after having already obtained a larger crystal size.

Figure 17. Quartz morphology as a function of cooling rate, degree of undercooling, and time for haplogranite and haplogranodiorite systems modeled after Swanson and Fenn (1986) and MacLellan and Trembath (1991). Qz = quartz; Pl = plagioclase; Kfs = potassium feldspar.

Figure 18. Interpretive sketch of common morphological transformations linked to thermodynamic conditions and growth phenomena. On the left, enthalpy change (ΔH) corresponding to crystallization of the most abundant mineral phases in YTT rhyolite is modeled using rhyolite-MELTS [~75 wt% SiO_2 (sample T-20) at 2 kbar, 4 wt. % H_2O, and 1°C temperature increments] (Gualda et al. 2012b). The schematic cooling rate curve below is dimensionless, and serves to link thermodynamic changes to stages of crystallization under a high degree of undercooling. **(a)** The model of ΔH helps demonstrate that a large ΔT would impose massive crystallization near the eutectic. Thus, imposing a sudden large increase in ΔT or cooling rate of the melt can explain the *Stage 1* morphology sequence by nucleation and a subsequent pulse of rapid crystallization. Inflection of the cooling rate curve corresponds to an increase in latent heat released by crystallization, which causes ΔT, the cooling rate, and crystal growth rate to decrease (*Stage 2*). Skeletal to dendritic quartz infills during the period of maximum latent heat buffering and liquid differentiation, as conditions approach equilibrium (*Stage 2*; see text for details). Melt inclusions are entrapped as the crystal becomes polyhedral. *Stage 3* marks a second-stage of polyhedral overgrowth (generic oscillatory zoning), recording conditions typical of the system. **(b)** Fine dendritic overgrowths in crystal mantles record a pulse of strong undercooling (i.e. advancing crystal surface rapidly breaks into a cellular morphology), perhaps the same disequilibrium event(s) that formed skeletal to dendritic crystals of (a) (see text for details). Overgrowths are coated with dark CL infill and subsequently buried by ‘normal’ or

'generic' polyhedral growth. **(c)** Crystal exteriors showing a larger-scale transition from polyhedral to skeletal morphology may occur under a more moderate degree of undercooling or cooling rate compared to (a, b), and perhaps during a separate (late) disequilibrium event. Sketched features are not drawn to scale; single crystals or crystal units may preserve early, intermittent, and late morphology transformations (not illustrated).

Table 1 (next page)

Table 1. Interpretations of quartz textures in Toba rhyolites—a summary

Quartz feature	Interpretation
Asymmetric rhombohedra ± prism form	Initial rapid crystallization led to differential growth rates between individual dipyramidal or rhombohedral faces, as well as elongation parallel to the *c*-axis [a, b]. Alternatively or additionally, quartz may have crystallized initially in the α-quartz stability field [c, d]
Replete crystal faces	Quartz developed a polyhedral morphology during slower, interface-controlled growth under small degrees of undercooling [e, f, g]
Hollow crystal faces with terraced cavities or curvilinear lobes	Quartz formed a skeletal (hopper) morphology (preferential growth of crystal corners and edges) during rapid, diffusion-controlled growth under moderate to large degrees of undercooling [e, f, g]
Crystal with both replete and hollow faces	Quartz formed a morphology transitional between polyhedral and skeletal by (1) growing skeletally, then slowly infilling, or (2) growing slowly, then skeletally. Growth or infilling may have occurred preferentially on faces of forms $\{10\bar{1}1\}$ and $\{01\bar{1}1\}$ relative to $\{10\bar{1}0\}$ [a, f]
Embayments	(1) Quartz developed a cellular morphology during unstable, rapid crystal growth at higher degrees of undercooling and supersaturation [e, h, i, j]; or (2) infilling of early skeletal to dendritic quartz left recesses or cavities filled with matrix glass [h]; or (3) incidentally, a dissolving crystal surface intersected pre-existing melt inclusions or areas of high lattice defect density (e.g., protuberance or unit suture boundaries, twin planes), causing preferential dissolution, followed by regrowth [a, k]
Melt inclusions	Quartz trapped initially spherical or lens-shaped pockets of host melt either (1) along its growth surfaces [a, l, m], (2) during the infilling of hopper cavities [f], (3) at planar lattice defects between growing dendritic buds, twins, or merging skeletal protuberances [a, f], or (4) occasionally, by reprecipitation following preferential dissolution of areas with high-energy defects
Quartz clusters (Crystals with multiple growth centers, or *units*)	Quartz formed nucleation errors or lattice mistakes during rapid crystal growth, resulting in twinning and multiplex twins. Propagated growth of hopper crystals led to dendritic crystallization, which manifested as replicated overgrowths, or buds, on the initial crystals [a, f, k, n, o]
Subgrain boundaries	Quartz formed either (1) twin planes, or (2) dislocation planes between parallel units [f]
Blocky-undulatory extinction	Budding quartz formed dislocation planes at the contacts of growing, slightly misaligned units [a, f]
Arborescent CL zones	Quartz grew with a skeletal (hopper) to dendritic morphology, while incorporating a melt boundary layer and intrinsic lattice defects during rapid, diffusion-controlled growth under high degrees of undercooling and supersaturation [f, p, q, r, s]
Lens-shape, or linear oscillatory CL zones	Quartz preserves competitions between growth and diffusion at the crystal-melt interface [p, t, u]
Curved CL zone boundary	Quartz preserves an older dissolution surface that formed during a temperature increase [v, w] or adiabatic ascent of the magma [x]
Step CL zones	Quartz records significant changes in magmatic conditions (i.e. T, P, melt composition) that are preserved as major and non-periodic changes in CL intensity bounded by dissolution surfaces [t, v, x]
Accessory mineral inclusions	(1) Impurities rejected by rapidly crystallizing quartz led to a local supersaturation of titanomagnetite and apatite [a, f, n, y]
Dauphiné twins	Quartz formed (secondary) penetration twins to accommodate strain induced by (1) rapid cooling through the β-α transition and (2) syn-eruptive crystal fracturing related to melt inclusion decrepitation [b, c]

[a] Sunagawa 2005; [b] Frondel 1962; [c] Frondel 1945; [d] Flick 1987; [e] Laemmlein 1930; [f] Welsch et al. 2013; [g] Swanson and Fenn 1986; [h] MacLellan and Trembath 1991; [i] Donaldson 1976; [j] Lofgren 1980; [k] Brugger and Hammer 2015; [l] Roedder 1979; [m] Chesner and Luhr 2010; [n] Hammer et al. 2010; [o] Buerger 1945; [p] Milman-Barris et al. 2008; [q] Welsch et al. 2014; [r] Huang and Audétat 2012; [s] Götze et al. 2001; [t] Allègre et al. 1981; [u] Seitz et al. 2015; [v] Wark et al. 2007; [w] Kuo and Kirkpatrick 1985; [x] Thomas et al. 2010; [y] Bacon 1989.

Figure 1. (5.5" width)

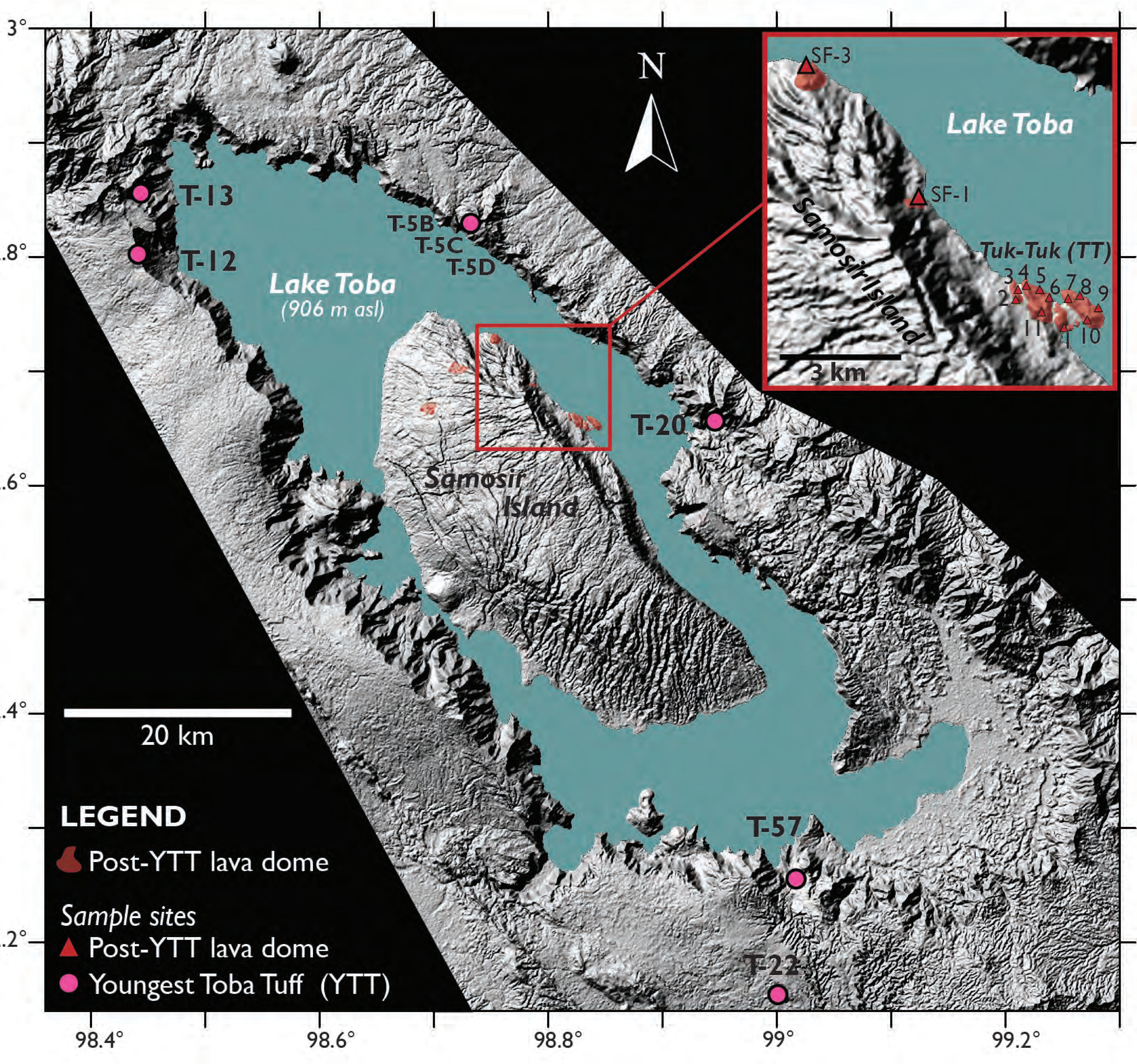

Figure 2. (3" width)

Figure 3. (6.5" width)

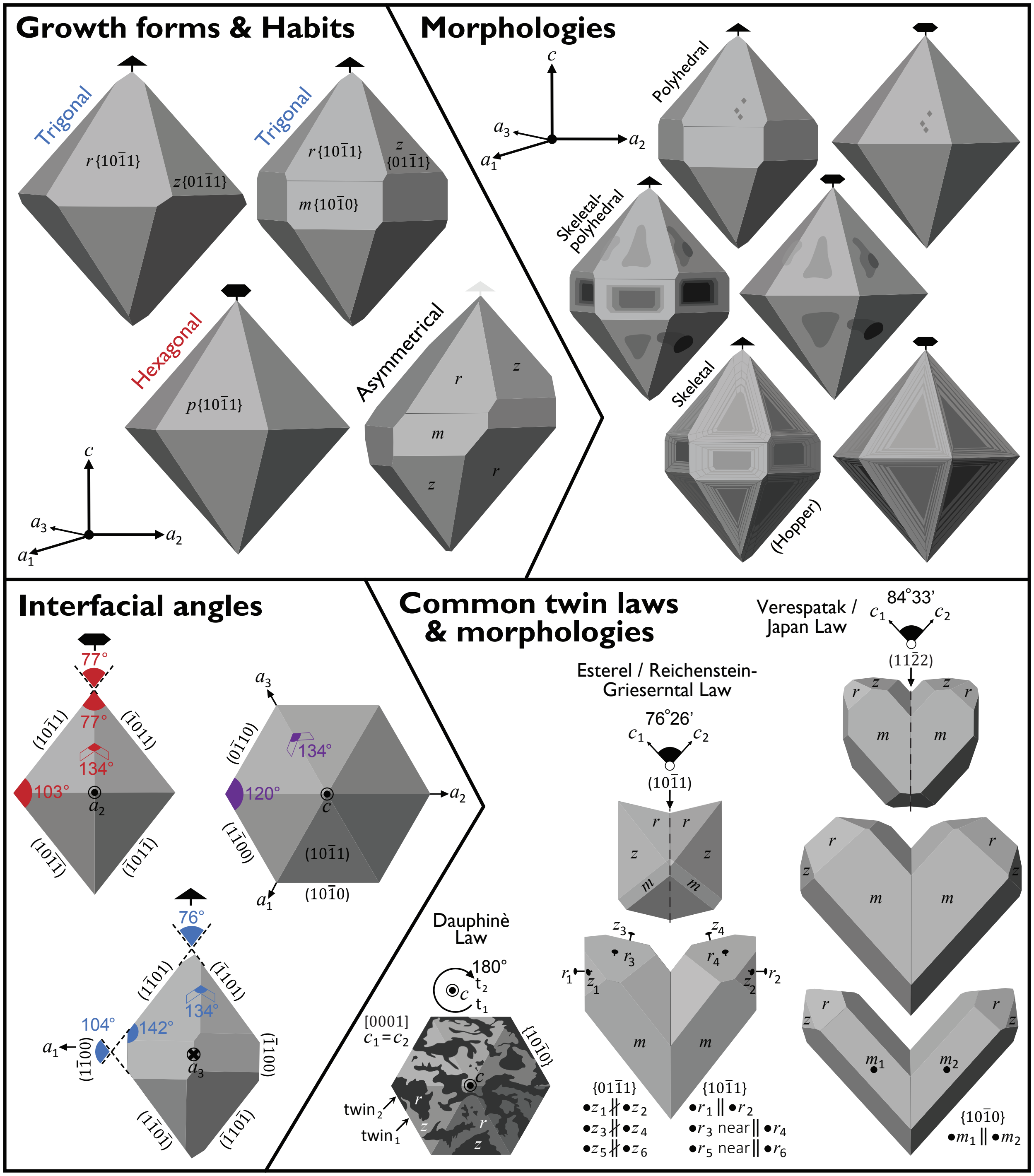

Figure 4. (6.5" width)

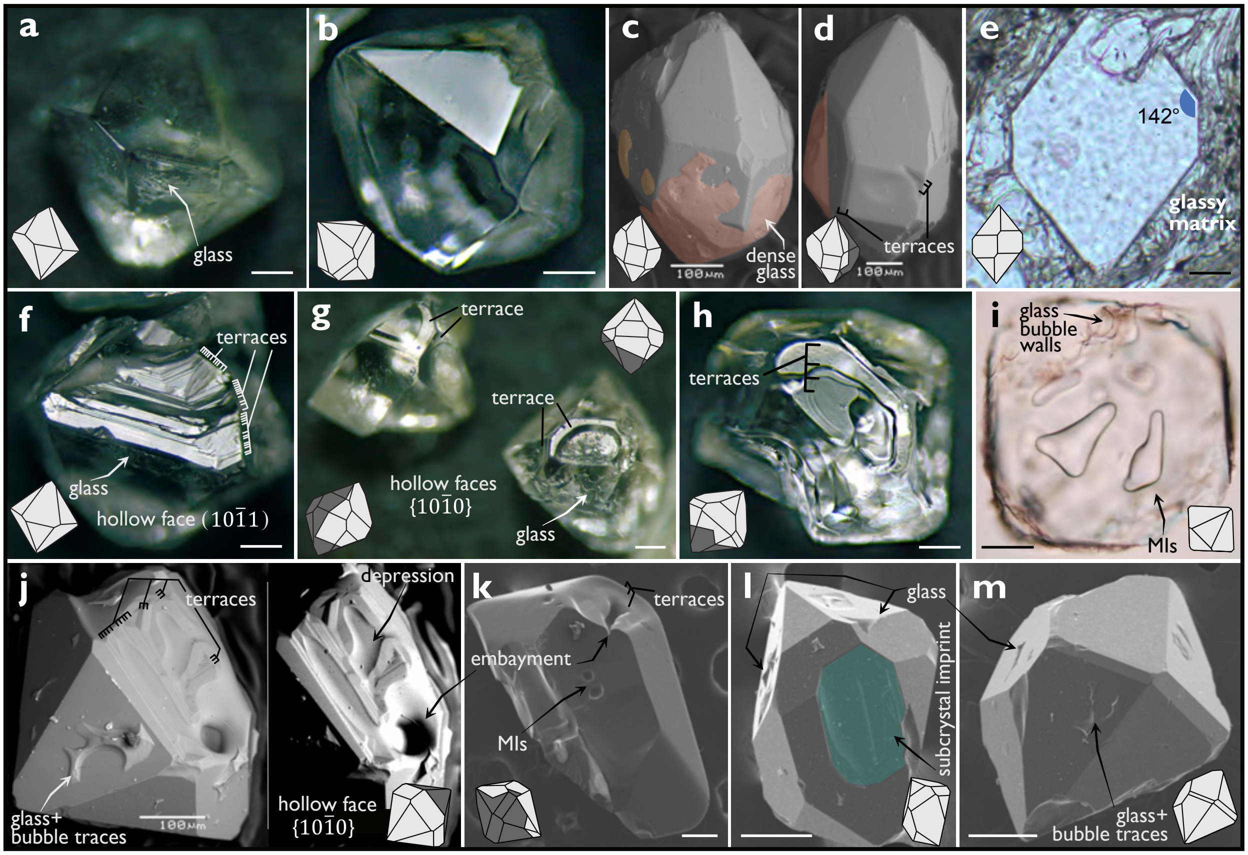

Figure 5. (6.5" width)

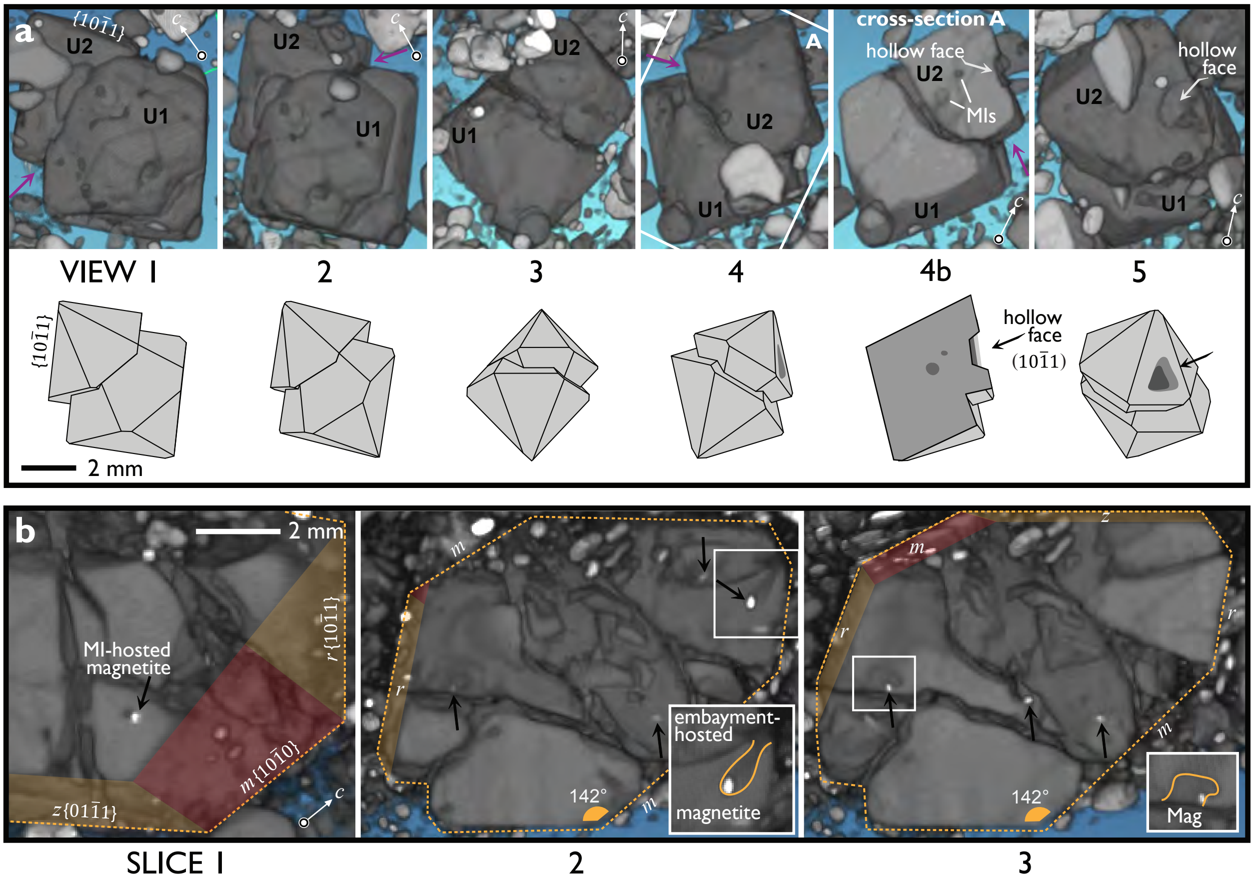

Figure 6. (6.5" width)

Figure 7. (6.5" width)

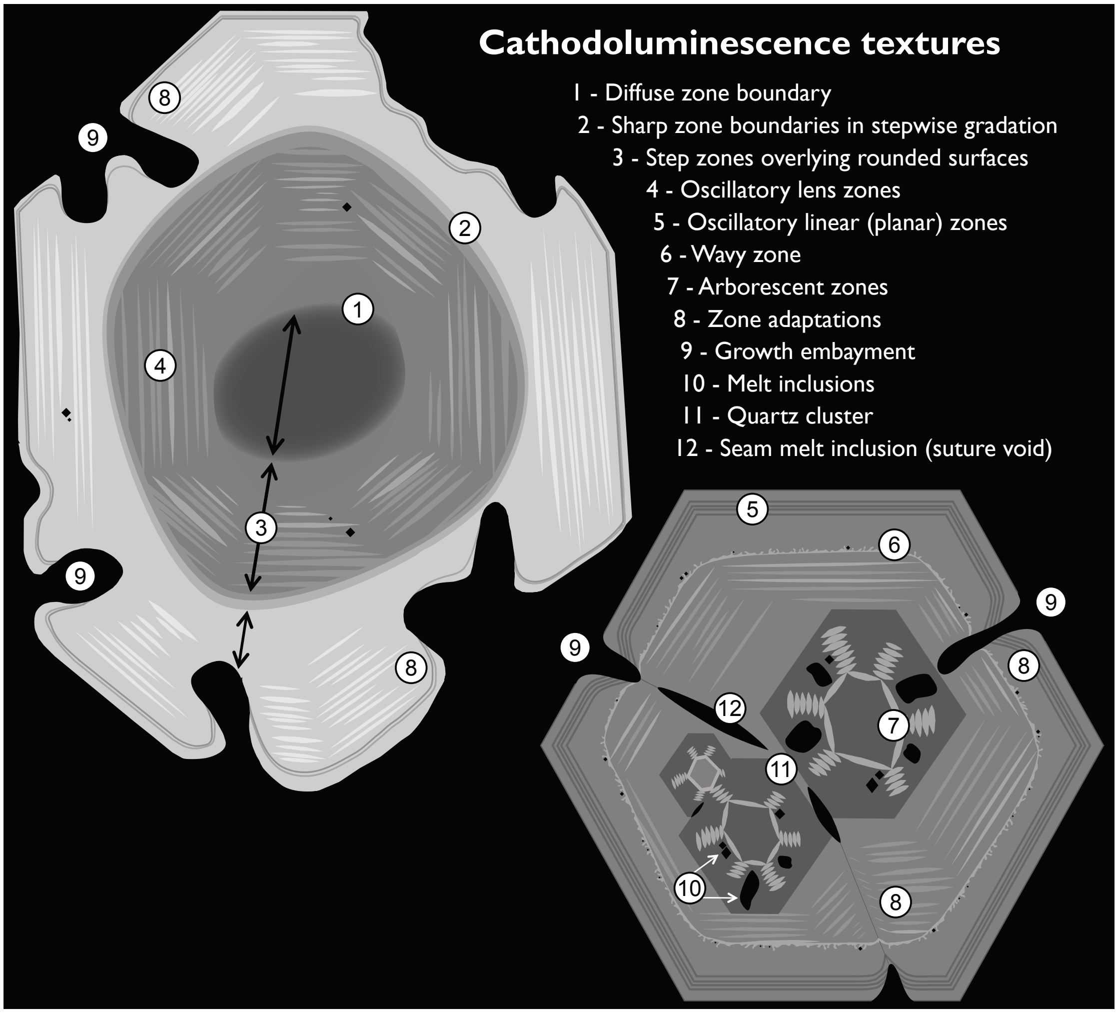

Figure 8. (part 1) (6.5" width)

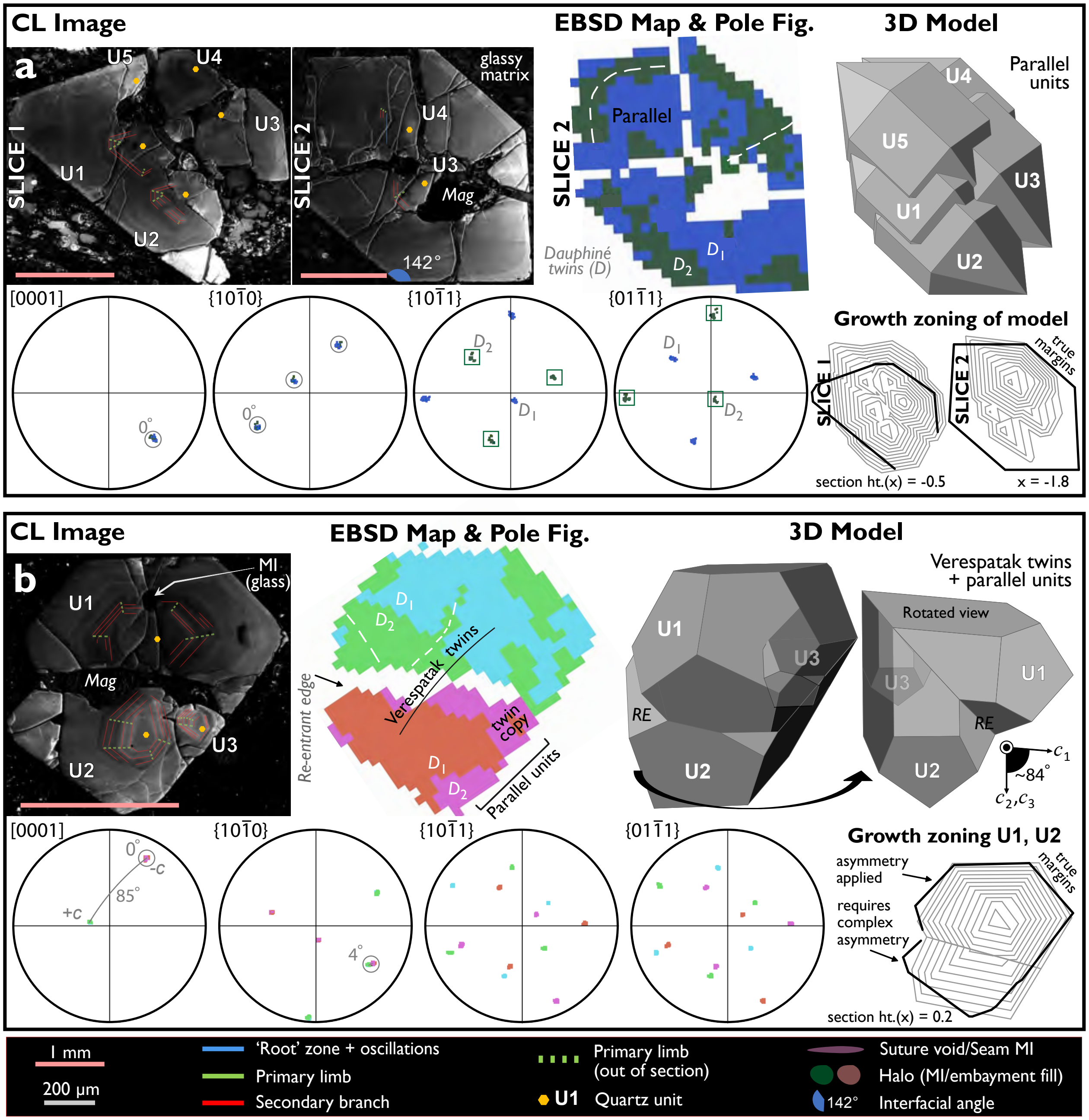

Figure 8 continued. (part 2) (6.5" width; landscape)

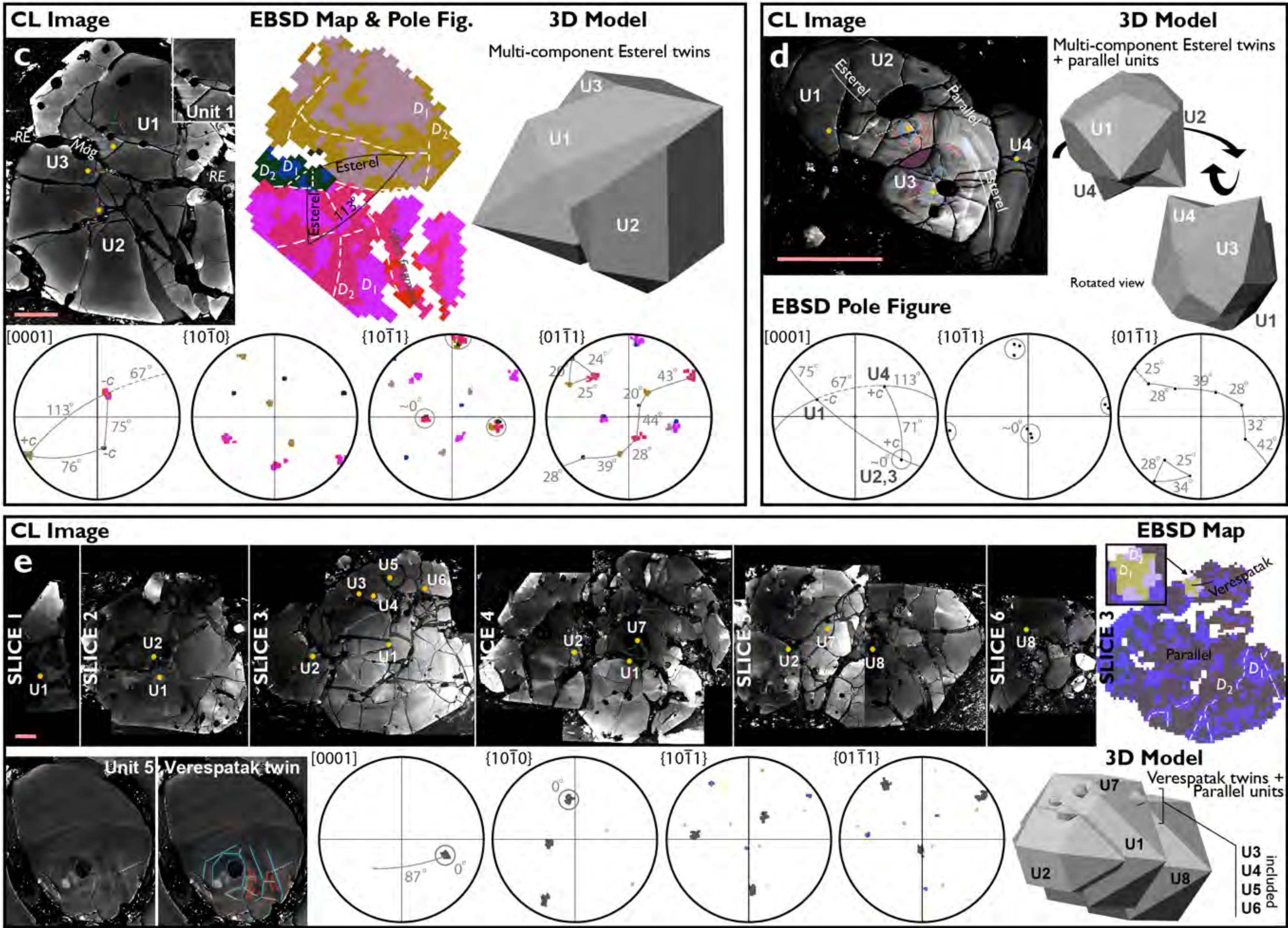

Figure 9. (6.5'' width)

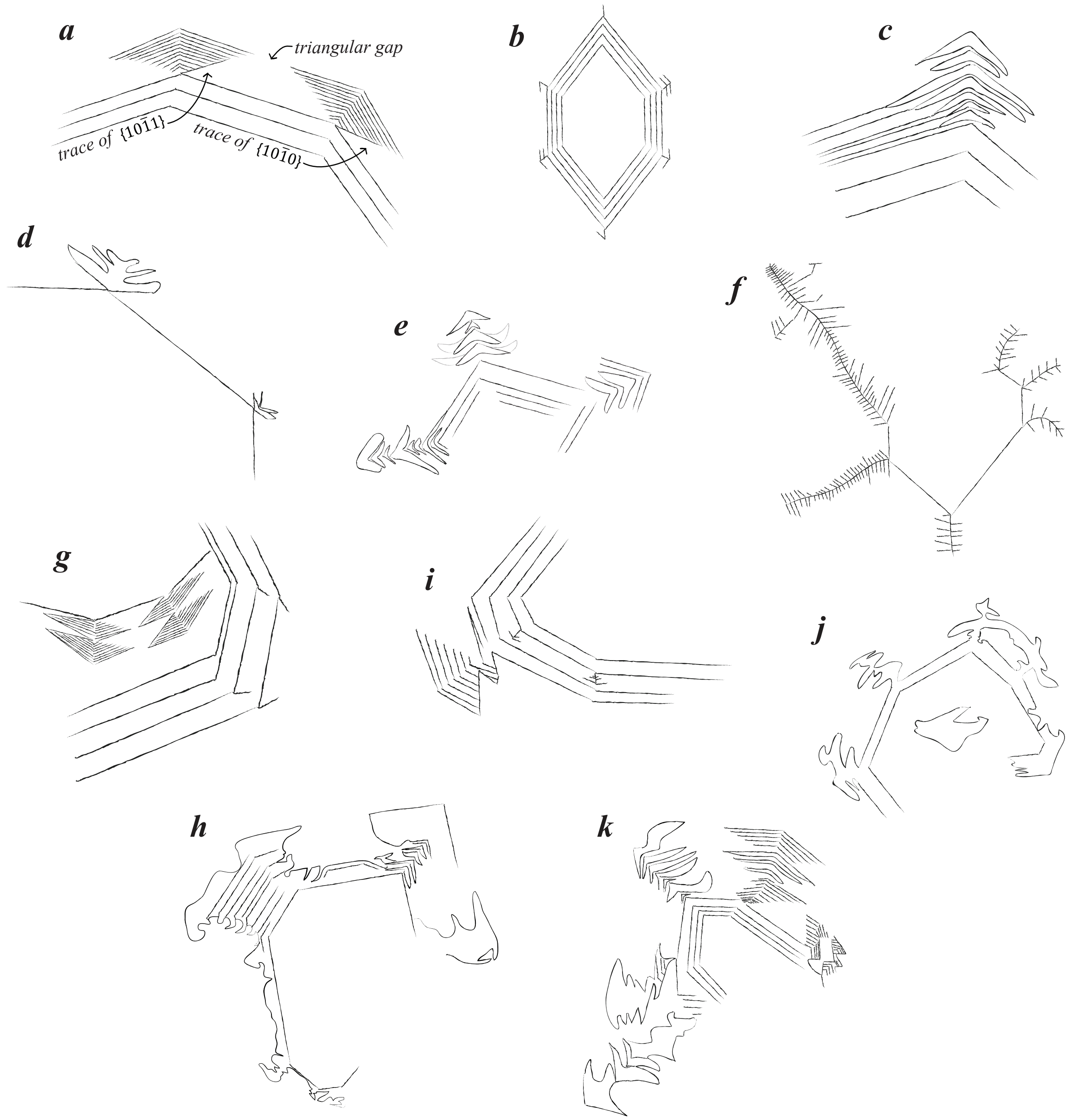

Figure 10. (part 1)   (6.5" width)

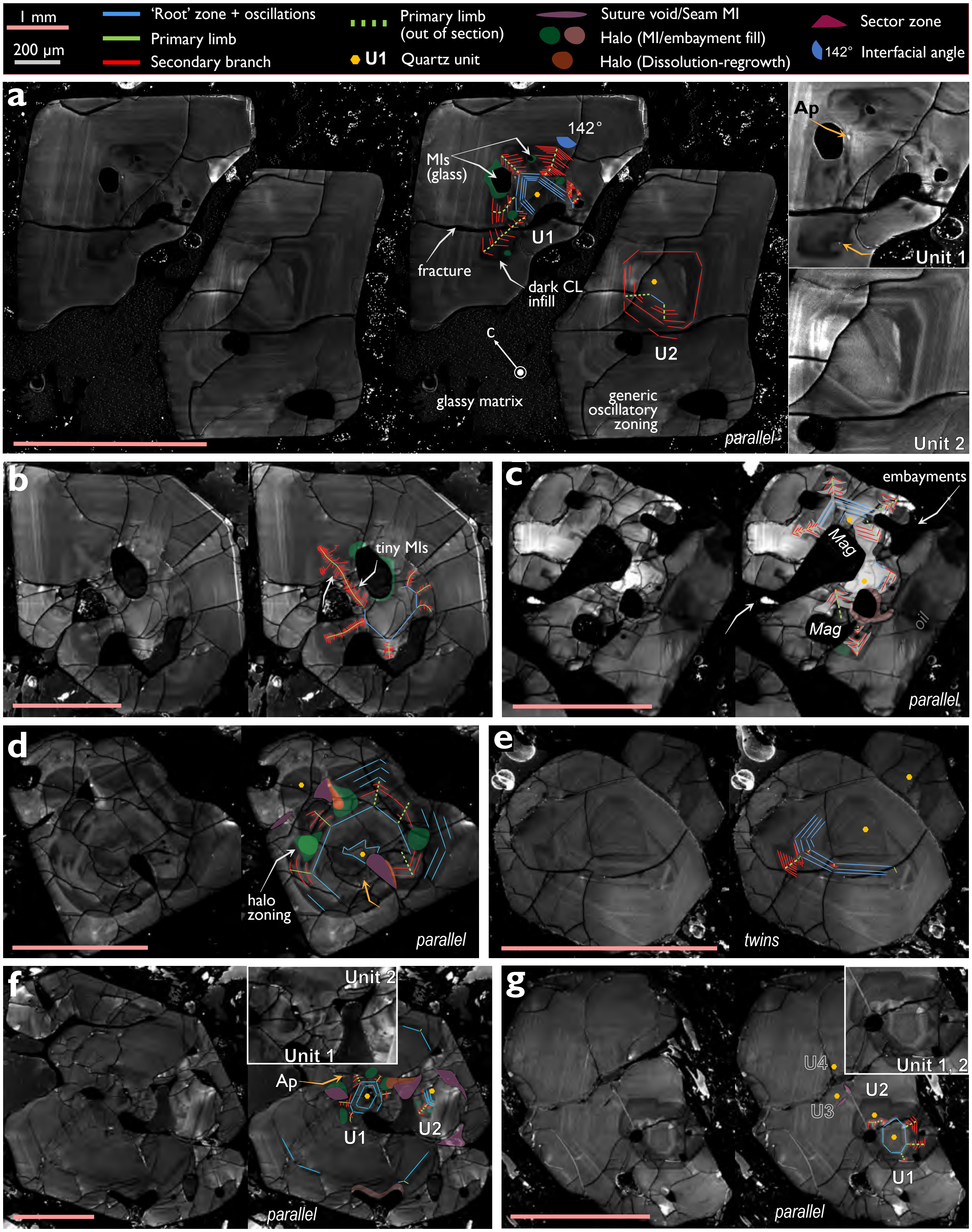

Figure 10 continued. (part 2) (6.5” width)

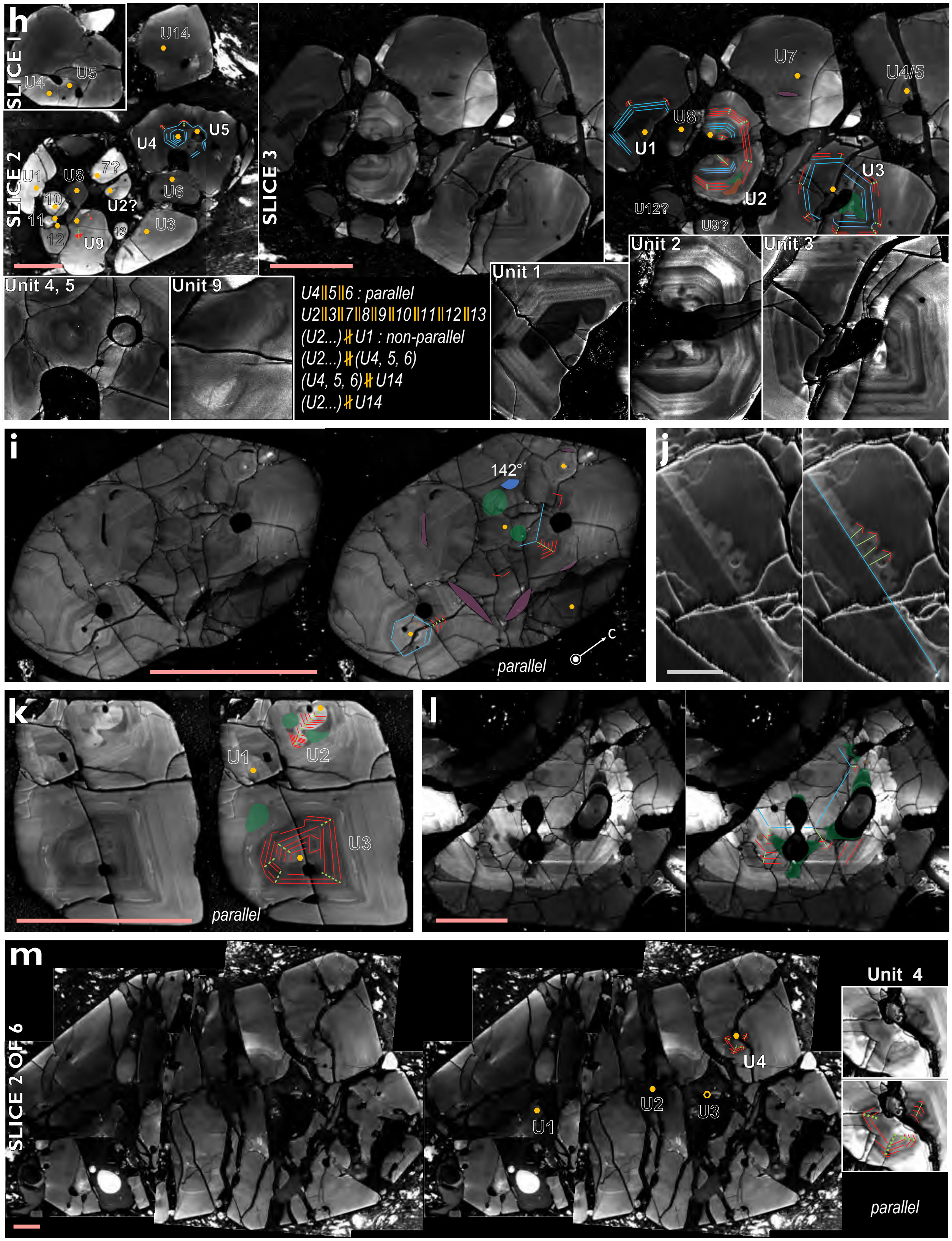

Figure 11.   (6.5" width)

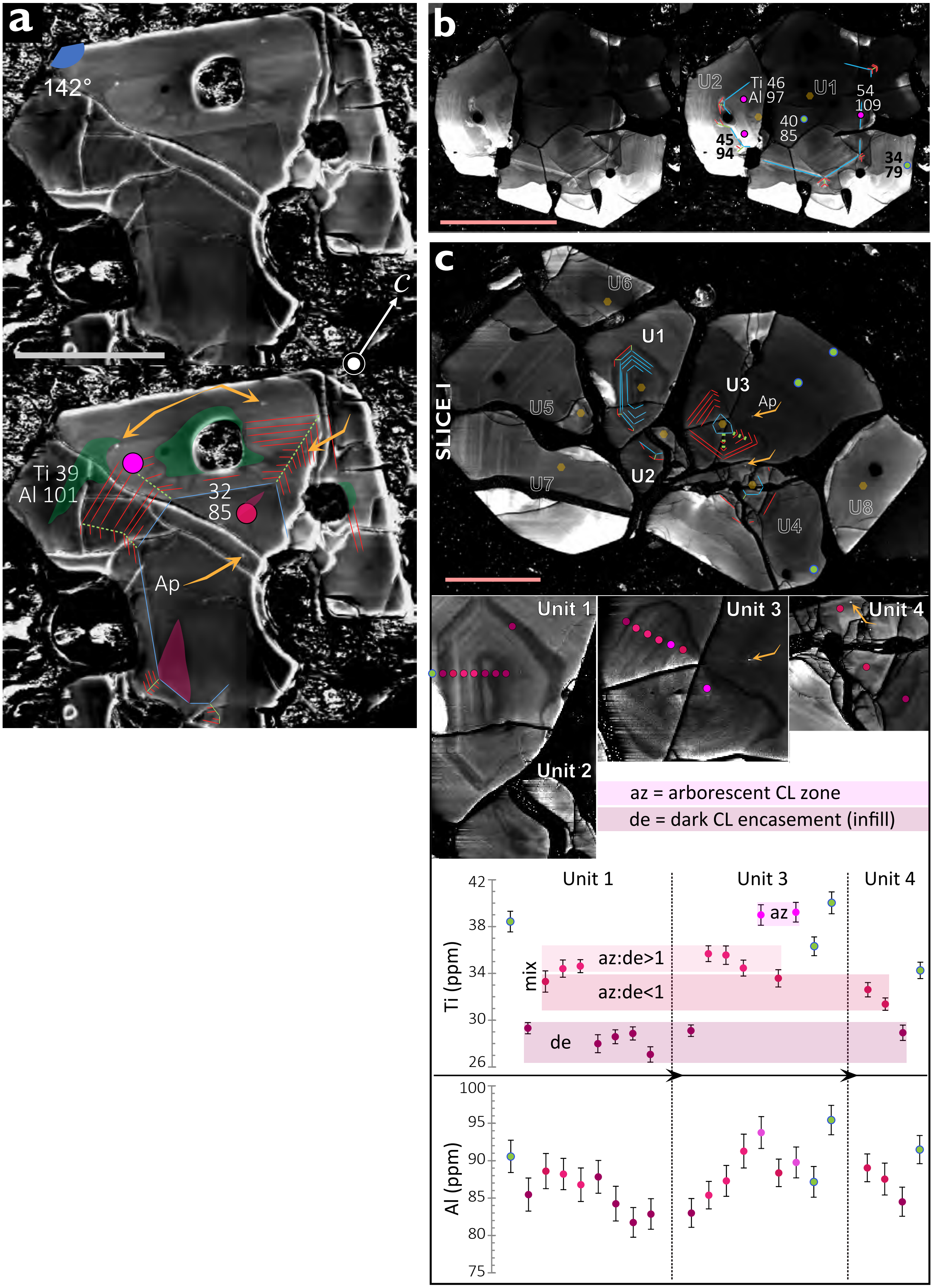

Figure 12. (6.5" width)

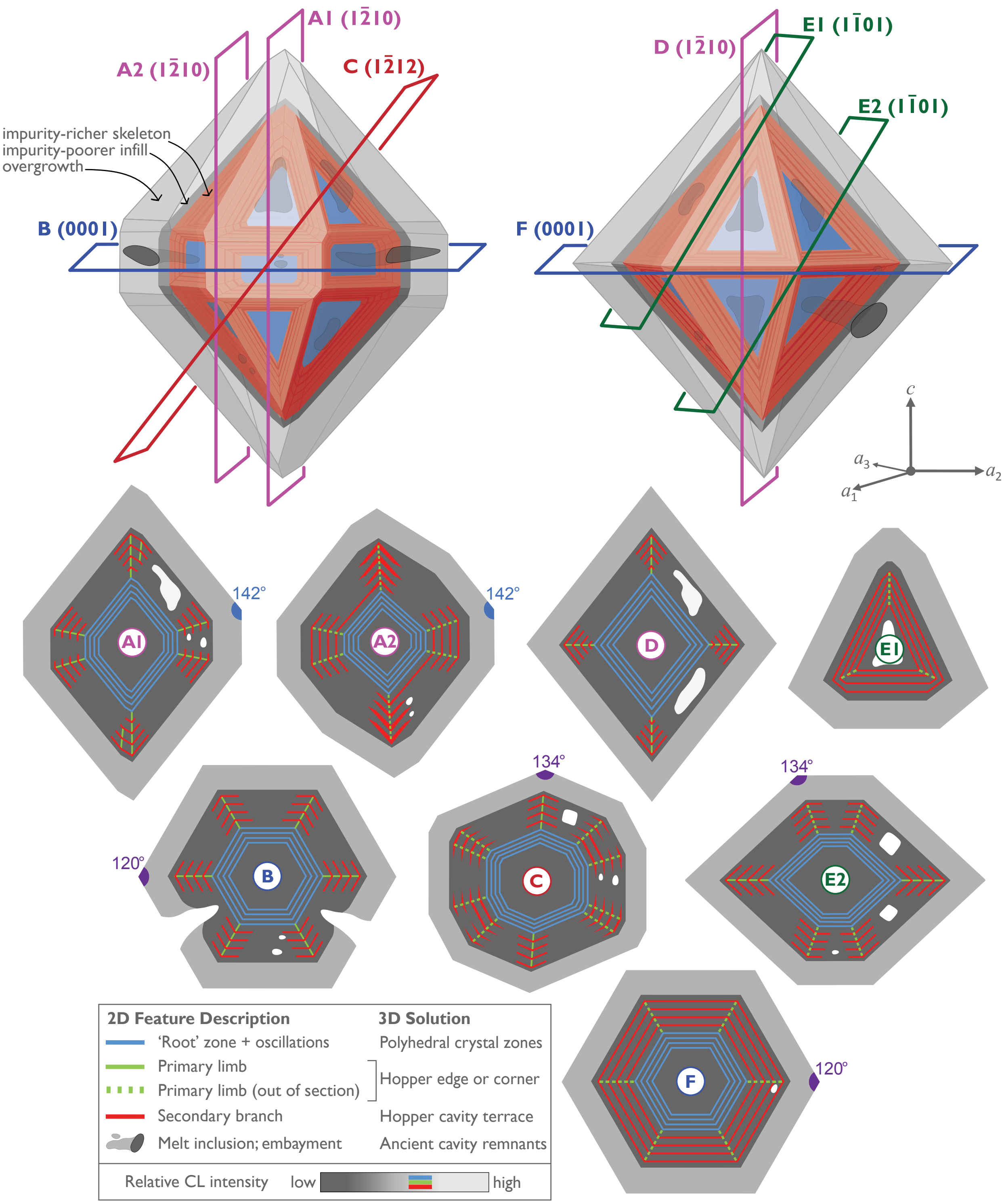

Figure 13. (~3" width)

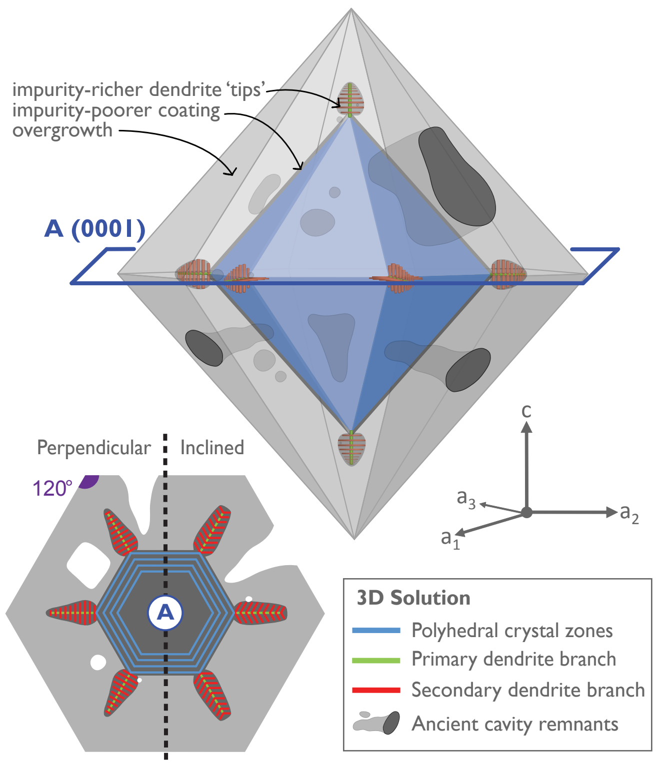

Figure 14. (~3" width)

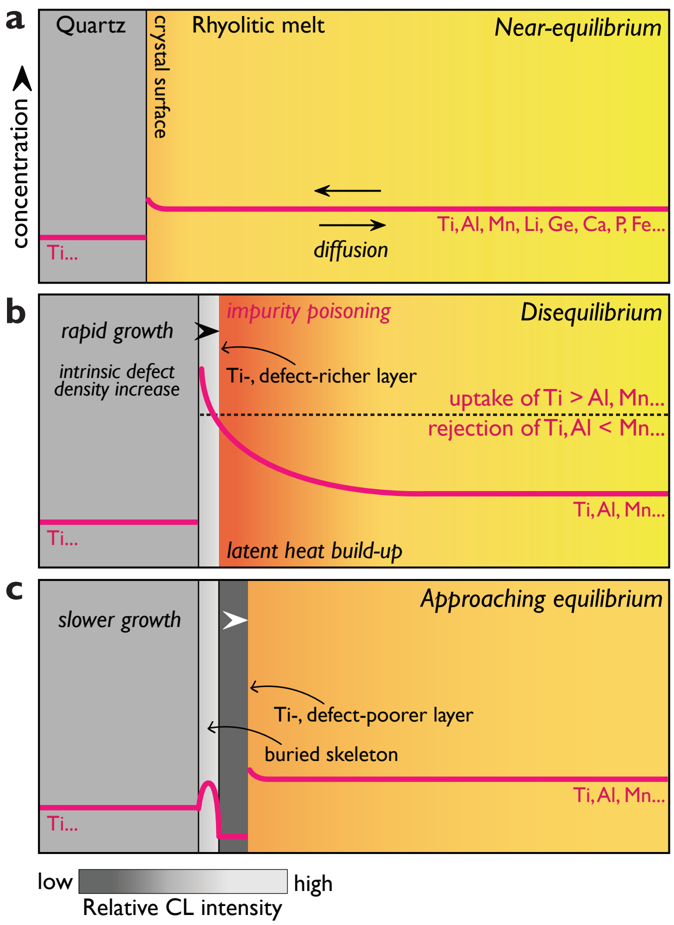

Figure 15. (6.5” width)

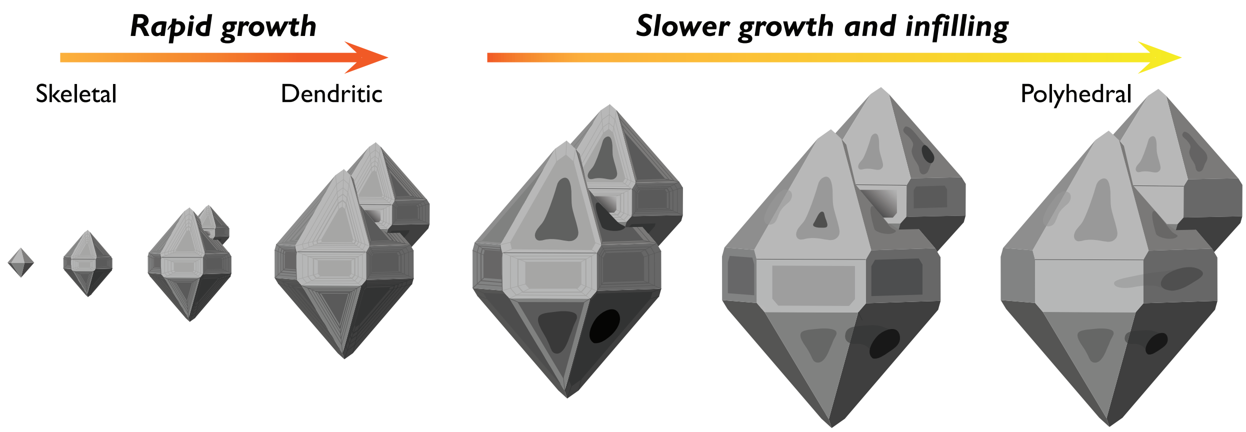

Figure 16. (6.5" width)

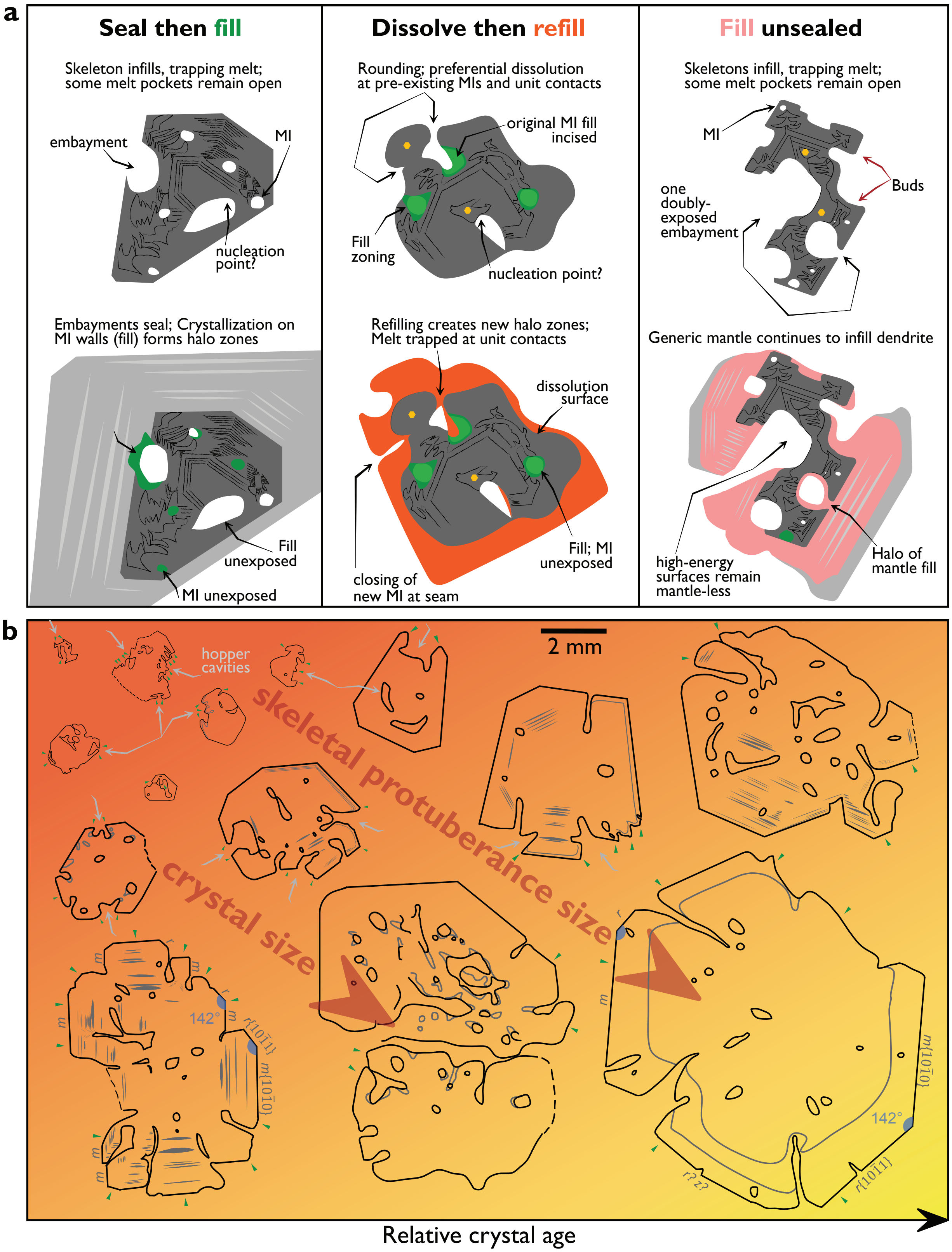

Figure 17. (5" width)

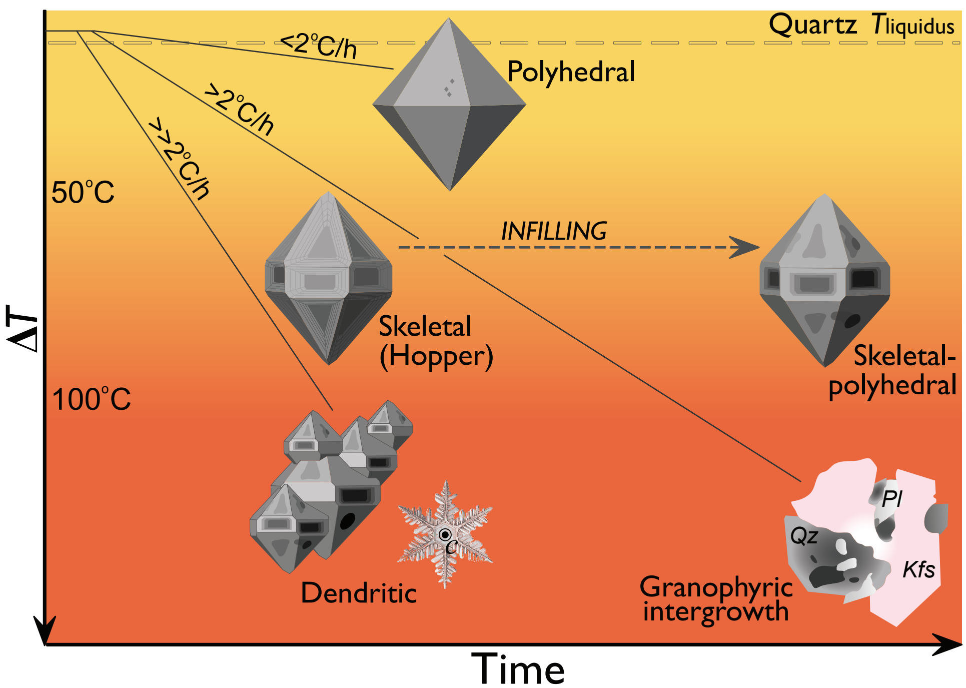

Figure 18. (6.5" width)